DISCLAIMER

This report was prepared as an account of work sponsored by an agency of the United States Government. Neither the United States Government nor any agency thereof, nor any of their employees, makes any warranty, express or implied, or assumes any legal liability or responsibility for the accuracy, completeness, or usefulness of any information, apparatus, product, or process disclosed, or represents that its use would not infringe privately owned rights. Reference herein to any specific commercial product, process, or service by trade name, trademark, manufacturer, or otherwise does not necessarily constitute or imply its endorsement, recommendation, or favoring by the United States Government or any agency thereof. The views and opinions of authors expressed herein do not necessarily state or reflect those of the United States Government or any agency thereof. Reference herein to any social initiative (including but not limited to Diversity, Equity, and Inclusion (DEI); Community Benefits Plans (CBP); Justice 40; etc.) is made by the Author independent of any current requirement by the United States Government and does not constitute or imply endorsement, recommendation, or support by the United States Government or any agency thereof.

SANDIA REPORT
SAND20XX-XXXX
Printed Click to enter a date

Evolution of the electrothermal instability from thick rod z pinches subject to dynamically and statically applied axial magnetic field

Thomas J. Awe[1], Edmund P. Yu[1], Gabriel S. Shipley[2], Derek C. Lamppa[1], Kurt Tomlinson[3], Edward G. Holman[1], Kevin C. Yates[1], Maren W. Hatch[1], Fernando Sanchez[1], Deanna Jaramillo[1], Matt Ales[4], Trospy Jarret[5], Ronald J. Kaye[1]

[1]Sandia National Laboratories, Albuquerque NM
[2]Los Alamos National Laboratory, Los Alamos, NM
[3]General Atomics, La Jolla, CA
[4]Oak Hill Engineering, Sumner WA
[5]Milhous Company, Amherst VA

Prepared by
Sandia National Laboratories
Albuquerque, New Mexico
87185 and Livermore,
California 94550

Issued by Sandia National Laboratories, operated for the United States Department of Energy by National Technology & Engineering Solutions of Sandia, LLC.

Available to DOE and DOE contractors from
U.S. Department of Energy
Office of Scientific and Technical Information
P.O. Box 62
Oak Ridge, TN 37831

Telephone: (865) 576-8401
Facsimile: (865) 576-5728
E-Mail: reports@osti.gov
Online ordering: http://www.osti.gov/scitech

Available to the public from
U.S. Department of Commerce
National Technical Information Service
5301 Shawnee Rd
Alexandria, VA 22312

Telephone: (800) 553-6847
Facsimile: (703) 605-6900
E-Mail: orders@ntis.gov
Online order: https://classic.ntis.gov/help/order-methods/

ABSTRACT

LDRD Project 229427 aimed to determine how electrothermal instability (ETI) driven heating on a z-pinch rod pulsed with intense current evolves under mixed magnetic field (azimuthal + axial) conditions, which is pertinent to pulsed-power-driven magnetically-insulated transmission lines and physics targets. Experiments focused on diagnosing ETI-driven heating from deliberately-machined and well-characterized micron-scale surface defects (referred to as engineered defects or ED). Prior to the start of this project, understanding of how unmagnetized (B_z=0) ED evolve had been obtained—simulations largely reproduce the experimentally observed high temperature spots which develop at the poles of bare/uncoated ED. Project 229427 extended the Mykonos Facility ED experimental platform to include axial field. In the first class of experiments, axial field was provided “dynamically” via a helical return can (HRC). In this case, B_z and B_θ rise at the same rate. Generally, the HRC generated magnetic field at a fixed polarization angle $\phi_B=\arctan(B_z/B_\theta)=15°$ on the rod’s surface. In the second class of experiments, axial field was provided “statically” via a slow-rising (millisecond) external Helmholtz coil pair. In this case, B_z was effectively constant/static throughout the 100 ns rise of the Mykonos current. For either case, a primary goal was to determine whether ETI provides a helical seed perturbation for the subsequent growth of the helical magneto Rayleigh-Taylor modes observed in MagLIF (static B_z) and dynamic screw pinch (DSP, dynamic B_z) experiments. When dynamic field was applied using an HRC, emissions from individual ED aligned toward ϕ_B, while emissions from ED within pairs elongated and preferentially merged along ϕ_B. These data strongly support that for a randomized defect distribution, heating from nearby current-density perturbations will favorably merge about ϕ_B to generate an extended seed perturbation that aligns toward the surface-field polarization, and this may impact the orientation of subsequent MRT growth on imploding liners. The results from the static field experiments were largely inconclusive, as any ETI heating rotation, if present, was obscured/overwhelmed by local/random heating from ED rim imperfections.

ACKNOWLEDGEMENTS

The authors would like to acknowledge useful conversations with and/or support from D. Ampleford, P. Ballance, B. Bauer, S. Bova, E. Breden, K. Cochrane, A. Crabtree, M. Cuneo, K. DeZetter, M. Gilmore, I. Golovkin, E. Harding, N. Hines, T. Hutchinson, B. Hutsel, D. Jaramillo, C. Jennings, M. Jones, C. Kalogeras, I. Kern, W. Lewis, L. Lucero, K. Matzen, J. Niederhaus, R. Obregon, R. Paguio, L. Perea, K. Perkins, K. Peterson, M. Rich, A. Robinson, G. Rochau, K. Rodgers, A. Sarracino, J. Schwarz, D. Sinars, S. Slutz, R. Speas, S. Speas, A. Steiner, W. Tatum, R. Vesey, M. Weis, and D. Yager-Elorriaga. The Applied B on Mykonos sub-team acknowledges Andrew Contreras, Jens Schwarz, and all the reviewers of the work plan for activities on Mykonos. This research was supported by Sandia's Laboratory Directed Research and Development Program (LDRD, Project Nos. 200269 and 229427). This work was also funded in part by Sandia's LDRD program via the appointment of one of the authors (G. Shipley) to the Truman Fellowship in National Security Science and Engineering, Project No. 226067. Sandia National Laboratories is a multi-mission laboratory managed and operated by National Technology and Engineering Solutions of Sandia, LLC., a wholly owned subsidiary of Honeywell International, Inc., for the U.S. Department of Energy's National Nuclear Security Administration under Contract No. DE-NA-0003525. This paper describes objective technical results and analysis. Any subjective views or opinions that might be expressed in the paper do not necessarily represent the views of the U.S. Department of Energy or the United States Government

CONTENTS

This page left blank

ACRONYMS AND TERMS

Acronym/Term	Definition
ABM	applied B on Mykonos
AJB	ABM junction box
ED	engineered defect
EMO	emergency off
ETI	electrothermal instability
HRC	helical return can
HV	high voltage
ICCD	intensified charge coupled device
ICF	inertial confinement fusion
LCA	laser control area
LDM	long distance microscope
LDRD	laboratory directed research and development
LJB	load junction box
LOS	line of sight
MDI	magnetically driven implosion
MHD	magnetohydrodynamic
MITL	magnetically insulated transmission line
MRT	magneto Rayleigh-Taylor
NI	National Instruments
PDV	photonic Doppler velocimetry
SRC	straight return can
STS	slow tool servo
TTL	transistor-transistor logic

1. INTRODUCTION

1.1. Note on the duplication of text from a recent publication

Note: This section largely follows a portion of the introduction provided in a recent publication in Physics of Plasmas, entitled "Rotation of electrothermal-instability-driven overheating structure due to helically oriented surface magnetic field on a high-current-density aluminum rod," which can be accessed via the following link: https://doi.org/10.1063/5.0279628

That publication [i] focuses primarily on ETI physics in the presence of dynamically applied axial field (B_z and B_θ rise together), which is provided by a helical return can. In this SAND report, however, we also discuss ETI physics in the presence of statically applied axial field (B_z is constant versus rapidly rising B_θ), which is provided by Helmholtz coils. So, the introduction has been modified accordingly to introduce both dynamic and static axial field studies. That said, many paragraphs, figures, and figure captions are copied verbatim from the publication.

1.2. Introduction to helical instabilities on axially magnetized z pinches

1.2.1. Axial field in MagLIF fusion systems

Fast z pinches, in general, consist of an annular, axially-flowing, fast current pulse (e.g., ~100 ns risetime) which generates an azimuthal magnetic field, resulting in radial compression of the current-carrying material via the Lorentz Force. Z pinch configurations include single wires/rods, arrays of wires, gas puffs, and imploding liners (cylindrical thick-walled tubes or cylindrical thin-walled foils) and are broadly applicable to controlled thermonuclear fusion [ii,iii,iv,v,vi,vii], the production of intense x-rays [viii,ix], and the study of laboratory astrophysics [x]. Z pinches are physics-rich platforms, with open questions concerning their current carrying properties, material phase changes, implosion dynamics, stability, and stagnation properties.

The studies in this LDRD apply most directly to the detailed current carrying properties of thick-walled imploding metallic liners, where the liner's wall thickness is much larger than the metal's room temperature magnetic field skin depth. Such liners can be used to both compress and inertially confine preheated and premagnetized fusion fuel in Magneto-Inertial Fusion (MIF) systems [xi,xii,xiii]. In Magnetized Liner Inertial Fusion (MagLIF [xiv,xv,xvi,xvii,xviii]), the preeminent MIF concept, an external Helmholtz coil pair premagnetizes the liner and the fusion fuel within to an axial field strength B_z=10-30 T [xix]. The coils are driven with a several-millisecond risetime so that B_z is "static" in the sense that it is fully diffused and uniform within the liner-fuel system before a ~20 MA, 100 ns current is pulsed on the liner's outer surface to drive the implosion. Fuel premagnetization is fundamental to the MagLIF concept, and experiments demonstrate enhanced stagnation performance (e.g., plasma temperature, neutron yield [xx,xxi]), and magnetization of tritons [xxii,xxiii] as a direct result of this applied and subsequently liner-compressed B_z.

Early MagLIF-relevant experiments demonstrate that inclusion of static B_z has transformative impact on the implosion dynamics of the metallic liner [xxiv,xxv]. For liners imploded without axial premagnetization, largely azimuthally symmetric magneto-Rayleigh Taylor (MRT) instabilities develop [xxvi,xxvii]. This is expected due to magnetic tension, since the fastest growing MRT modes align with a wave vector (**k**) that is perpendicular to the azimuthal drive field such that $k_z \bullet B_\theta=0$ (note, however, that perfect alignment is not required for a mode to grow). By contrast, helically-oriented instability structures develop for liners premagnetized with static B_z~10 T. Initially, perhaps, this result seems intuitive, since, early in the experiment when the axial current is low, the magnetic field polarization angle at the liner's outer surface $\phi_B(t) \equiv \arctan[B_z(t)/B_\theta(t)]$ is large ($B_z \sim B_\theta$, thus $\mathbf{k} \bullet \mathbf{B} \sim 0$ for helically oriented perturbations). But significant ϕ_B is presumably short-lived because B_θ is expected to grow to >1000 T, whereas B_z is expected to remain nearly constant, at ~10 T. Therefore, since $\phi_B(t) \sim 0$ for all but the earliest (pre-implosion) stages of the experiment azimuthally symmetric MRT was expected. Data, however, show dominant and persistent helical instability modes. Furthermore, the pitch angle of the observed helices grow steeper as the liner implodes, suggesting that the helical modes are somehow "locked" to the liner's surface.

Axial magnetic field may have further utility to MagLIF by improving liner implosion stability through a dynamic screw pinch (DSP) mechanism. A DSP includes a helically-wound return-current path, or helical return can (HRC) which is coaxial with the liner and drives a time-varying axial magnetic field, $B_z(t)$, at the liner's surface. Here the axial field is "dynamic" in the sense that it is driven with the same rise time as the driver current, and, prior to liner implosion, the surface polarization angle ϕ_B will remain constant for a given HRC design. However, as the liner implodes, at the liner's surface $B_\theta(t)=\mu_0 I(t)/2\pi r(t)$ increases more rapidly than $B_z(t)$, since $B_\theta(t)$ increases as the liner radius, $r(t)$, falls, thus driving ϕ_B downward (toward the horizontal). Time varying ϕ_B results in a continuous change in which MRT mode is most unstable as the liner implodes, resulting in a reduction in the accumulated growth time for any one mode. For MagLIF-like liners, theory suggests that linear MRT growth should be reduced by one to two orders of magnitude via the DSP method [xxviii]. Magnetohydrodynamic (MHD) simulations suggest [xxix, xxx] that DSP-driven liners should evolve with a persistent helical instability, with a pitch angle that both grows for higher initial ϕ_B and increases as the liner implodes. Data from Z experiments suggest that the DSP improves liner-implosion stability, though detailed analysis has yet to be published.

1.2.2. Hypotheses concerning helical instability formation and evolution

Fundamental questions regarding instability development on axially magnetized imploding liners remain, including: (1) when is a helical perturbation initiated? And (2), under what conditions does the helical perturbation grow/persist throughout the implosion? When considering these questions, we distinguish 4 general field-polarization-evolution scenarios for thick-walled metallic liners:

In **Scenario 1 (static B_z, no flux compression)**, static field is provided by external Helmholtz coils, B_z is fully diffused and uniform prior to the liner implosion, and no axial flux compression occurs at the liner's outer surface. The field is initially purely axial (prior to Z's current delivery), followed by a brief pre-implosion stage, where $B_z \sim B_\theta$, followed by $B_\theta \gg B_z$ for the remainder of the experiment. Here, helical modes are only reasonably seeded pre-implosion while $B_z \sim B_\theta$. Early helical seeds could grow due to electrothermal instability (ETI) driven liner-surface melt [xxxi, xxxii, xxxiii]. The time and orientation of melt may also be influenced by energy deposition from magnetically insulated transmission line (MITL) flow plasmas [xxxiv] where energetic particles bombarding the liner's surface may drive helically-oriented heating.

The remaining scenarios consider $B_z(t)$ which grows throughout the experiment. In **Scenario 2 (static B_z, compressed flux)** static axial field is generated from external coils as in Scenario 1, but now MITL-generated low-density plasmas with sufficient electrical conductivity to advect magnetic field enter the target region and implode via the Lorentz Force to compress B_z to near 1000 T [xxxv,xxxvi], supporting persistent $\phi_B(t)$ and enabling the possibility of helical mode seeding throughout the experiment. In **Scenario 3 (Hall instability)** static field is generated as in Scenario 1, but now an interchange instability within a low-density coronal plasma (e.g., 10^{15} cm^{-3}) generates helical plasma filaments on the liner's outer surface which carry helical current [xxxvii,xxxviii,xxxix]. This current aligns with the magnetic field and is thus force free. The force-free configuration persists to generate increasing $B_z(t)$ throughout the experiment, supporting persistent $\phi_B(t)$. In **Scenario 4 (DSP)**, there is no static applied field, but rather $B_z(t)$ increases linearly with current, conceivably to 100s of T, via the DSP mechanism [xxviii, xxix]. Qualitatively then, **Scenarios 2-4** all include helically polarized surface magnetic field at the liner's surface throughout (albeit by distinct mechanisms) making the persistence of helical modes expected relative to **Scenario 1**.

Helical instability development has been considered theoretically and computationally. For example, relevant to **Scenario 1 (static B_z, no flux compression)**, Weis *et al*., used ideal MHD and linear perturbation theory to evaluate the coupling of sausage and kink modes to MRT for the cases of thin and thick imploding liners with uniform B_z inside, within, and outside of the current carrying metal [xl]. Instabilities of the form $\exp(im\Theta - i2\pi z/\lambda)$ develop, where m is the azimuthal mode number, and λ is the perturbation wavelength. In the absence of B_z, m=0 sausage modes dominate, while higher-order modes (m>0) grow more rapidly when B_z is present. Larger B_z "unlock" higher mode numbers, enabling growth of multiple intertwined helices, in qualitative agreement with the structures observed in [xxiv]. Furthermore, when B_z is present, m=0 mode growth is delayed, and the growth rate is reduced versus higher mode numbers, potentially explaining the persistence of helical modes in **Scenario 1**, even if $B_\theta >> B_z$ for much of the experiment. Also, 3D MHD simulations [xxv] showed that if helical surface perturbations can be seeded pre-implosion the perturbation will grow, even in the absence of applied helical field.

Other studies have focused on helical instability evolution for $B_z(t) \sim B_\theta(t)$, i.e., for **Scenarios 2-4**. For example, relevant to **Scenario 2 (static B_z, compressed flux)** Seyler *et al*., have shown computationally using the extended MHD (XMHD) code PERSEUS [xxxvi] that such a flux-compression mechanism can result in strong $B_z(t)$ at the liner's surface to support helical instability growth. Later, to explore **Scenario 3 (Hall instability)**, PERSEUS was again used to model the impact of Hall physics on helical-mode generation, but now the low-density plasma is localized to a coronal plasma layer which surrounds the liner [xxxviii]. For simulations initialized with an ad-hoc low-density plasma layer, helical modes grow and persist both for foils driven at 1 MA current, or MagLIF-like liners driven by 20-60 MA current. Finally, relevant to **Scenario 4 (DSP)**, Shipley *et al*. have presented 3D MHD simulations which demonstrate that helical modes grow from liners seeded with a random/white-noise perturbation when driven by the DSP mechanism [xxx]. Axial flux compression is not required for helical-instability growth for the DSP mechanism, but the possibility of MITL-generated plasmas driving flux compression exists.

1.2.3. Helical instability experimental studies at 1 MA

Various 1-MA-scale experiments have explored helical instability growth from z pinches with applied B_z. Given the reduced peak current versus Z, not all pertinent imploding-liner physics can be evaluated in a single experiment. For example, implosion physics can only be studied using thin-foil liners (e.g., 100's of nm wall thickness). For a ~100 ns current pulse such foils are much thinner than the current-carrying skin depth, causing the foil to explode and increase in thickness by a factor of 100 or more. Such exploding-foil physics is absent in Z liners, which have wall thickness of 100s of µm, allowing current to initially flow in a surface skin layer and gradually diffuse inward. Therefore, if the experimenter chooses to study helical-instability initiation pertinent to "thick" metal, the z pinch is too massive to be imploded by a 1 MA current, and acceleration-driven MRT cannot be studied. Despite such limitations, a variety of key observations have been made on 1-MA-class drivers over the last decade, which are summarized next.

Experiments by Atoyan *et al*. [xli], evaluated non-imploding thin-foil liners for both dynamic (HRC-generated) and static (Helmholtz-coil-generated) B_z. For both types of B_z, extreme ultraviolet (XUV) emissions from foil surfaces were helical, and the handedness of the helical emissions flipped according to the orientation of the axial field. Images were gathered after peak current; thus, data cannot inform the physics of the seeding mechanism, and given the absence of implosion, results aren't applicable to MRT. Next, Yager-Elorriaga *et al*., produced a series of relevant papers [xlii, xliii, xliv], discussing instability development in the presence of static B_z for non-imploding, imploding, and exploding metallic-foil liners. For non-imploding liners, foils were placed directly over an insulating cylindrical support which was either flat/unseeded or helically seeded. For unseeded supports, m=0 modes grew in the absence of B_z, whereas helical modes grew when a 1-2 T static B_z was applied. For helically-seeded liners, application of a 1-2 T static B_z was shown to reduce instability development when the handedness of the field was opposite that of the seed perturbation. Complementary experiments allowed the foil to implode. The imploding plasma eventually stagnated upon a central dielectric support rod, and later expanded. Data show helical modes develop when B_z is applied, and the pitch angle of the helix increases as the liner implodes and then decreases after the liner stagnates on the support and rebounds radially outward, suggesting robust helical mode locking. Data are shown to be largely consistent with mode locking in thick liners, including the experimental observations in [xxiv] and in the analytic theory of Weis [xl], but neither of these thick-liner studies considered instability evolution after rebound. Finally, DSP physics was studied by Campbell et al [xlv, xlvi]. Here, thin metallic foils imploded by the DSP mechanism developed helical modes. Versus standard (B_z=0) pinches, MRT amplitudes were reduced for DSP-driven liners, with reduced growth as the field polarization angle ϕ_B was increased.

All aforementioned studies from 1-MA-class drivers focused on thin-foil liners, with results reported on the evolution of well-established instabilities and no direct observations of the initialization of the helical seed perturbation. By contrast, the experiments detailed in this report were designed to study the initiation of an ETI-driven helical seed perturbation on the surface of thick aluminum rods.

The work summarized in this report is an extension of previous thick-rod experiments [xlvii,xlviii ,xlix, l, li, lii, liii, liv, lv, lvi] and in particular "engineered defect (ED)" platform results [lvii]. ED-z-pinch targets are machined from 99.999% pure aluminum or "Al 5N" to a 1.00-mm-central rod diameter with ~10-nm-surface roughness. The 1.00-mm-diameter surface is then further machined to include pairs of 10-micron-scale quasi-hemispherical voids (i.e., EDs), which are the dominant current-density perturbation in the rod's surface. EDs emulate native defects (i.e., micron-scale voids and resistive inclusions) that commonly occur in metals, while ultrapure (i.e., defect-free), ultrasmooth aluminum provides a clean background for studying current-driven ETI evolution. Paired EDs provide insight into how isolated defects merge to form larger structures. The well-defined initial conditions in previous experiments enabled detailed comparison of data on ED-seeded ETI evolution with 3D MHD simulation [lviii, lix, lx]. Like these previous experiments, rods were pulsed to nearly 1 MA in 100 ns, but now the magnetic field at the rod surface was modified to include an axial component, $B_z(t)$, either through the addition of an HRC, or through use of an external, slow rising (static versus the timescale of Mykonos), Helmholtz coil pair.

1.3. Introduction to the electrothermal instability (ETI)

1.3.1. ETI from ED for B_z=0

Bare ED, B_z=0

The evolution of bare EDs in current-driven metal has been described in detail in Refs [lvii, lix, lx]. In the interest of keeping this report self-contained, we provide the following synopsis: as shown in Fig. 1(a), **j** diverts around the ED, similar to hydrodynamic flow around an impermeable sphere, and amplifies around the equator of the ED, driving enhanced Joule heating there. The resulting pressure gradient, seen in Fig. 1(b), causes melted metal to flow along $-\nabla p$ and focus azimuthally towards the ED center, forming a bump with similar electrical conductivity σ to the surrounding metal. Drawing on the analogy between electrical current and hydrodynamic flow, **j** is drawn into the bump (rather than away from the ED – contrast the **j** flow patterns in Figs. 1(a) and 1(c)), amplifying at the poles of the bump [lx, **Error! Bookmark not defined.**], resulting in amplified Joule heating there, as seen in Fig. 1(c). Consequently, peak Joule heating has shifted from the ED equator to the poles. Enhanced Joule heating from the poles drives higher temperature at the "hot spots" indicated in Fig. 1(e), leading to enhanced emissions which should be observable experimentally, as indicated by the synthetic visible emission image in Fig. 1(g), generated from the post-processing code SPECT3D [lxi]. The brightly emitting spots at the pole locations are referred to in this report as "polar emission" (note it was previously referred to as "cat eye" emission in [lvi]). As illustrated in Fig. 1(f), the hot spots responsible for polar emission eventually explode radially outward, resulting in lower-density-plasma plumes that develop ETI filaments directed along the direction of current flow (i.e. along z), which eventually dominate emission (see Figs. 3(e,f) of [l] and Fig. 6 of [lix]). After plasma filaments form, emission structures in the underlying metal can no longer be experimentally observed via visible-light self-emission imaging.

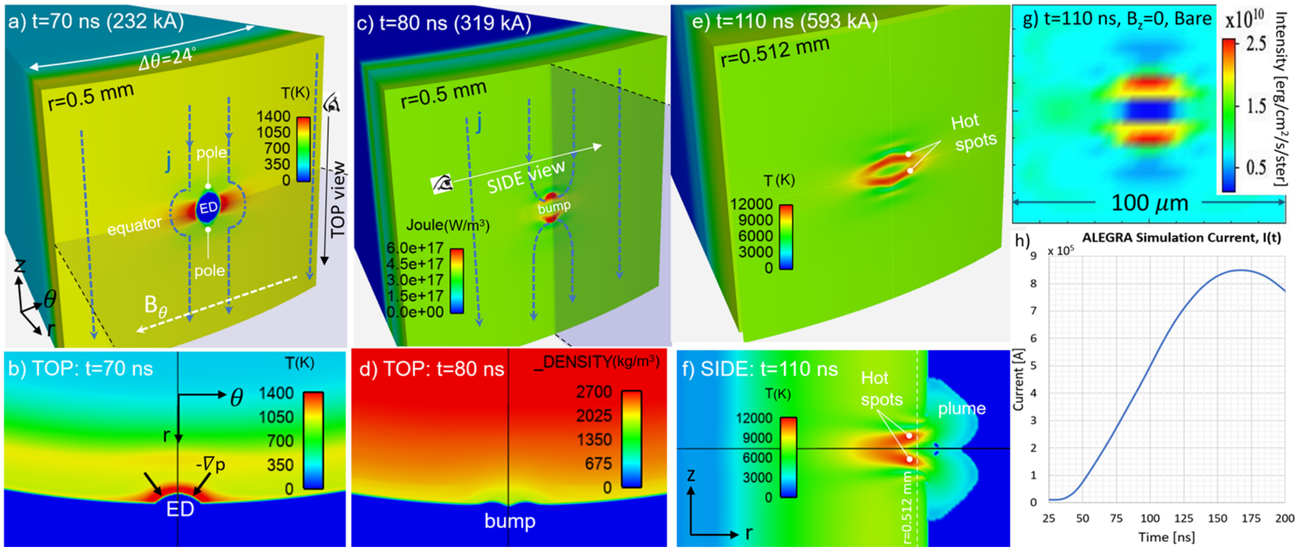

Figure 1. **3D ALEGRA simulation of a bare/uncoated engineered defect (ED) for the case B_z=0. The computational wedge is periodic in axial (z) and azimuthal (θ) directions. (a) Early temperature (T) of the rod surface (r=0.5 mm). Blue lines represent current density (j) streamlines, diverting around the ED and amplifying around its equator. Dashed black lines bound a fixed-z plane used to visualize the top view. b) Top view of ED, showing enhanced T around the ED equator and an azimuthally focusing pressure gradient. The resulting expansion transforms the ED pit into a bump by t=80 ns. c) Joule heating on rod surface. Enhanced expansion at the ED equator generates a bump – see top view in d) – which causes j to flow into the bump, amplifying at its top and bottom. Consequently, Joule heating is also enhanced there, driving hot spot formation – see (e). Hot spots explode outward, as seen in the side view in f), which cuts through the ED center at a fixed-θ plane. (g) Synthetic visible emission image from SPECT3D, which solves the radiative transfer equation along lines-of-sight through the ALEGRA computational grid. At each volume element along the line-of-sight, the frequency-dependent absorption and emissivity of aluminum are computed under the assumption of local thermodynamic equilibrium (LTE). The resolution in the synthetic images is 4 μm (similar to experimental imagers) and the range of photon energies is 1.3-4.6 eV. (h) Current profile used in ALEGRA simulations.**

Dielectric-coated ED, B_z=0

Liners have shown improved implosion stability when coated with 10s of microns of dielectric, due to the dielectric tamping of ETI-driven surface expansion, which reduces the seed for subsequent MRT growth [**Error! Bookmark not defined.**, lxii]. When studying ED evolution, dielectric coatings have an added benefit of delaying surface plasma formation, thus enabling extended study of strata formation and evolution in condensed metal. As a result, simulations have examined coated ED both in isolation and configured in closely-spaced pairs. Figure 2 shows a simulation of an isolated ED which has been filled and coated with a 40-μm thick layer of dielectric (Lexan). Recall that from Figs. 1(c,d) that by t=80 ns, the bare ED has transformed into a bump, qualitatively altering **j** and resulting in the polar emission seen in Fig. 1(g). By contrast, Figs. 2(a,b) show that at t=80 ns, the coated ED remains a pit because the coating has tamped the hydrodynamic expansion necessary for bump formation. This prevents development of the polar overheating pattern, seen from bare-ED in Fig. 1(c), so that by t=110 ns, the heating pattern for the coated ED is qualitatively different (see Fig. 2(c)).

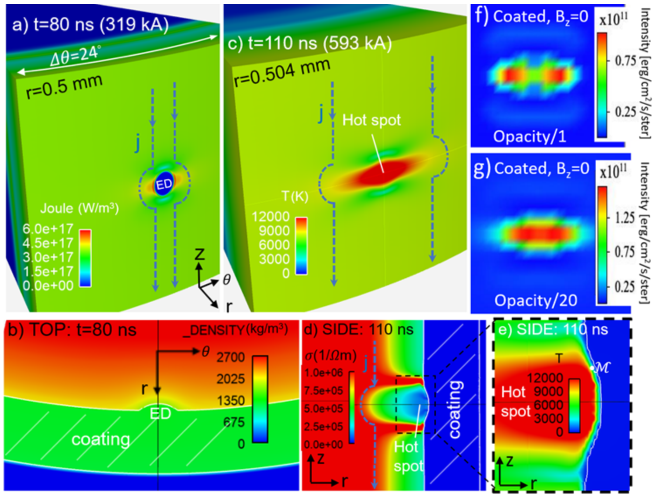

Figure 2. Dielectric-coated ED, B_z=0. a) Joule heating on the surface of an aluminum rod at t=80 ns. By contrast to Fig. 1(c), j still diverts around the ED, because the coating tamps pit expansion. Hence Joule heating peaks at the ED equator, rather than at the poles, as in Fig. 1(c). b) Top view of coated ED (see Fig. 1(a) for viewing orientation). Unlike the bare case shown in Fig. 1(d), the pit has not converted to a bump. c) Hot spot driven by coated ED. Unlike the bare case shown in Fig. 1(e), T does not exhibit "polar emission." d) Side view of electrical conductivity σ (see Fig. 1(c) for viewing orientation) shows that the coating tamps hot spot explosion and plume formation. The hot spot bulges radially outward, but because of low σ there, j does not get pulled into the bump; rather, j streamlines (in blue) divert around the hot spot, so polar emission never develops. e) magnified side view of hot spot. $\mathcal{M}$ represents a mixed Al-dielectric cell with high opacity, which prevents bright emission from hot spot being visible. Simulated visible emission images at t=110 ns post processed in SPECT3D with unmodified opacity in (f). In (g) the opacity has been reduced by a factor of 20, which increases the photon mean free path, allowing photons born from the hot spot to transport through mixed cells, resulting in bright emission from the hot spot location. See the Fig. 1 caption for a discussion of how synthetic images are generated.

As seen in the side view in Fig. 2(d), thermal pressure in the hot spot has grown sufficiently to transform the pit into a bump, despite the presence of the coating. In the bare case shown in Figs. 1(c,d), the bump consists of relatively cool (3300 K) and dense (1900 kg/m^3~0.7ρ_{solid}) melted metal with electrical conductivity σ similar to surrounding metal. Consequently, the hydrodynamic analogy with electrical current flow remains applicable, and **j** is pulled into the bump, leading to polar emission. In the coated case, the bump does not form until later, when it has reached temperature (~14,000 K) and density (~500 kg/m^3) such that σ in the bump is significantly lower than surrounding rod material, as seen in Fig. 2(d). Hence, **j** flows around the bump rather than into it, and polar emission does not develop.

Figure 2(e) shows a magnified view of the hot spot, highlighting details within the dashed black box of Fig. 2(d). At the interface between Al and the dielectric coating are mixed Al-dielectric cells with temperature intermediate between hot Al and cold dielectric. According to the opacity tables used, the density (~700 kg/m^3) and temperatures (~8000 K) correspond to high Al opacities (photon mean free path~30 nm at 3 eV energy). Hence, emission at these locations is dominated by the relatively cool mixed cells, resulting in dim emission at the hot spot location, as seen in Fig. 2(f). Because of uncertainties in the numerical accuracy of mixed cells, as well as the high opacity values themselves, we also ran SPECT3D with 20 times lower opacity, increasing the photon mean free path to 0.6 μm (slightly larger than resolution cell size). In this case, photons born from the hot spot can transport through the mixed cells, resulting in bright emission at the hot spot location (see Fig. 2(g)), which agrees better with experiment (see [lvi]).

ETI strata formation between azimuthally-separated and dielectric-coated ED pairs for $B_z=0$ has also been simulated (Fig. 3) and shows that **j** redistributes around each ED, adding constructively between them to drive local overheating and eventually ED-pair merging. Early in time at t=80 ns, EDs behave nearly independently; the single ED pattern (see Fig. 1(a)) is repeated about each ED, with T and Joule heating peaked at the ED equators. However, superposition of diverted **j** leads to a slight increase in j, Joule heating (Fig. 3(c)), and T (Fig. 3(a)) between EDs. In addition, peak T at the sides of the EDs corresponds to a reduction in σ there, causing the low-σ ED region to widen, increasing ED-pair interaction.

By t=110 ns, redistribution of **j** between the EDs, combined with lower σ there, results in peak Joule heating occurring between EDs (Fig. 3(f)), in turn driving a merged temperature strip (Fig. 3(d)), which we can identify as an ETI striation. At this point, **j** preferentially flows along the lower resistance "outer" paths around the striation, rather than the low-σ "inner" paths (Fig. 3(e)) between EDs. Nevertheless, Joule heating between EDs remains elevated due to low σ. The striation should be experimentally diagnosable, as indicated by the synthetic emission image (Fig. 3(g)).

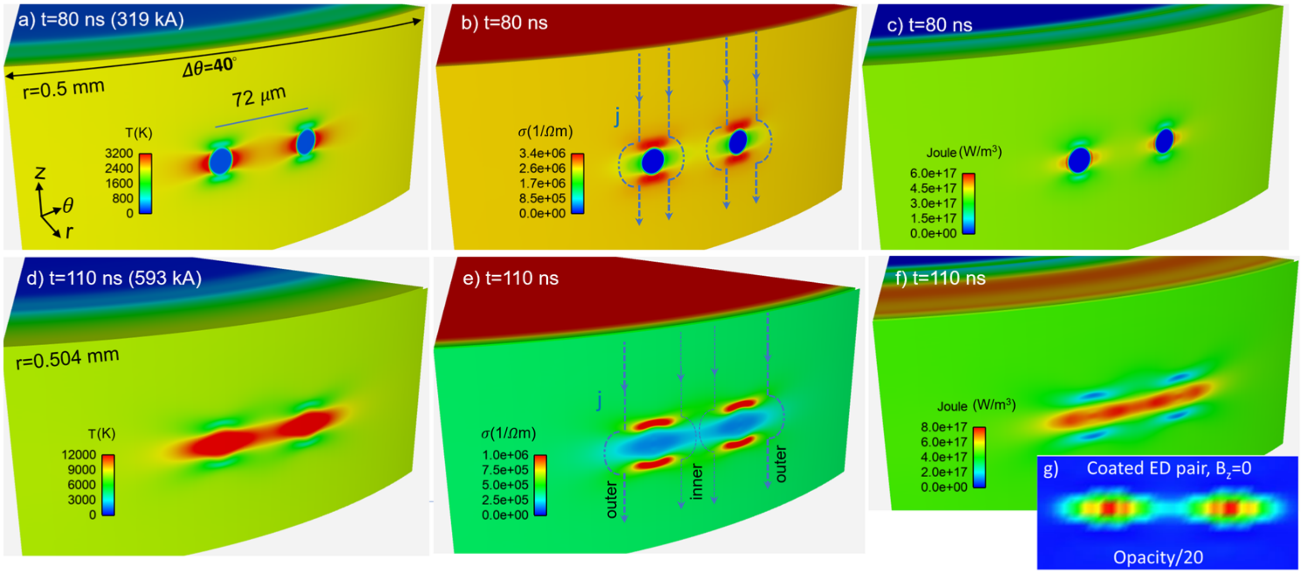

Figure 3. **ED pair separated by 72 *μ*m and coated with 35 *μ*m of dielectric (not shown). a),b),c) Temperature, electrical conductivity, and Joule heating, respectively, on the surface of an aluminum rod at t=80 ns. Blue lines illustrate streamlines for current density j. d),e),f) Same quantities plotted at t=110 ns. EDs have merged due to enhanced Joule heating between EDs. Thinner j lines between EDs illustrate that j redistribution between EDs is weaker due to low *σ* there; j prefers to flow around the merged low-*σ* striation. (g) displays a synthetic self-emission image of the coated ED pair at 110 ns. See the Fig. 2 caption for a discussion of how synthetic images are generated.**

1.3.2. ETI from ED for dynamic B_z (B_z provided by HRC)

Bare ED, B_z provided by an HRC

In the presence of dynamic $B_z(t)$ generated, for example, by a helical return can (HRC), from $\nabla\times E=-\partial B/\partial t$, azimuthal j_θ will be generated on the rod's surface via eddy current induction, shielding the interior of the metal from the externally pulsed $B_z(t)$. This will result in helical current flow on the rod's surface. In the limit where the current skin depth δ is much smaller than rod radius, the current density vector **j** is approximately perpendicular to the magnetic field vector **B**. For an ED placed on the surface of the rod, the general evolution is predicted to be identical to that for $B_z=0$, but now, with the helical (rather than axial) **j**, the heating pattern will also rotate. This scenario is illustrated in Fig. 4, which is identical to the bare ED shown in Fig. 1, but now with an external $B_z(t)=0.268B_\theta(t)$, or $\phi_B=15°$ applied at the rod's surface. In Figs. 4(a,b), **j**, **B**, and T each rotate by ϕ_B relative to the $B_z=0$ case in Figs. 1(a,e). As a result, the polar emission pattern predicted in the synthetic emission image also rotates by ϕ_B (compare Fig. 1(g) to Fig. 4(c)); such significant rotation should be diagnosable in experiments.

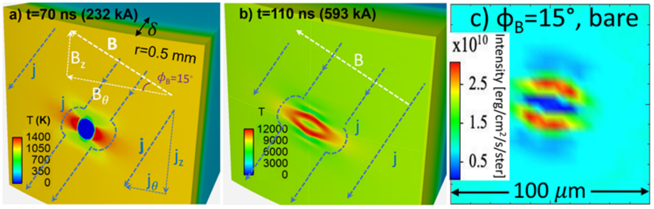

Figure 4. **Bare ED in presence of dynamically applied $B_z(t)$. a) Azimuthal j_θ is generated on the rod's surface via eddy current induction, shielding the interior of the metal from the externally pulsed $B_z(t)$. Far from the ED, j is helical and aligned perpendicular to B, so long as the skin depth δ is much smaller than the rod radius. Close to the ED, the j pattern is identical to the $B_z=0$ case in Fig. 1(a) but rotated by ϕ_B. b) Later in time, the polar temperature topography is also rotated by ϕ_B, resulting in the rotated synthetic emission image in (c) also at t=110 ns. See the Fig. 1 caption for a discussion of how synthetic images are generated.**

Dielectric coated ED, B_z provided by HRC

As discussed for bare ED, in the presence of HRC-generated dynamic $B_z(t)$, azimuthal j_θ will be generated on the coated rod's metal surface via eddy current induction, resulting in helical current flow. **j**, **B**, and T will all rotate by ϕ_B relative to the $B_z=0$ case, and as a result, the emission patterns predicted in the synthetic emission image also rotate by ϕ_B. As shown in Fig. 5, simulations show that the same picture holds in the coated case in that the heating and emission patterns about ED rotate by ϕ_B to align with the helical **B**. In the case of closely spaced ED pairs, we expect EDs to be more likely to merge when they are aligned to ϕ_B, rather than horizontally, as in the $B_z=0$ case.

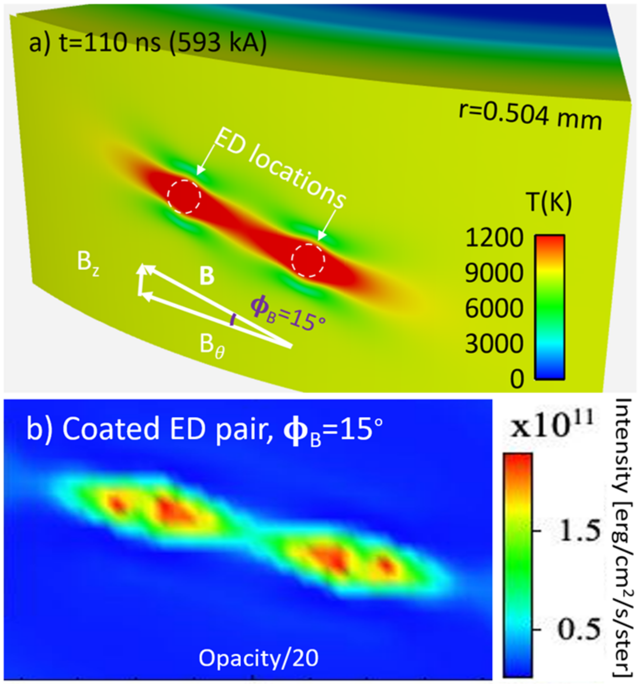

Figure 5. **Coated ED pair in the case of dynamically applied $B_z(t)$. The pair is separated by 72 μm and $\phi_B = \phi_{ED} = 15°$. a) Temperature near the surface of the rod. b) Simulated visible emission from the ED pair.**

1.3.3. ETI from ED for static B_z (B_z provided by Helmholtz coils)

In the presence of static B_z (B_z=constant on the 100 ns timescale of the Mykonos current) generated, for example, by a Helmholtz coil pair, the mechanism by which asymmetric j_θ is generated from an ED is different from the dynamic B_z case. Here, an external coil applies the axial field to the rod on a millisecond timescale, and thus the B_z field is fully diffused by the time the relatively fast axial current arrives, and eddy current induction does not alter the current density at the surface of the rod. Instead, a different mechanism drives asymmetric current density and ETI heating near the ED as indicated by Fig. 6. In Fig. 6, the current density associated with the 100 ns current pulse is indicated by black dashed lines, and is diverted around the ED, generating j_θ of varying strength and orientation as dictated by location around the perimeter of the ED. Note, however, that this diversion generates symmetric j_θ. Eventually, the surface of the rod will expand radially outward. This radial velocity and axial magnetic field cross product results in motional EMF as governed by Ohms law, generating a small azimuthal current density $\delta j_\theta = \sigma v_r B_z$. As shown in the figure, this azimuthal current density will increase j_θ at the "southwest" and "northeast" regions of the ED, while decreasing j_θ at the "northwest" and "southeast" regions of the ED.

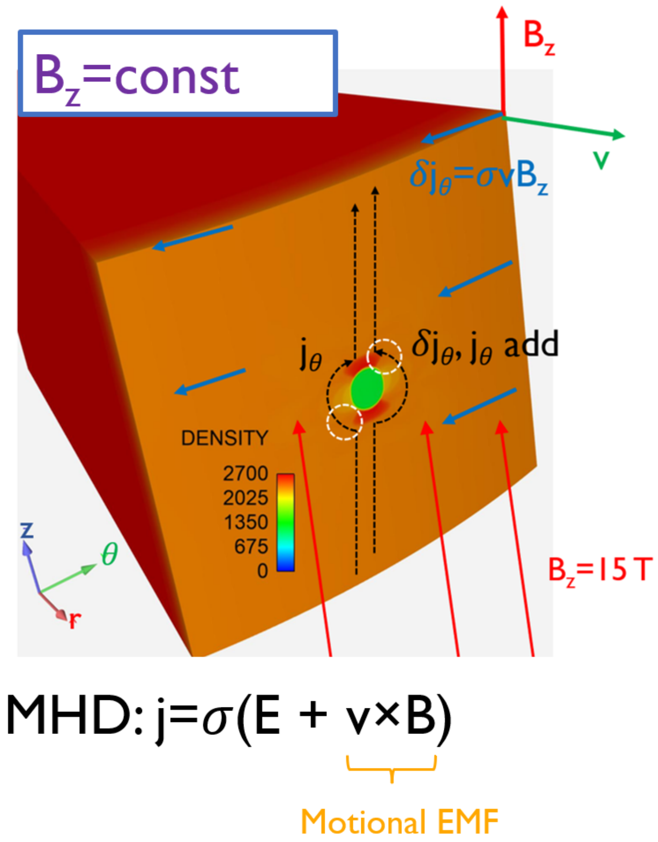

Figure 6. Asymmetric current density around an ED for the case of static axial field (via a Helmholtz coil). The radial velocity and axial magnetic field cross product results in motional EMF as governed by Ohms law, generating a small azimuthal current density $\delta j_\theta=\sigma v_r B_z$. This azimuthal current density will increase j_θ at the "southwest" and "northeast" regions of the ED, while decreasing j_θ at the "northwest" and "southeast" regions of the ED.

ETI evolution around the ED will be impacted by this assymetric current density, resulting in a rotation of the heating topography near the ED, as by the simluation temperaure maps and assoicated synthetic self-emission images shown in Fig. 7. These results (for bare ED) indicate the resulatant rotation of the heating topography is much more sublte for static B_z than it is for dynamic B_z (at least for those conditions expected to be achieved in Mykonos experiments). Given the small predicted impact on the standard quasi-hemishperical ED, simulations of hemispherical (deeper/higher curvature) ED were also run. These simulations indicate stronger and likely experimentally observalbe rotation of the ETI heating topography. In response to these simlulation predictions, targets with hemispherical ED were design for static B_z experiments. Such targets are discussed in detail in Section 5.1.

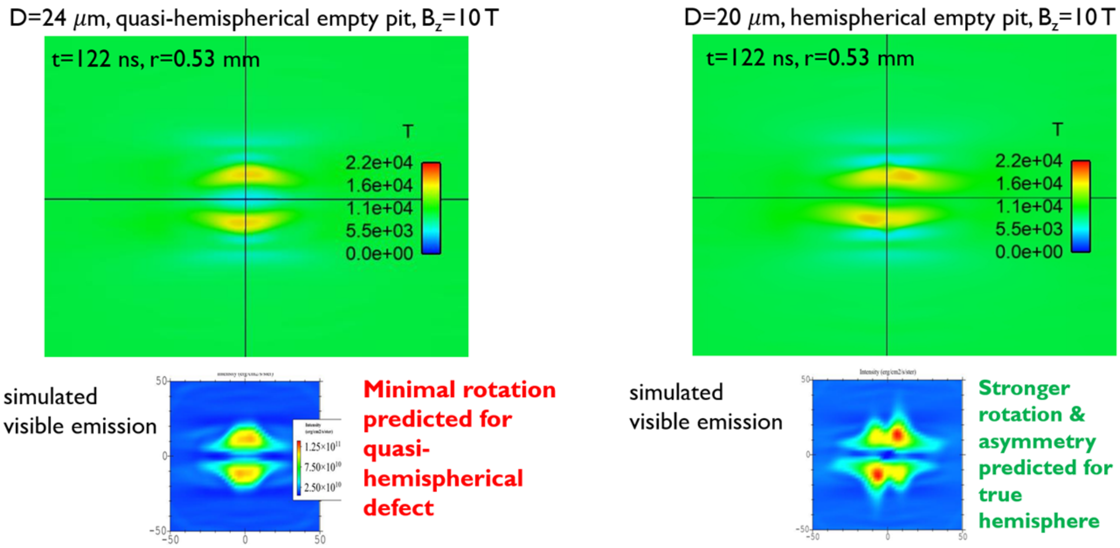
D=24 μm, quasi-hemispherical empty pit, B_z=10 T

D=20 μm, hemispherical empty pit, B_z=10 T

simulated visible emission

Minimal rotation predicted for quasi-hemispherical defect

Stronger rotation & asymmetry predicted for true hemisphere

Figure 7. Simulations of heating from quasi-hemispherical (left) and true hemispherical (right) ED for the case of statically applied axial field. Heating topography rotation is subtle in both cases, but is predicted to be diagnosable in the case of true hemispherical ED. This simulation prediction led to change in the ED design.

2. FACILITY INFRASTRUCTURE—LARGE DIAMETER VACUUM CHAMBER WITH RE-ENTRANT PORTS

2.1. Existing small diameter ETI vacuum chamber

An ETI vacuum chamber, designed for the first ED experiments on Mykonos, was small diameter to reduce the distance between the physics target and imaging diagnostics (Fig. 8). This was motivated by the desire to diagnose nonuniform ohmic heating of condensed metal and vapor at low (sub-eV) temperature. At such temperatures, the low intensity self-emission from the z-pinch makes radiometric and self-emission measurements challenging (low signal levels). By moving the diagnostics closer to the physics load, a larger solid-angle is captured (for a given lens diameter), signal levels are higher, and lower temperature emissions can be measured. As most diagnostics of interest are sensitive to visible light, the chamber included 7 optical viewports. 3 had 2.5” diameter clear glass openings (larger than the 2.3” opening of the long-distance microscope (LDM), which is commonly used for ICCD imaging in these experiments) and 4 have 2” diameter clear glass openings. Microscope slide “debris shields” are placed between the load and the windows to protect the windows from debris (e.g., aluminum vapor). Debris shields are replaced after every experiment and vacuum windows are generally not damaged. One oversized port shown in the right-hand image of Fig. 8 is used for vacuum pumping.

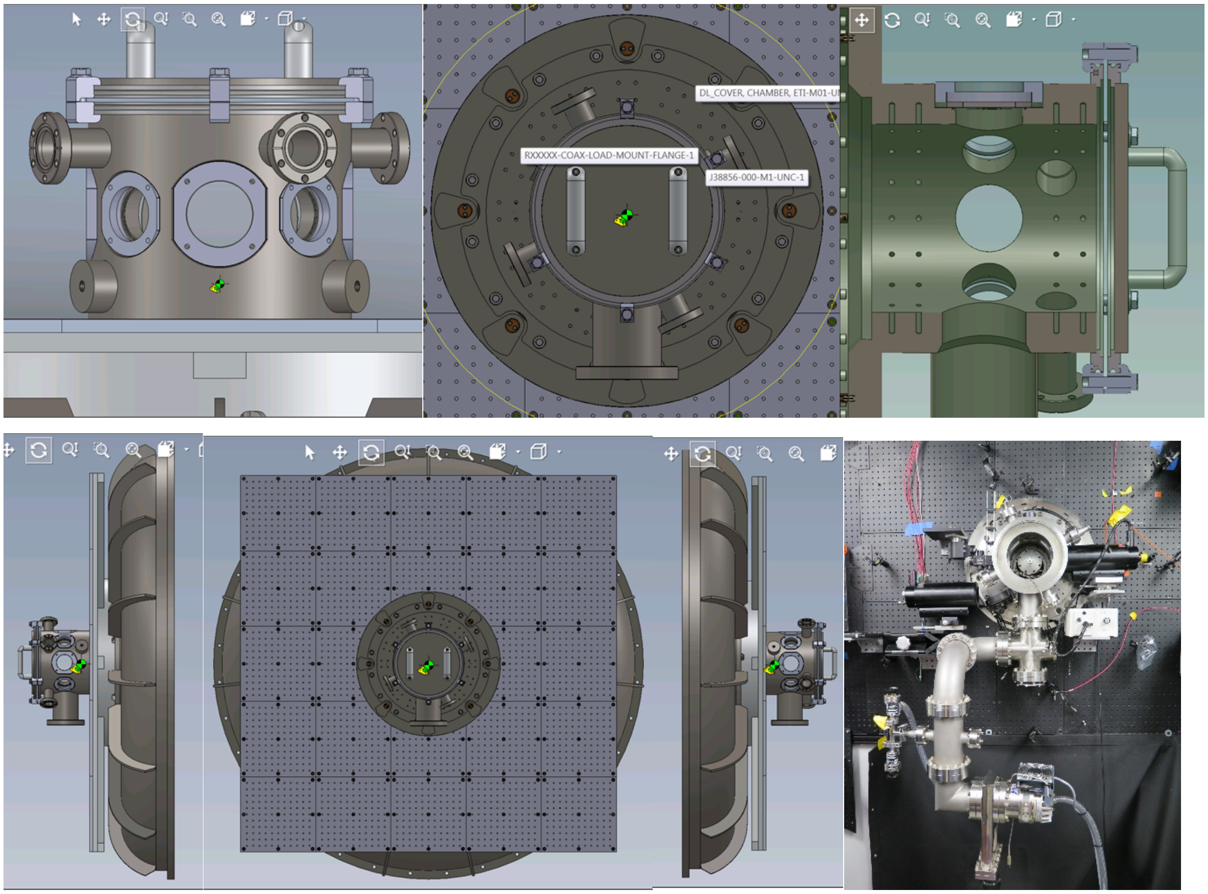

Figure 8. Various views of the diagnostic chamber and diagnostic framework added to the Mykonos Facility as part of an earlier LDRD project (Project 200269).

While functional from a scientific perspective, the small diameter ETI chamber was operationally cumbersome. As shown in Fig. 9, the small diameter portion of the chamber was welded onto a larger diameter flange to enable vacuum sealing to Mykonos (o-ring indicated by yellow arrows). To access and refurbish the Mykonos insulator (blue arrows), which is required every 6-8 downline shots, the Mykonos anode (red arrows) must be removed, and this required removal of the vacuum chamber. This is a unique requirement of this small diameter chamber (the anode can be removed through the interior of larger diameter chambers, without need for chamber removal) which created significant delays, because not only did the chamber itself require removal, but so too did any diagnostics which restricted chamber removal. Furthermore, the small diameter chamber was incompatible with the Helmholtz like coils which would be needed for static field experiments (see Section 4 for a discussion of in-chamber coils). Therefore, the design of a new ETI chamber was prioritized early in the project. The small format chamber has since been decommissioned and has in fact been modified for use on a different research project and is no longer compatible with the Mykonos Facility.

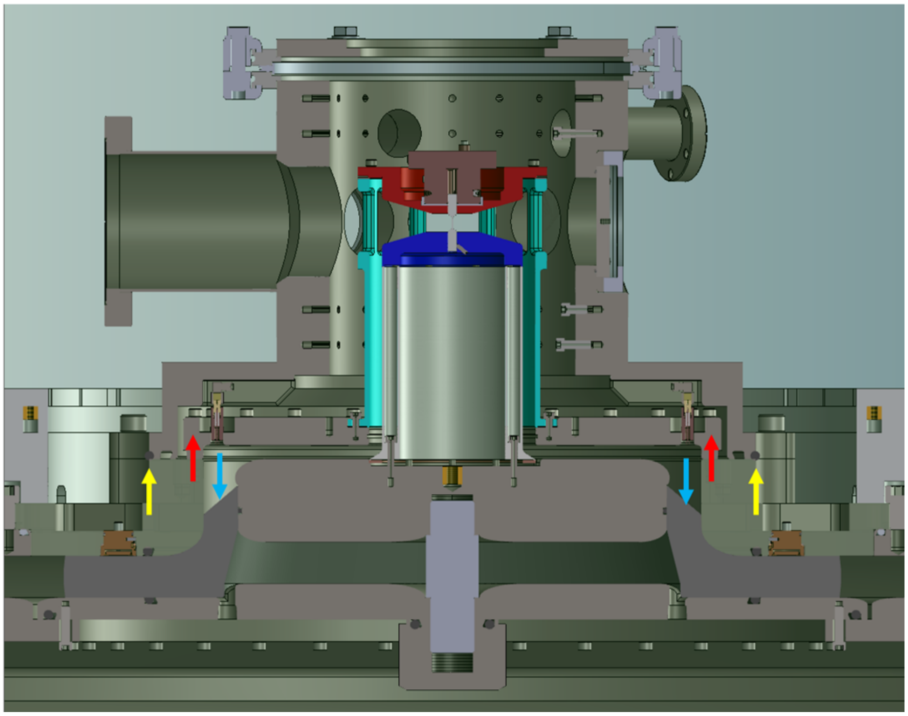

Figure 9. Cross section of small diameter ETI vacuum chamber, indicating why the chamber must be removed to allow for Mykonos insulator cleaning.

2.2. New large diameter vacuum chamber with re-entrant viewports

A large (standard) diameter vacuum vessel was developed to alleviate the operational challenges associated with the small diameter ETI chamber, and also allow sufficient space for in-chamber Helmholtz coils for static field experiments. But it remained important that the large solid angle diagnostic access to the physics target was preserved. Therefore, a chamber was developed to allow the option of re-entrant ports at 3 of the 4 cardinal directions (with the fourth reserved for a large diameter vacuum port). The cartoon view in Fig. 10 shows the functional elements of the chamber’s re-entrant port design.

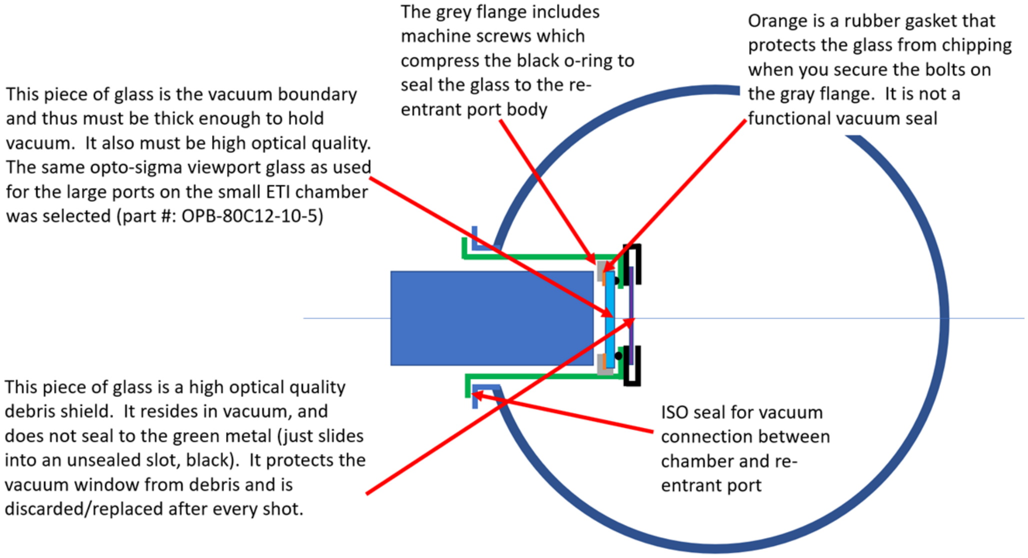

The grey flange includes machine screws which compress the black o-ring to seal the glass to the re-entrant port body

Orange is a rubber gasket that protects the glass from chipping when you secure the bolts on the gray flange. It is not a functional vacuum seal

This piece of glass is the vacuum boundary and thus must be thick enough to hold vacuum. It also must be high optical quality. The same opto-sigma viewport glass as used for the large ports on the small ETI chamber was selected (part #: OPB-80C12-10-5)

This piece of glass is a high optical quality debris shield. It resides in vacuum, and does not seal to the green metal (just slides into an unsealed slot, black). It protects the vacuum window from debris and is discarded/replaced after every shot.

ISO seal for vacuum connection between chamber and re-entrant port

Figure 20. Cartoon showing the functional elements of the re-entrant vacuum port design

The LDM is represented by the large blue rectangle in the cartoon above. It enters the re-entrant port through an optical kinematic mount (Edmund Optics #35-474, see Fig. 11), traditionally used to hold/tip/tilt large diameter mirrors. The mount was modified by adding rubber tipped set screws to pinch the outer diameter of the LDM body/tube to secure it. In this way, the LDM can be positioned within the re-entrant port at various radial distances from the target. In general, the LDM is positioned as close to the target as possible (deep within the re-entrant port tube), resulting in a distance between the LDM window and target of about 6 inches. Once positioned within the re-entrant port, the vernier tip/tilt adjustments of the mirror mount is used for precise pointing of the LDM, allowing adjustment of the image placement on the downstream ICCD sensor. Focusing is accomplished via standard LDM adjustments. To allow removal of the anode plate for insulator refurbishment, the re-entrant ports must be removed but removing the LDMs from the re-entrant port but is not necessary. In practice, when re-installing the ports/LDMs after refurbishment, the target is brought back into focus on the ICCD sensor with only a few minutes of effort.

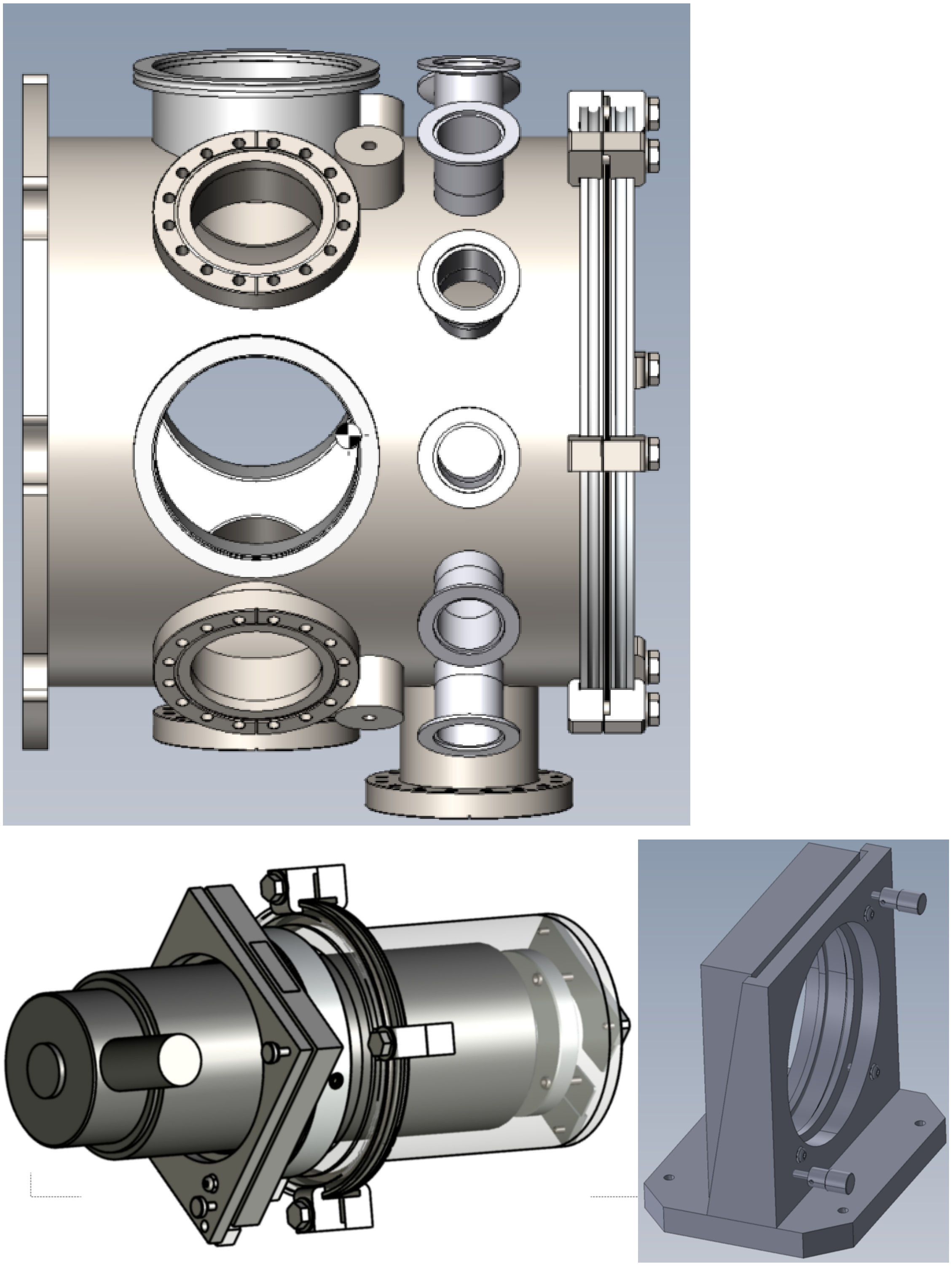

Figure 11. CAD view of the large diameter vacuum vessel (top), which includes large ISO flanges which accept the re-entrant port tubes (bottom left). The port tubes are designed with external brackets which allow the user to bolt on a modified tip/tilt mount, which both secures the LDM, and allows precise adjustments to LDM pointing (bottom left and right).

The re-entrant ports were design for compatibility with QM-100 LDMs, but other diagnostics are also compatible, including optics used for radiometry and PDV. The design of the LDM re-entrant port assembly can be accessed in drawing J92703, which is included as Fig. 12.

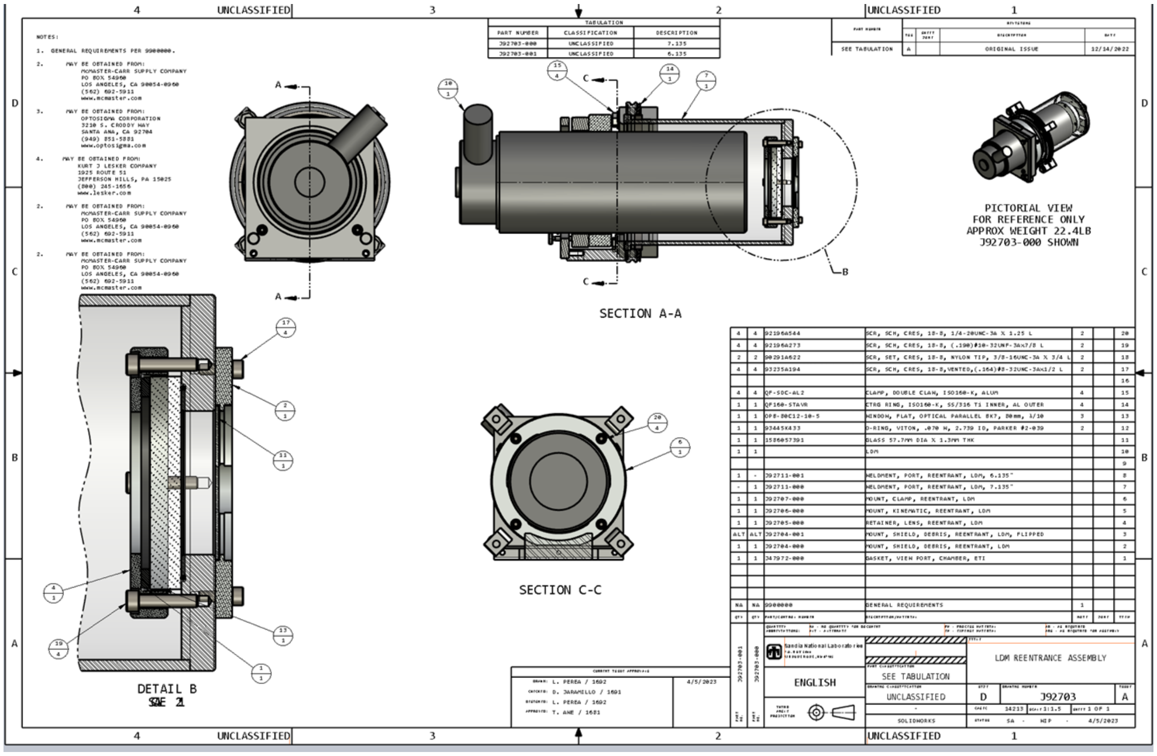

Figure 32. Assembly drawing for the LDM re-entrant assembly.

3. ETI+DYNAMIC AXIAL FIELD—EXPERIMENTAL RESULTS

In this section we summarize dynamic axial field studies, including experimental setup and results. We do so, largely by reproducing and briefly describing the figures from a recent publication which can be found at: https://doi.org/10.1063/5.0279628

We urge interested readers to access the full article for more information.

3.1. Experimental design and commissioning

A variety of recent studies [lvii, lvi] on the Mykonos Facility have used powerflow hardware similar to the design shown in Fig. 13(a), which includes a cylindrical coaxial feed to deliver current to the z pinch target. When adding $B_z(t)$, to preserve peak current, the HRC cannot be too inductive, and so must be much smaller radius than the original SRC, which is accommodated by a newly designed "swooping" MITL (Fig. 13(b)) with an AK gap that falls from 9.0 mm to 3.4 mm to limit inductance. A new small-radius and low-inductance SRC (Fig. 13(c)) couples to the same swooping MITL. Mykonos machine current data, I(t), from the swooping feed are shown in Fig. 13(d), where the 12 red curves are for shots using a ϕ_B=15° HRC while the 11 black curves are for shots using an SRC. Data indicate minimally shorter rise time for the lower inductance SRC. Peak currents vary by nearly 100 kA over this dataset.

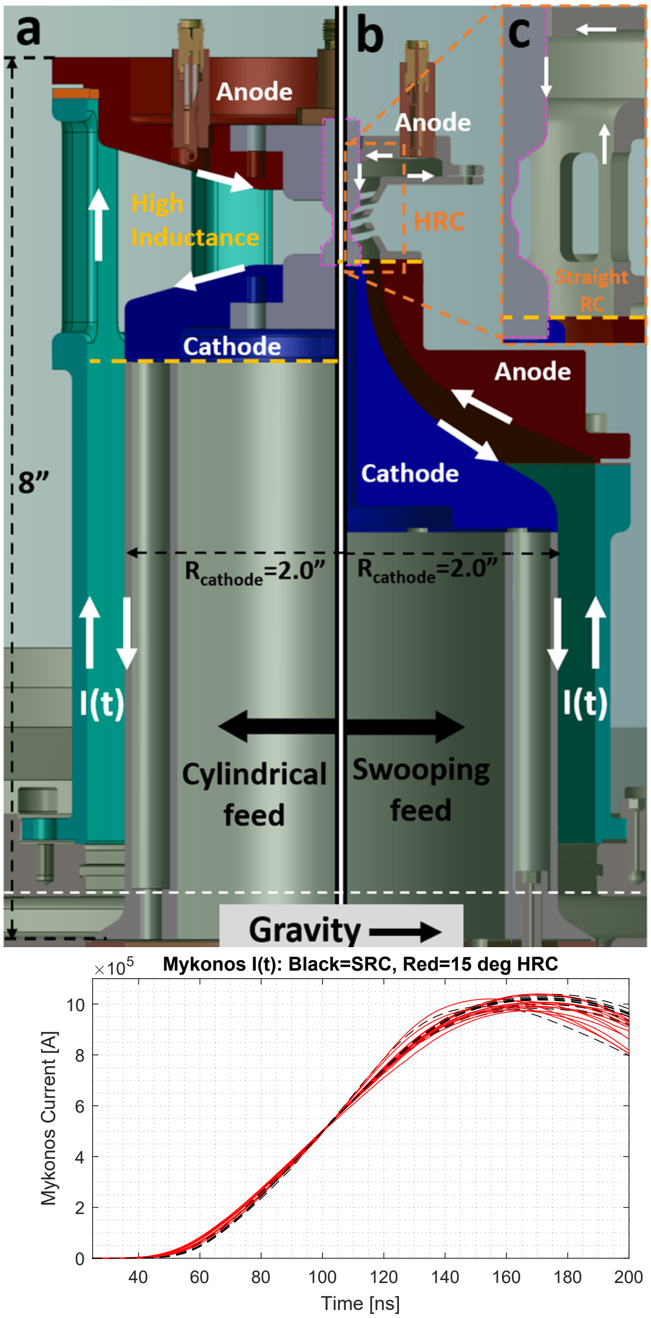

Figure 13. Mykonos powerflow hardware. (a) Cylindrical feed used in earlier ETI studies. (b) New, "swooping" current feed developed to transition to a small radius HRC (b) or small radius SRC (c). The direction of current flow is indicated by white arrows and the physics target is outlined in dashed-pink lines. A more detailed view of the target region is provided in Fig. 9. (d) Mykonos machine-current curves for experiments using the swooping feed and either a ϕ_B=15° HRC (Red) or SRC (dashed black).

HRCs (Fig. 13(b) and Fig. 14(a,b)) were machined from 304 stainless steel and were designed to meet a variety of experimental requirements. (1) The HRC must allow diagnostic imagers to view the full 1.00-mm-diameter physics region of interest of the target (indicated by red in Fig. 14(a)) at two azimuthal locations separated by 180°. (2) It must provide $\phi_B(t)$=15° field polarization at the target's 1.00-mm-diameter surface. (3) The strength of the axial field about the central 1-

mm height of the physics target must not vary by more than 10% to provide uniform ϕ_B. (4) The HRC geometry should prevent both shorting between the HRC and target as well as interhelix shorting through the time of peak current. The 4 requirements are sometimes conflicting in the sense that satisfying one condition may challenge another.

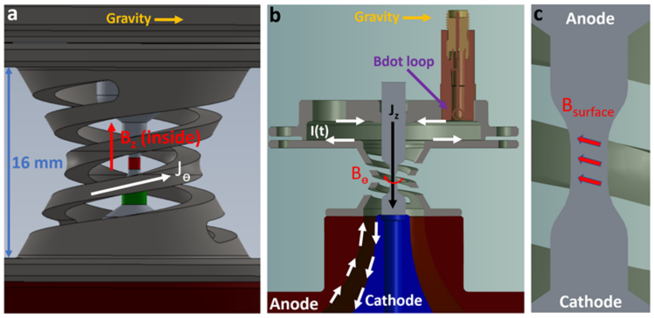

Figure 14. **Field orientation generated by the HRC. (a) Orientation of current flow around the HRC, generating a positive axial field component. Note that the red-colored 1.00-mm-diameter surface can be fully viewed from 0° and 180° diagnostic lines of sight. (b) Orientation of current flow downward through the z pinch, generating a negative azimuthal field component. (c) Magnetic field orientation on the 1.00-mm-diameter surface of the z pinch, which is 15° rotated from horizontal (ϕ_B=15°) for the HRC shown. While the target is shown vertically, the Mykonos hardware is actually horizontally oriented. The direction of gravity is indicated in (a,b).**

Engineered defect targets of the same "barbell" profile (Fig. 14) and general machining process as described in [lvii] were used in dynamic axial field experiments. Here, however, 4 ED pairs were included on the 0° and 180° sides of the target. All individual quasi-hemispherical ED were machined similarly, with rim diameter D_{rim}=24 µm and 6 µm center depth. Details of the patterns are shown in Fig 15(a). The 0° side of the target contains pairs of ED with center-to-center pair angle ϕ_{ED} of +0°, +7°, +11°, and +15° from horizontal. The 180° side contains angled pairs is of opposite slope (ϕ_{ED} of -0°, -7°, -11°, and -15°). The center-to-center spacing of each defect pair was 72 µm, regardless of ϕ_{ED}. The ϕ_{ED}=±0° pairs were nearest to the anode, while the ϕ_{ED}=±15° pairs were nearest to the cathode.

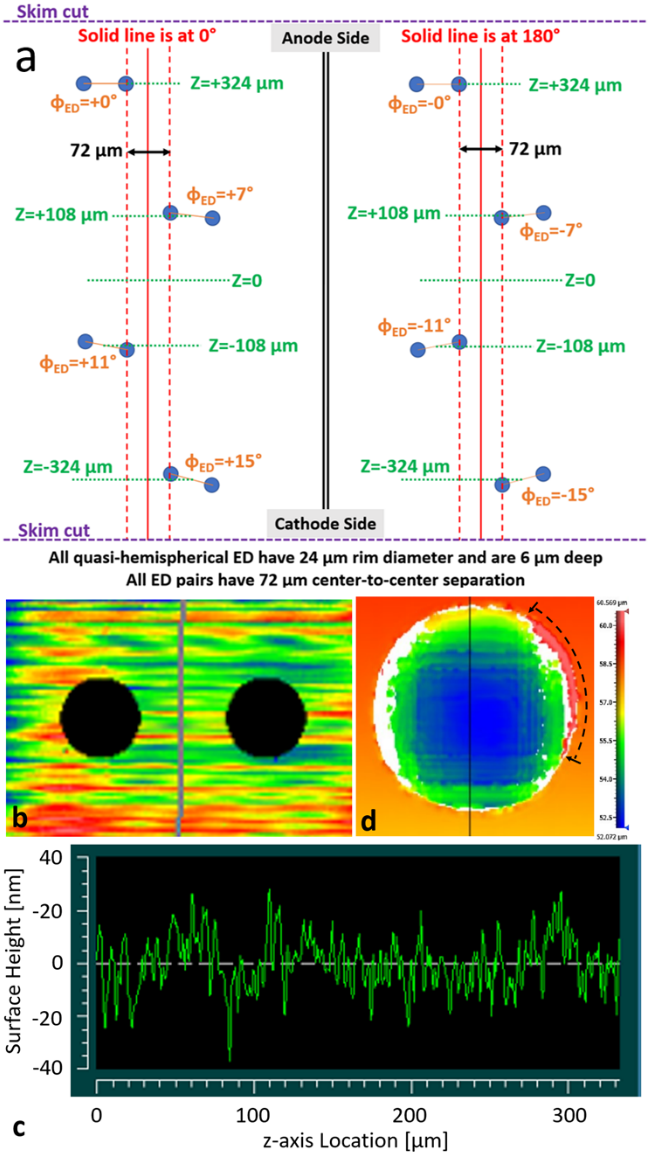

Figure 15. (a) ED pattern specification for experimental z pinch targets. (b) Interferogram of the azimuthally correlated machining grooves on surfaces near ED (the ED profiles have been masked as indicated by the black circles). (c) Surface height profile about the grey line in (b), extended, showing the height of surface machining grooves near ED (d) Interferogram of an ED, showing imperfections about the ED rim. White regions indicated data loss about locations of the ED where light reflection was insufficient for the measurement. The black dashed arc and arrows indicate the extent of a flap of material inside of the rim diameter and at nearly the same height as the nearby surface, which is likely a burr that was folded back over the ED rim rather than removed during the skim cut.

3.2. Experimental Results

3.2.1. *Bare/uncoated ED— Θ_{pole} rotation toward ϕ_B*

Data obtained from *bare* (uncoated) ED targets with either ϕ_B=0°or ϕ_B=15° magnetic field polarization demonstrate that the ETI-driven polar heating about EDs aligns towards ϕ_B. To determine Θ_{pole}, we locate the center coordinates of both poles generated by a single ED, and then calculate the angle of the line connecting the two pole centers. The full analysis procedure is detailed in the publication. In this LDRD report, we summarize only the results.

Θ_{pole}, data from the 90% contours (see paper for discussion how contour values were calculated) of 81 ED are included in Fig. 16, with 43 ED from ϕ_B=0° experiments and 38 ED from ϕ_B=15° experiments. Θ_{pole} measurements associated with each ED are color coded by ϕ_B, and separately by whether data originates from the L or R ED within a pair (see legend). 15 of the 16 combinations of ϕ_B, ϕ_{ED}, and (L or R) are represented in the plot (no ϕ_B=15°, ϕ_{ED}=0°, L emission data were gathered which were compatible with the analysis method). The fifth panel combines data from all pair angles and presents 4 averages (with 1 standard deviation presented as error bars) for the four primary cases: (ϕ_B=0°||L), (ϕ_B=0°||R), (ϕ_B=15°||L), (ϕ_B=15°||R).

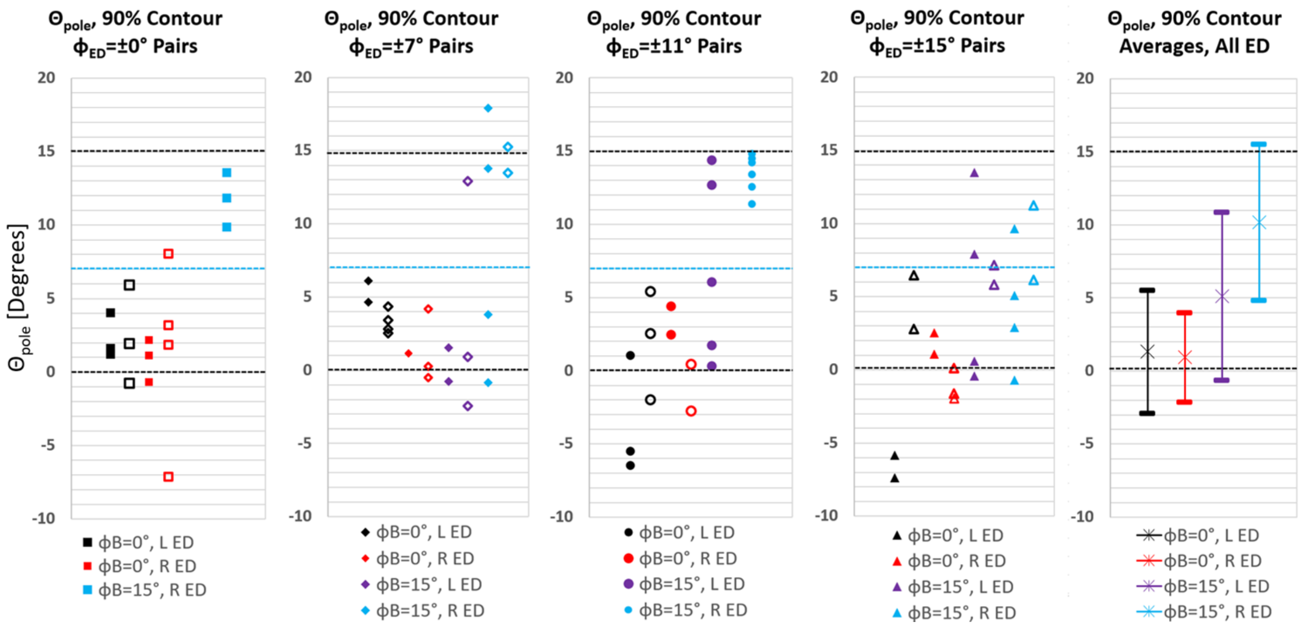

Figure 46. **Pole rotation angle, Θ_{pole}, for 90% contours from 81 ED. Data are plotted within separate panels according to the absolute value of pair angle, ϕ_{ED}, where positive ϕ_{ED} are plotted with filled markers, negative ϕ_{ED} are plotted with hollow markers of the same shape and color. Black, red, purple, and blue data points are associated, respectively, with the following four cases: (ϕ_B=0°||L), (ϕ_B=0°||R), (ϕ_B=15°||L), and (ϕ_B=15°||R), where L and R indicate which ED Θ_{pole} was calculated from. The fifth panel averages data for these four cases, where the center point gives $\Theta_{pole,AVG}$ with 1 standard deviation "error bars" assigned. Note that the x-value of data points has no physical meaning. Data are simply horizontally separated within panels to avoid excessive overlap.**

Several conclusions can be drawn from the data in Fig. 16. First, ϕ_{ED} has no clear impact on Θ_{pole}, which is expected, since bare ED are known to evolve largely in isolation throughout the time of surface plasma formation. Next, despite the spread contained within this limited dataset, ϕ_B does significantly influence Θ_{pole}. As shown in the 5th panel of Fig. 16, $\Theta_{pole,AVG}$ ~1° for ϕ_B=0° for both left and right ED whereas when ϕ_B=15°, $\Theta_{pole,AVG}$ =5° for left ED and $\Theta_{pole,AVG}$ =10° for right ED. To determine whether the observed difference between the means of these datasets is statistically significant, we apply Welch's t-test [lxiii] and separate the data in Fig. 16 into two groups. Group one includes 43 Θ_{pole} datapoints for ϕ_B=0° (black and red datapoints), and the second includes 37 Θ_{pole} datapoints for ϕ_B=15° (purple and blue datapoints). The null hypothesis that the mean polar angles for the two datasets are equal is rejected, as indicated by the hypothesis test result, h=1. The p-value, p=0.0000 indicates very strong evidence against the null hypothesis. Furthermore, the test indicates that the difference in the mean of the ϕ_B=15° and ϕ_B=0° datasets falls within the range from 4.6° to 9.1° degrees with 95% confidence. To further exemplify the impact of ϕ_B, note that only 1 out of 43 ϕ_B=0° ED emissions have Θ_{pole}>7° (Θ_{pole}=7° indicated by blue dashed lines), whereas 21 out of 38 ϕ_B=15° ED emissions have Θ_{pole}>7°. However, it is noteworthy that, $\Theta_{pole,AVG}$ for ϕ_B=0° is nearly 0°, matching prediction, whereas $\Theta_{pole,AVG}$ for ϕ_B=15° is much less than 15° (falling well below the theoretical prediction). Several experimental factors could influence this inconsistency. First, the azimuthally correlated orientation of background machining grooves (see Fig. 15(b)), would likely tend to favorably align pole heating towards the vertical (Θ_{pole} near 0°). Second, it is possible that ϕ_B did not meet the experimental design specification of 15° due to undetected temporally and spatially variable shorting. Finally, incomplete understanding of the governing physics may remain.

The observed difference in Θ_{pole} data for left versus right ED for ϕ_B=15° experiments was unexpected and is not yet understood. That said, one potentially impactful machining asymmetry was uncovered after the experiments and is discussed in Appendix 3 of the publication.

3.2.2. Dielectric coated ED—Pair merging along ϕ_B

Data obtained from *dielectric-coated* ED targets demonstrate both local alignment of overheating patterns from single ED towards ϕ_B and enhanced merging for ED pairs when ϕ_{ED} is aligned with ϕ_B. For example, data from nominally similar targets are shown in Fig. 17. The left-hand column (Figs. 17(a-d)) displays data from experiment M16523 where ϕ_B=0° while the right-hand column (Figs. 17(e-h)) displays data from experiment M16502 where ϕ_B=+15°. Here, we display emissions from the ϕ_{ED}=+15° pairs (Figs. 17(a,e)), the ϕ_{ED}=0° pairs (Figs. 17(b,f)), and the ϕ_{ED}=-15° pairs (Figs. 17(c,g)). It is apparent that the pair heating topography changes with ϕ_B. For example, when considering the ϕ_B=0° data, the ϕ_{ED}=0° pair (Fig. 17(b)) demonstrates well-connected emission about the 0° straight line connecting the ED centers, while emissions between the ϕ_{ED}=+15° and ϕ_{ED}=-15° pairs (Figs. 17(a) and 17(c)) are more segmented. Similarly, when considering the ϕ_B=+15° data, the ϕ_{ED}=+15° pair (Fig. 17(e)) demonstrates well-connected emission about the +15° straight line connecting the ED centers, while emission between the ϕ_{ED}=0° and ϕ_{ED}=-15° pairs (Figs. 17(f) and 17(g)) become progressively more segmented as the misalignment between ϕ_{ED} and ϕ_B grows. Thus, data are consistent with preferred merging about ED pairs which are well aligned to ϕ_B. Next, we quantify these qualitative observations by evaluating (1) how ϕ_B alters local overheating orientation from individual ED, (2) pair merging connectivity as a function of the difference in angle between ϕ_B and ϕ_{ED}, and (3) the evolution of pair merging as a function of target current for various ϕ_B to ϕ_{ED} alignment.

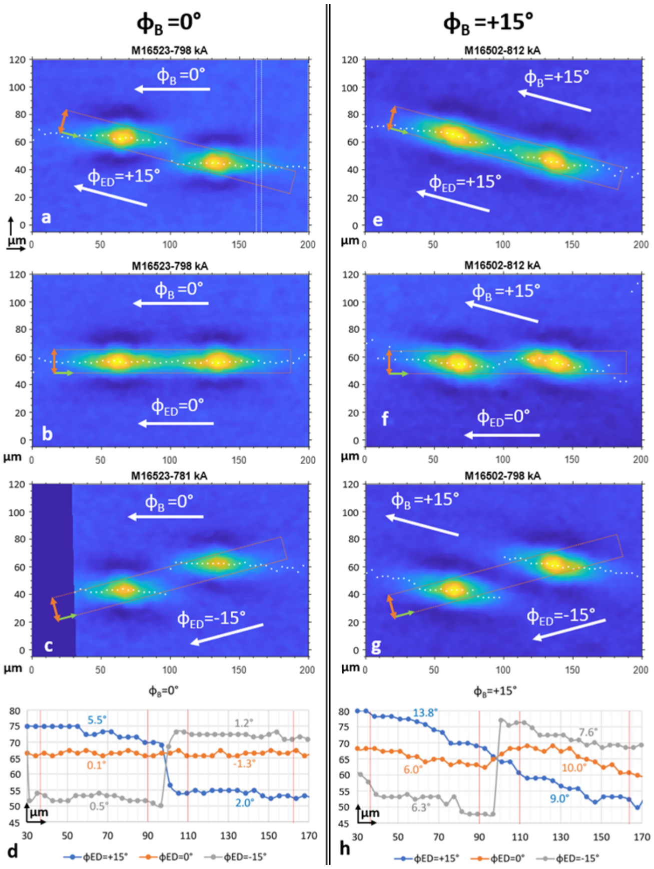

Figure 57. Data on pair merging and local emission rotation for ϕ_{ED}=+15°, 0°, and -15° pairs for the cases of ϕ_B=0° (a-d) and ϕ_B=+15° (e-h). Both ϕ_{ED}=0° and ϕ_{ED}=+15° pairs were on the 0° side of the target, while the ϕ_{ED}=-15° pairs were on the 180° side of the target. Therefore, images were captured with separate ICCDs at different times and the load currents differ minimally. Localized ED emissions from individual ED are ellipse-like, with a major axis that tends to align toward ϕ_B. To quantify these observations, the location of peak emissions from 5-pixel wide vertical profiles (e.g., white rectangle in (a)) were superimposed on the image, generating the series of white circles. These data are replotted in (d) and (h). Angles reported in (d) and (h) correspond to the major axis of each ellipsoid.

The data in Fig. 17 show that ϕ_B alters the local overheating orientation of an individual ED. While pair merging is apparent and thus individual ED do not evolve in full isolation, it is nonetheless true that each ED develops local ellipse-like emission, and the major axis of these ellipse-like emissions tends to align toward ϕ_B. To quantify this effect, vertical profiles were obtained by segmenting each image into 5-pixel-wide, full-height rectangles (see the example white rectangle in Fig. 17(a)). For each profile, the maximum was found, and the z-location of that maximum was plotted over the image, generating the series of white circles shown in Figs 17 (a-c & e-g). Curves generated in this manner are replotted together in Figs. 17(d & h). The data confirm that the most continuous straight-line emissions connecting the ED centers occurs for ϕ_{ED}=ϕ_B (compare the orange curve in Fig. 17(d) and blue curve in Fig. 17(h) to ϕ_{ED}≠ϕ_B curves within each plot). Furthermore, linear fits have been determined for the portions of the curves nearest the center of each ED. Linear fits are derived from the data points within the vertical red lines pairs in plots 17(d) and 17(h), which span about 2X the original rim diameter of the ED and provide an estimate of the angle of the major axis of each ellipsoid. Here, we see that major-axis angles of the ellipsoids associated with ϕ_B=0° are small in comparison to the major-axis angles associated with the ϕ_B=+15°, suggesting favorable orientation of local heating patterns along ϕ_B .

Next, we evaluate pair merging strength for varying ϕ_B to ϕ_{ED} alignment. To do so, emission profiles are calculated along straight lines passing through the center of each ED within a pair (i.e., along an angle ϕ_{ED}). Data contained within the orange rectangles shown in Fig. 17(a-c & e-g) are averaged about the 20-cell "height" (along the orange double arrows) and plotted along the axis indicated by green arrows. Profiles are normalized by setting the peak emission associated with the center of the brightest ED to 1 and the average background emission associated with surface emission far from the ED pair to zero. Fig. 18(a) displays these profiles for experiment M16523 where ϕ_B=0° while Fig. 18(b) displays profiles from experiment M16502 where ϕ_B=+15°.

Emissions between ED pairs, centered at 0 µm on the x-axis, are shown to increase as the difference in angle between ϕ_{ED} and ϕ_B falls, as indicated by the emission profiles in Fig. 18. In Fig 18(b), where ϕ_B=+15°, the emission profile for the ϕ_{ED}=-15° pair (30 degrees different from ϕ_B) falls to the background level (near zero scaled emission), whereas emissions from the ϕ_{ED}=+15° pair (ϕ_{ED}=ϕ_B) is strongest at 40% of the scaled peak value, indicative of stronger pair merging. The trend is largely followed, where better alignment between ϕ_{ED} and ϕ_B results in stronger pair merging. The data in Fig 18(a), where ϕ_B=0°, shows a similar trend, with the strongest pair merging observed for those pairs where ϕ_{ED}=ϕ_B (ϕ_{ED}=±0° in this case), with lowest merging for the most poorly aligned pairs (ϕ_{ED}=±15° pairs in this case). Here, no inter-ED heating profiles fall to the background level, apparently due to the reduced maximum misalignment between ϕ_{ED} and ϕ_B. Trends in pair merging strength are summarized in Fig. 18(c), where profile minima near x=0 (found by fitting a parabola to each curve using data from -20 µm to +20 µm) have been plotted against their respective ϕ_{ED} for all curves in Figs. 18(a,b). For ϕ_B=0°, pair merging strength peaks for ϕ_{ED}=±0° and falls as the difference between ϕ_B and ϕ_{ED} grows. By contrast, for ϕ_B=15° pair merging is weakest at ϕ_{ED}=-15° and increases as ϕ_{ED} grows.

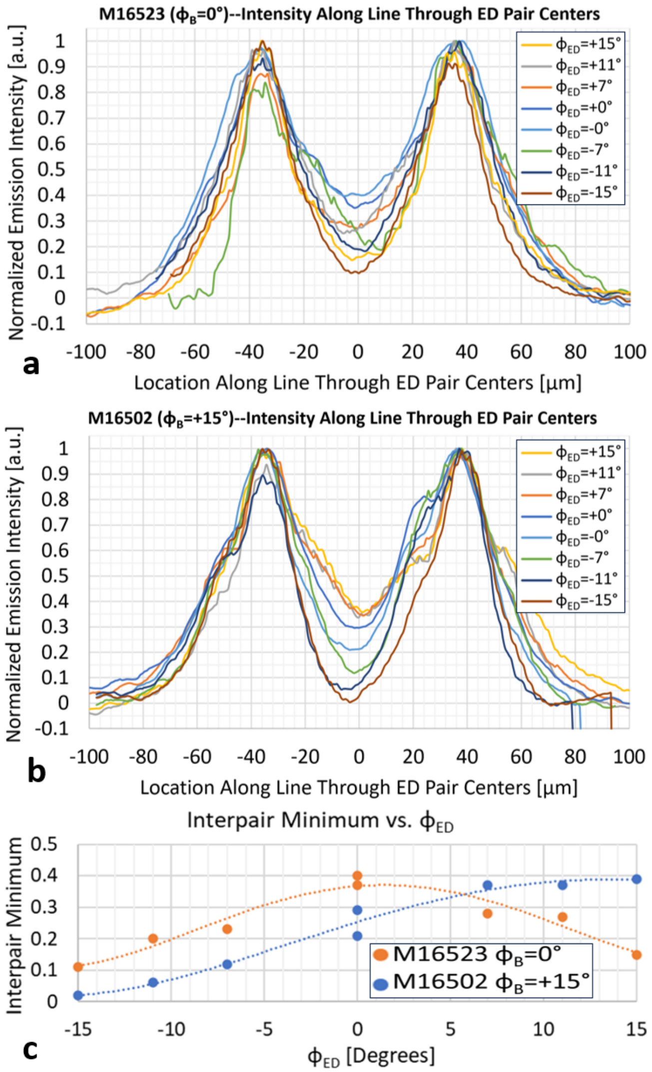

Figure 68. Emission profiles which enable evaluation of pair merging strength for varying ϕ_{ED} to ϕ_B alignment. Profiles are plotted separately for each of the 8 ED pairs from experiments (a) M16523 (ϕ_B=0°) and (b) M16502 (ϕ_B=+15°). For (a), ϕ_B=0°, the ϕ_{ED}=±0° curves have the strongest central emission between the two ED (strongest merging), while the central emission level falls for progressively larger $|\phi_{ED}|$. For (b), ϕ_B=+15°, the ϕ_{ED}=+15° curve shows strongest merging, with weaker merging for smaller values of ϕ_{ED}. Trends in pair merging strength are summarized in (c), where the minima near x=0 have been plotted against their respective ϕ_{ED} for all curves in (a) and (b). Orange and blue trendlines, intended only as guides, are 4th order polynomial fits to each dataset.

Finally, we evaluate how the strength of pair merging changes with increasing current for varying ϕ_{ED} to ϕ_B alignment by comparing data gathered from multiple experiments, at different currents. Profiles are obtained using similar processing as that used to generate Fig. 18. In Fig. 19(a), $\phi_{ED}=\phi_B$=+15° (dashed) and $\phi_{ED}=\phi_B$=0° (solid) profiles are plotted. The degree of pair merging increases with current, reaching a maximum (normalized) value near 0.5. It is noteworthy that the degree of merging appears nearly identical for the two $\phi_{ED}=\phi_B$=0° and $\phi_{ED}=\phi_B$=+15° datasets (compare dashed/solid curves of comparable Mykonos current), suggesting ϕ_{ED} to ϕ_B alignment is the primary driver of the merging rate for closely spaced ED pairs. In Fig. 19(b), ϕ_B=+15°, ϕ_{ED}= 0°, (dashed) and ϕ_B=0°, ϕ_{ED}=+15° (solid) profiles are plotted for the same set of experimental images and currents. The tendency for pair merging to increase at larger current again generally holds, but, given that ϕ_B and ϕ_{ED} are misaligned by 15° in all cases, pair merging is reduced overall versus the data in Fig. 19(a), with the maximum normalized emission between pairs (at highest current) reaching only about 0.3. Trends in pair merging strength versus current for the various ϕ_B and ϕ_{ED} combinations are summarized in Fig. 19(c), where profile minima (found by fitting a parabolas to each curve using data from -20 µm to +-20 µm) have been plotted against their respective Mykonos current for all curves in Figs. 19(a,b). Separate curves are plotted for the 4 combinations of ϕ_B=0°,+15° and ϕ_{ED}=0°,+15°. Profile minima are higher when $\phi_B = \phi_{ED}$ than when these parameters differ by 15° and in all cases merging strength increases with current. These data strongly support that for a randomized distribution of current density perturbations on a dielectric coated conductor, nearby perturbations will favorably merge about ϕ_B, with the degree of merging increasing with current.

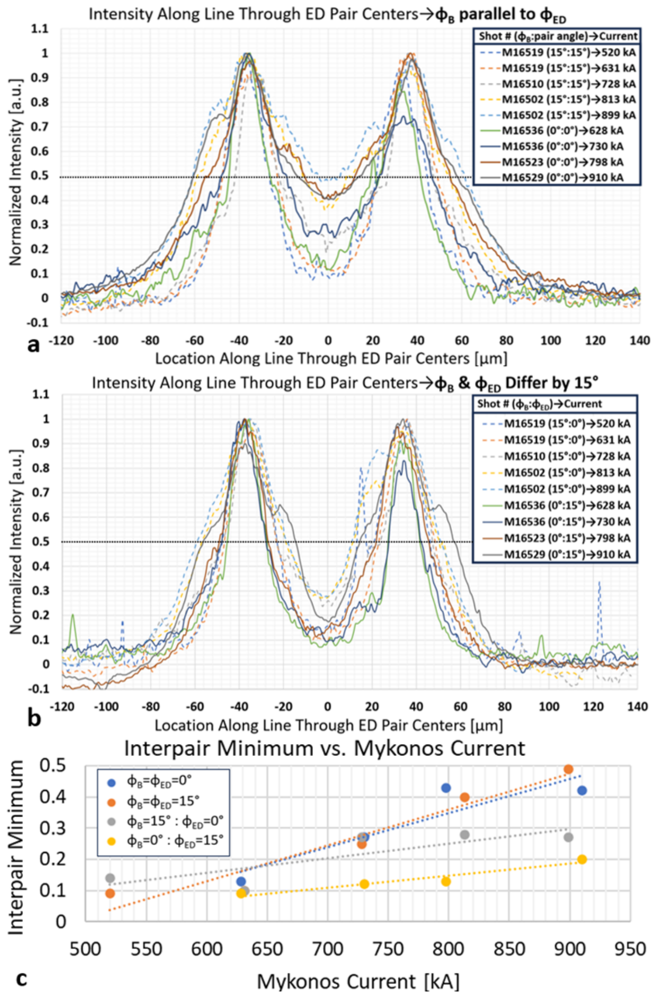

Figure 79. **Pair merging as a function of current for varying ϕ_{ED} to ϕ_B alignment. Data in (a) are profiles for ϕ_{ED} parallel to ϕ_B for both $\phi_{ED}=\phi_B$=0° (solid lines) and $\phi_{ED}=\phi_B$=15° (dashed lines). Data in (b) are profiles where ϕ_{ED} and ϕ_B differ by 15° (see legend). Trends in pair merging strength are summarized in (c), where the inter-pair minima have been plotted against their respective Mykonos current for all curves in (a,b). Color-coded trendlines, intended only as guides, are linear fits to each dataset.**

4. GENERATING 10T STATIC AXIAL FIELD ON MYKONOS FOR ETI RESEARCH

The formation and evolution of ETI has been studied for several years. Recent published work [i] has shown that ETI emission patterns will rotate toward the surface field orientation when dynamic axial magnetic field is applied using a helical return can (HRC, see Section 3), in which the axial and azimuthal field magnitudes are in phase with the accelerator drive current. The dynamics of ETI formation for HRC-driven dynamic axial field (e.g., as in dynamic screw pinch liners) is predicted by MHD simulation to be markedly different from ETI formation for Helmholtz-coil-driven (slow rising) "static" axial field, (e.g. similar to MagLIF liners). To study ETI evolution relevant to MagLIF liners, a pulsed electromagnet system is needed on the Mykonos accelerator to apply a static vacuum field to the ETI barbell target. This section discusses the design of the electromagnets (coils) and the modifications to the vacuum and load hardware to accommodate pulsed coil operation. The design of the capacitor bank and its controller will also be reviewed. The coupled capacitor bank – electromagnet system is named the Applied B on Mykonos (ABM) subsystem for the Mykonos facility. A summary will be provided of the system performance during the April 2025 ETI+ABM Mykonos shot campaign.

Before a concerted design effort could begin, a robust set of design criteria was needed to capture expectations for the delivered system. A requirements document was finalized and approved in February 2024. Each subsection will begin with the relevant requirements that constrained the design for the ABM system.

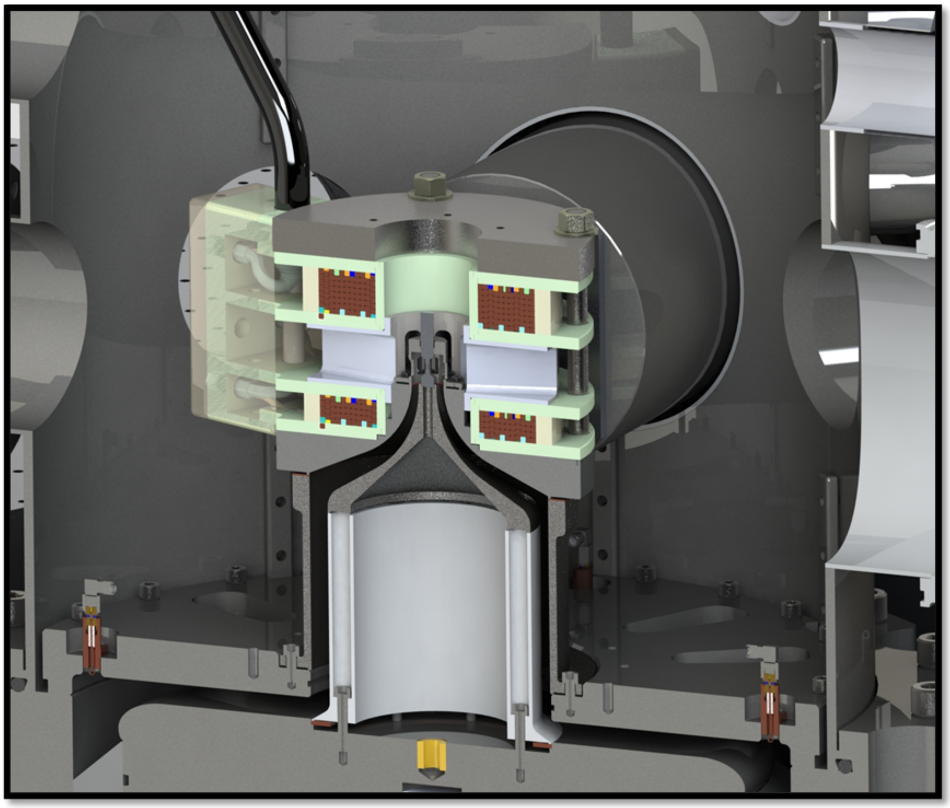

Figure 20: The ABM 10T Coil Pair installed on the Mykonos ETI experimental platform.

4.1. System Performance Requirements and Electromagnet Design

The high-level requirements for ABM system performance were like those of the original Applied B on Z (ABZ) system [xix], which initially delivered 10 T from a split coil design for magnetized liner and MagLIF experiments [xxiv]. In that system, a lower 60-turn coil and upper 80-turn coil approximately one inch apart generated 10 T when driven with about 8 kA. This first ABZ point design was used as the starting point to meet the following ABM system requirements:

- ABM shall achieve 10 T at the ETI rod surface.
- Field shall be >95% uniform over 1 mm axial extent.
- A split coil topology shall be used to allow radial diagnostic access.
- The coils shall be connected in series to prevent drive current imbalance.
- Coils should be spaced apart to not clip the LDM diagnostic's collection cones.
- Coil assembly shall be indexed to ensure line of sight through middle plate support features.
- Coil assembly shall provide 8 lines of sight to the target matching the vacuum chamber ports.
- The lines of sight shall be centered on the target height.
- An encapsulated transition internal to the vacuum chamber shall seal the virtual leaks presented by the coaxial cable conductors.
- The encapsulated transition shall be mechanically robust to survive multiple assembly and disassembly processes during a shot campaign.
- Coil pair should achieve a lifetime exceeding ten shots at 10 T.

The "swooping" MITL (see Section 3), designed for HRC experiments, was designed to also be compatible with ABM coils, and so reserved volume for the bottom field coils as the feed extended axially. The volume requiring magnetization at 10 T near the ETI barbell exceeds 40 cm^3. The axial extent of the ETI target is constrained to be aligned with the midplane of the larger vacuum re-entrant ports for the LDMs. The coils and any reinforcement features are required to clear an acceptance angle cone of approximately 28°, which projects a 2.5" diameter cone about 6" from the ETI barbell face. To fit within this limited volume, the bottom coil's wire layout was switched from 6 axial turns by 10 radial turns (6 x 10, 60 nominal turns) to a more compact 5 x 11 (55 turns). To compensate for this reduction in turns, the upper coil was modified from 8 x 10 (80 turns) to 8 x 11 (88 turns). This redistribution of turns does introduce some nonuniformity to the magnetic field through the load region, but nowhere near enough to change 5% within 1 mm axial height. The original ABZ 60-80 coil pair achieved <1% nonuniformity over the 1 cm tall MagLIF liner. Similar performance to this is expected despite the redistributed turns to 55-88. Figure 81 shows the original ETI layout next to the ABM+ETI configuration.

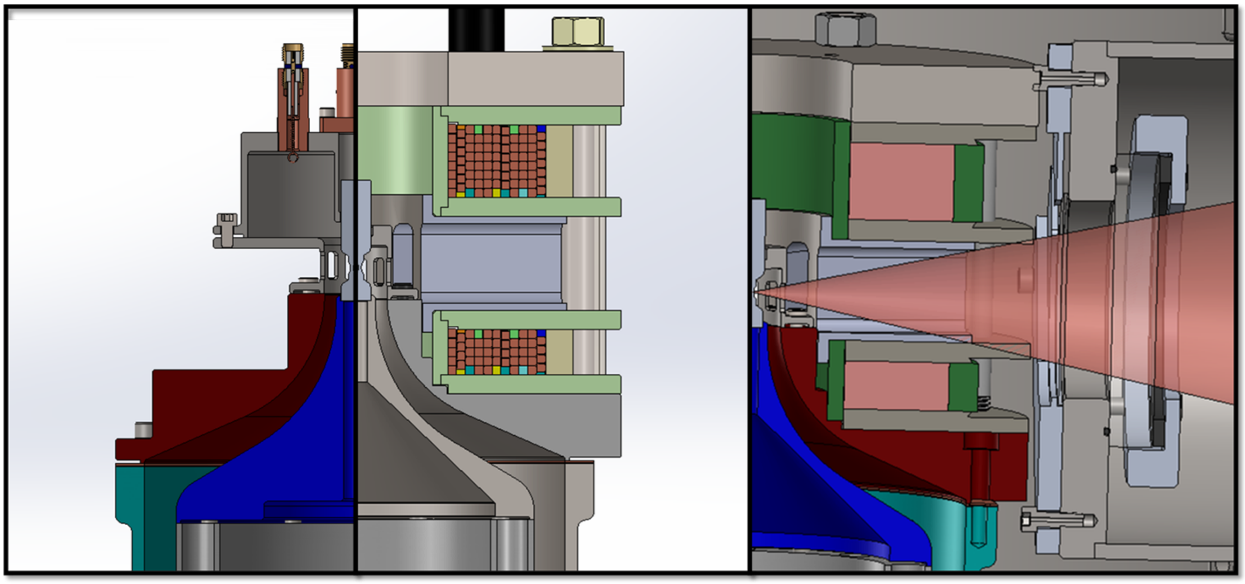

Figure 81: The original ETI platform with extended power feed (left) to permit room for the bottom coil. The ABM+ETI load hardware (center) with coil pair separated by titanium middle plate. The LDM acceptance angle through the coil plate diagnostic window is only slightly clipped (right).

The Mykonos vacuum chamber is much smaller than the Z chamber, so the two-coil system had to be significantly compressed compared to how it is deployed on Z. It is difficult to ensure identical current distribution in a two-coil system with unequal inductances. This is mitigated by connecting the coils electrically in series and ensuring HV standoff for the higher voltage coil. Like ABZ, ABM is using a coaxial cable feed into the vacuum chamber. A vacuum seal is needed on the inner and outer conductors of the cable once they are broken out to connect to the coils. This is done with an encapsulated region that serves several purposes: first, the encapsulant mechanically couples the coaxial cable and provides strain relief; second, the encapsulant seals the virtual leaks presented by the stranded cable conductors; third, the encapsulant provides dielectric standoff for the crimped connections that are required to connect cable conductors to coil leads.

The ABM coil pair has been designed to be a monolithic assembly that mechanically couples the lower coil, upper coil, middle plate, and coaxial cable-to-coil encapsulated “transition region” into one body. This requires the middle plate to be captured between the two coils before the crimps and encapsulation can be done. Four compression rods are required to sandwich the plate between the coils with an initial preload. Once the Stycast 1264 encapsulation is cured, the assembly is mechanically robust. The middle plate provides 8ea. diagnostic lines of sight with an axial channel height of 0.92 in and an azimuthal angle of 26 degrees. The axial spacing between the turns of the two coils is 1.52 in.

Each coil consists of an annular “winding journal” of #11 square copper magnet wire turns with a double wrap, half overlap of Kapton tape for high voltage insulation. This ensures wire-to-wire standoff exceeding 30kV, well above the operating conditions for the ABM capacitor bank. Zylon fiber is wound over the winding journal to form a 1-cm-thick shell. With a tensile strength comparable to steel, this nonconductive reinforcement contains the significant radial self-forces imparted by the coils during an ABM pulse. Each coil is axially contained by flanges machined out of G10 fiberglass composite; lead ingress and egress channels are machined into the flanges to provide containment for coil ingress and egress leads, which guide the two conductors to the transition region. The coil assembly is secured to the Mykonos anode via four 3/8-16 titanium tiedown rods, with titanium nuts torqued to 18 ft-lb, and a stainless-steel top plate. The compressive preload is sufficient to contain the repulsive force that the coil pair experiences during the pulsed magnetic field diffusion into the Mykonos load hardware. The tiedown rods also provide the indexing feature required to ensure the radial lines of sight are aligned with the diagnostic apertures. Figure 22 below labels the coil pair per this discussion.

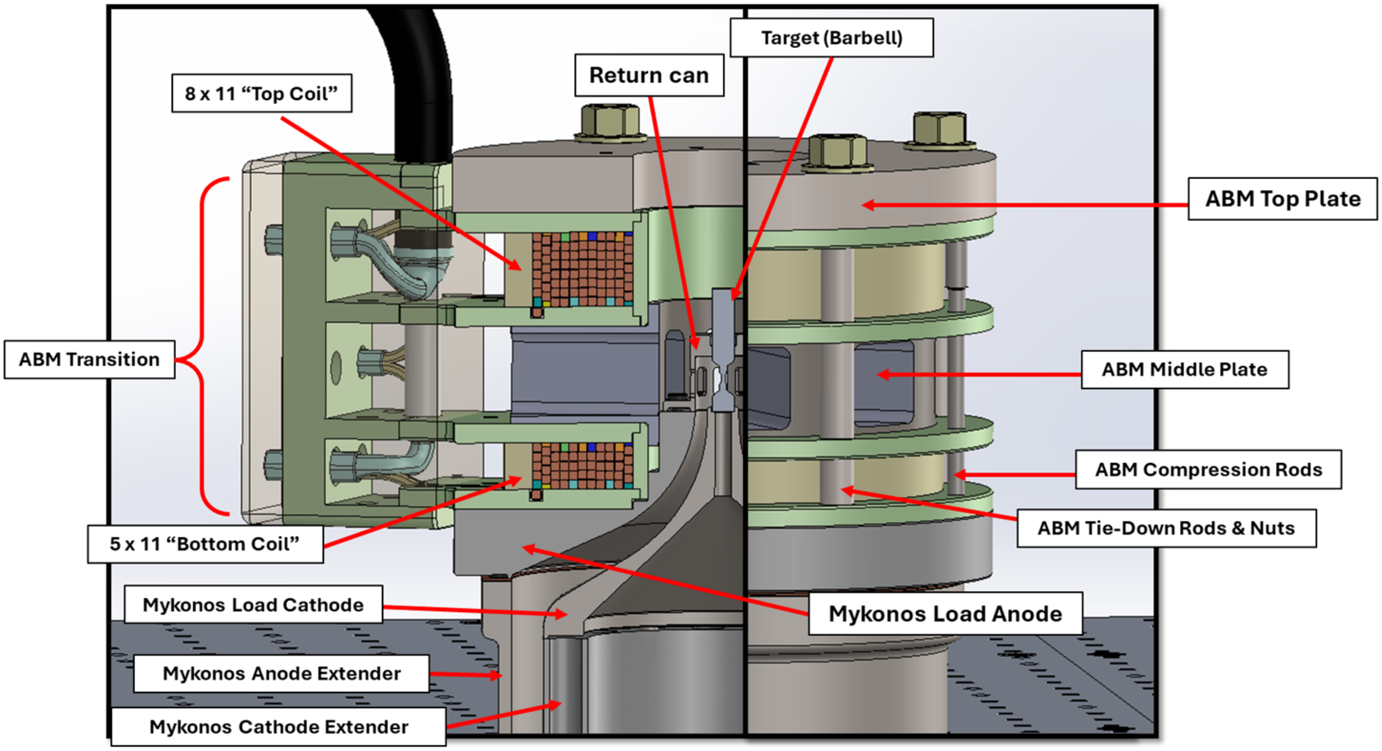

Figure 22: The Applied B on Mykonos electromagnet system in half-section (left) and exterior views (right). Labels are provided of key coil assembly and Mykonos load hardware components.

ABZ coils destined for Z are decidedly single use, as the Z shot destroys the coil pair after target implosion. The ABZ 60-80 coil pairs have been shown to have lifetime of over ten shots at 10 T in light lab characterization and lifetime demonstration research. The self-forces for a coil pair operating at 10 T do not dramatically exceed the inherent strength of the magnet wire, much less the Zylon reinforcement shell. To ensure multi-shot lifetime on the 1 MA Mykonos accelerator, the only addition required was to add reinforcement on the inner diameter to protect the winding journal from the debris environment. A G10 tube was incorporated into the coil bodies to protect them from debris, increase voltage standoff from the grounded experimental hardware, and increase the compressive modulus of the coil system. The reasonable operating field level and this additional mechanical reinforcement has provided excellent reusability for ABM coil pairs. A single coil pair has been used for all commissioning and ETI+ABM shots, reaching 18 shots at the 10 T operating point with no indications of compromised performance. Figure 23 highlights the inner diameter G10 reinforcing tube on each coil.

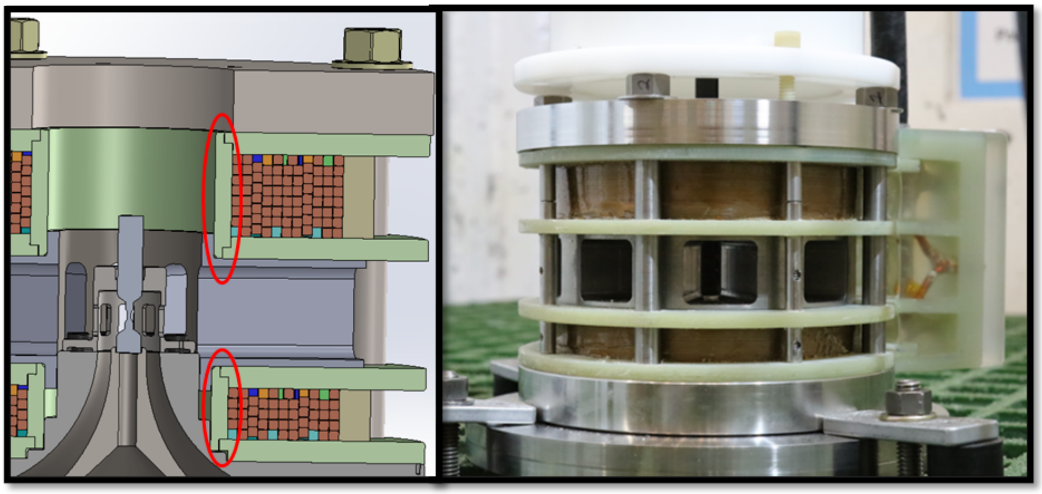

Figure 23: Each coil in the ABM pair has an inner diameter G10 composite tube (left) to protect the coil from debris and increase voltage standoff. ABM-001 (right), the coil pair used for all commissioning and ETI+ABM testing, has accumulated 18 shots at 10 T without issue.

The design space for the coil pair structure was constrained by the geometry of the Mykonos ETI load hardware and the restrictive volume of the vacuum chamber. This is contrary to standard magnet design, where such parameters are driven instead of the required magnetic performance. Because the coil pair and capacitor bank were being designed together, it was easier to just build a big enough bank to achieve the required field level for the resultant geometry. ANSYS Maxwell's [lxiv] transient magnetic field solver was used to determine the required capacitor bank driver to achieve the 10 T requirement at the ETI barbell. This solver tracks magnetic diffusion through conductive materials and can provide the dynamic coil impedance to a coupled circuit model of the capacitor bank. These simulations are linear, in that there is no accounting for changes in resistivity due to ohmic heating of conductors. This is a negligible impact to diffusion through Mykonos load hardware and for coil pairs operating at 10 T, as ohmic heating of bulk Mykonos conductors during diffusion only increases the temperature a few degrees.

The coil cross sections in ANSYS Maxwell can be approximated as sheets in which a uniform current density is applied, which is an appropriate simplification of the same drive current flowing through each of the wires in the winding journal. Each sheet is assigned an effective number of turns that multiply the calculated current distribution:

$$n_{eff} = n_{axial}(n_{radial} - 0.7)$$

The 5x11 and 8x11 have approximately 48.2 and 80.3 turns instead of the nominal 55 and 88 turns. The turns within a coil cannot achieve the perfect fill factor required to achieve nominal values; those on the outside edge of the winding journal require more azimuthal volume as they wind to the next radial layer. The turn decrement per layer is estimated at 0.75 and then fine-tuned by comparing calculated effective coil inductance to that measured from the prototype pairs.

Custom capacitors were deemed too expensive for the scope of this LDRD project, so 830 μF, 11 kV capacitors in organizational storage became the building block for the excitation circuit. The gentle local optimization for energy coupling efficiency to this coil pair was found with two parallel capacitors for 1.66 mF ideal (1.60 mF measured). The resulting magnet system simulation shown in Fig. 24 achieves 10.2 T on the ETI barbell face when the 1.6mF capacitor bank is initially charged to 8.0 kV. Uniformity over the 1mm axial region of the ETI experiment is verified to be over 99% via an axial lineout of barbell surface field.

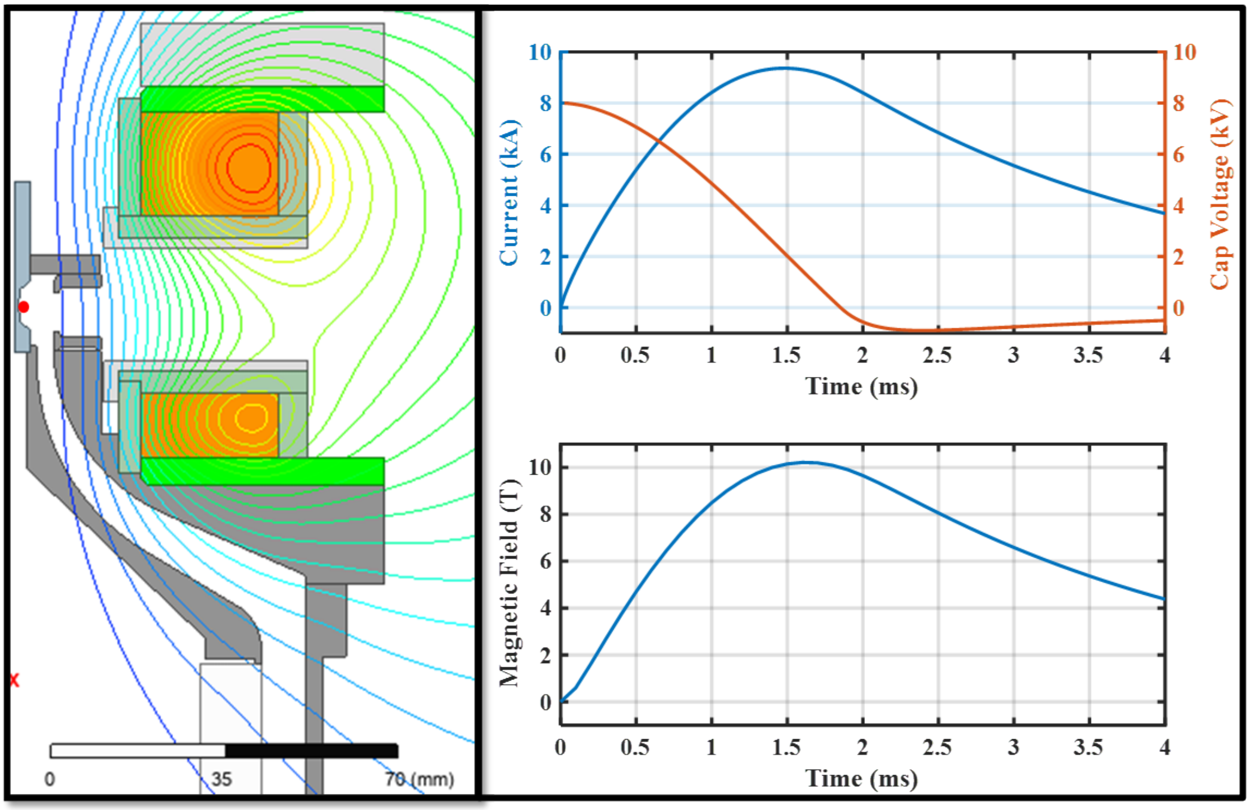

Figure 24: The axisymmetric geometry of the ETI+ABM load hardware in ANSYS Maxwell (left) with flux lines at peak current; the tangent of any flux line represents the direction of the magnetic field vector. An initial bank charge voltage of 8.0 kV delivers 9.36 kA (upper right) and applies 10.2 T (lower right) to the ETI barbell surface at the indicated point (red circle, left).

The designed coil assembly can meet required applied magnetic field magnitude and uniformity requirements. Additional design considerations must be made to ensure the coupled coil – load hardware system can handle the magnetic forces imparted during pulsed field diffusion. These considerations will be discussed in the next subsection.

4.2. Load Hardware and Vacuum Feedthrough

The existing ETI load hardware configuration required only minimal modification to enable integration of a coil pair onto the experimental platform. An already proven extended power feed was critical to a straightforward design effort to achieve required premagnetization. Several unknowns needed to be addressed to ensure Mykonos could operate with a pulsed magnetic field:

- The power flow contours of the anode and cathode base pieces shall not be modified to accommodate the coils.
- Induced force load on cathode assembly shall not exceed vacuum force on the base cathode (~7600 N, per conversation with B. Hutsel and solid model area estimates).
- A vacuum seal shall be performed on the OD of ABM power delivery coaxial cable.

It is a rigorous process to design power flow surface contours that couple machine current from a larger radius to an axially-extended smaller radius. Inclusion of the coil system was therefore not permitted to modify these power flow contours. This objective was easily met, though, as only substantive changes were made to the outside region of the ETI anode plate. Counterbore features for enforce coil assembly concentricity were added, as were threaded hole patterns for the tiedown rods. A significant amount of material from the bottom of the cathode was removed to reduce the induced forces on the cathode. These changes can be inspected in Fig. 21.

Early in the project, there was significant concern that an axially applied downforce on the cathode during magnetic field diffusion could overcome the vacuum forces sealing the Mykonos water resistor and introduce a water leak into the chamber. A rexolite insulator isolates the vacuum section from the upstream transmission line and series load resistor. The machine cathode ("cathode button") sits centered within this insulator with an o-ring seal to prevent water leakage into the chamber. A Torlon tensioning rod secures the cathode button in place, which then gets put in tension when the chamber is pumped out. With a surface area of 121 in^2, the pressure differential applies a tension load of 7630 N (7.6 kN). This layout is shown graphically in the following figure.

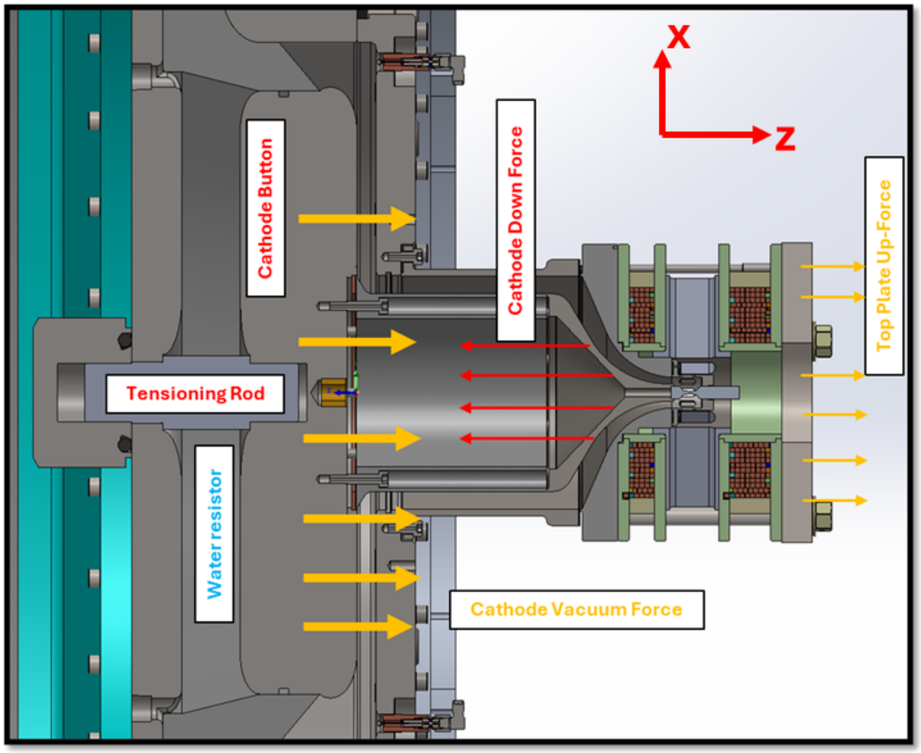

Figure 25: Induced forces on the cathode from magnetic diffusion oppose the vacuum pressure load on the cathode button. The coil pair and top plate repel from both anode and cathode. Down- and Up-force are defined in relation to the z axis, which is horizontal on Mykonos.

Hollowing out the cathode proved to be necessary to reduce total induced forces. Total force per conductive element is calculated by integrating the z-directed component of $J \times B$ for the entire axisymmetric surface, converting a force density (N/m^3) into cumulative force. The induced downward force for the modified cathode pieces is 5.2 kN at 1.1 ms, about 70% of the vacuum pressure load. Total anode downforce is 47.5 kN at 0.9 ms, but that reacts through the base plate for the load chamber which is much more mechanically rigid than the cathode interface. Finally, the coil pair and top plate as a body lift with a peak force of 52.6 kN at 0.9 ms. Peak force does not occur simultaneously for all components in the system. The time varying forces are shown in Fig. 26.

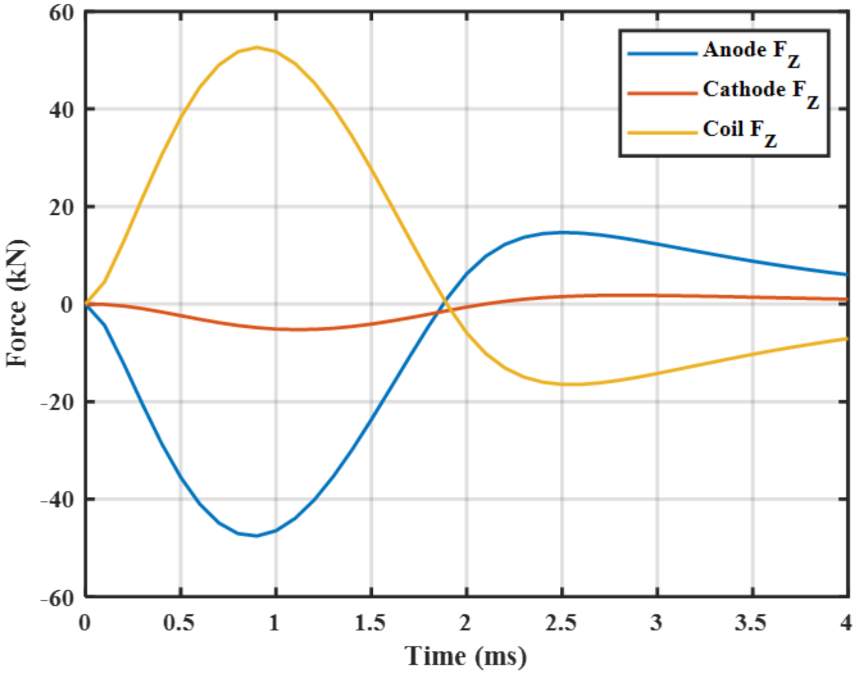

Figure 26: Induced forces in anode (blue) and cathode (red) conductors. The total force for the coil pair, middle plate, and top plate are summed into the yellow curve.

The four titanium tiedown rods must react the ~52.6 kN lift force for the coil pair. With a minor diameter of 7.5 mm and a bearing area of 44.7 mm^2, the four rods experience a tensile stress of 294 MPa, well below the yield strength of Ti6Al4V of ~880 MPa. The tiedown rods have about 17 mm bearing depth engagement into the anode. The pullout stress in shear for the four rods is about 25.6 MPa, again well below the shear yield stress for AISI 304L stainless steel of ~386M Pa. A torque value of ~18 ft-lb is used to compressively preload the ABM structure and fully react this repulsive force. This exact torque value is not critical, as allowing the rods to be partially loaded in tension will not elongate enough to compromise diagnostic access.

During the February 2025 commissioning series, the first downline attempt with ABM and an ETI barbell failed. The Mykonos electrical traces left no doubt that the electrical connection had been opened; the post-shot inspection showed the barbell hanging loosely in the return can structure with significant electron beam damage and arcing to the internal volume. It is thought that the lower energy pulses prior to downline were sufficient to dislodge the barbell despite the much lower induced forces. Knowing that Mykonos would fire at 1.6 ms, and looking at the force profile in Fig. 27, it is hard to imagine that force loading coupling to positive axial movement of the barbell. However, after 2 ms, the force profile reverses as the field diffuses out of the assembly. It is likely that the low energy shots prior to downline popped the barbell out. A retaining cup was designed and implemented for the ETI+ABM experimental campaign, and no repeats of this failure occurred.

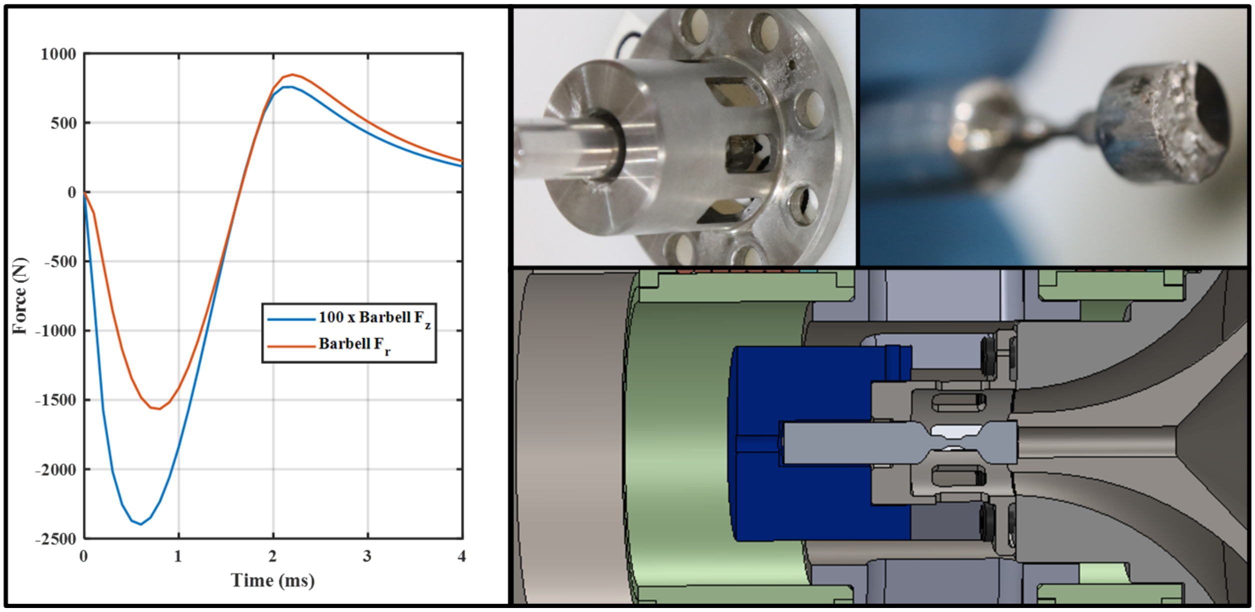

Figure 27: (Left) the radial (red) and 100 times axial (blue) induced forces for a 10-T shot. The barbell and return can system following the failure (upper right); and the barbell retaining cup CAD geometry (in blue) to contain the barbell during pre-downline pulses (lower right).

Feeding a full coaxial cable through the vacuum chamber wall introduces several leak paths that must be mitigated. First, the center and outer conductors provide a virtual leak path to the airside if not properly sealed. Both conductor leak paths are sealed by the encapsulated coaxial-cable-to-coil transition described earlier. The remaining leak path is on the outer diameter ("outer jacket") of the cable as it feeds through the air-vacuum interface. The outer jacket O-ring seal concept on the ABZ system was transferred to a modified 250mm flange blank off. A welded flange adapter was needed to couple this modified feedthrough onto the main Mykonos 400mm vacuum chamber lid.

The vacuum feedthrough assembly process is complex and requires appropriate staging of the vacuum lids, centering/sealing rings, and the coil assembly. The following procedure is used to build the outer jacket vacuum seal in place.

1. Prior to coil installation, the J20138 compression ring, O-ring, QF250 blank off, QF250 centering ring, and QF250-QF400 vacuum lid adapter must be slid in place along the coaxial cable line. Everything but the QF250 centering ring and QF250-QF400 lid adapter must be put in place before the coaxial cable is crimped with its termination to adapt to the load junction box.
2. Stage this hardware on a cart in a manner that does not bend, pinch, or scratch the outer polyethylene of the coaxial cable, O-ring, or centering ring.
3. Feed the ABM coil assembly through the QF250-QF400 lid adapter and QF400 centering ring. Install the ABM coil assembly and secure in place, using a star pattern to get the nuts finger tight, then torqued to 9 ft-lb, then 18 ft-lb.
4. Run the lid adapter and QF400 centering ring up the coaxial cable and secure in place with 4ea. ISO clamps.

5. Snake the QF250 vacuum feedthrough plate and QF250 centering ring up to the chamber and secure in place with 4ea. ISO clamps.
6. Liberally apply IPA or ethanol to a wipe cloth and lubricate the cable ahead of the O-ring. Slide the O-ring and the J20138 compression ring up the length of the cable and secure in place with ¼-20 screws.
7. Build up the 013915A strain relief assembly to protect the cable egress and ensure fidelity of the vacuum seal.

The following figure shows the CAD model half section of this geometry and incremental progress through the previous procedure.

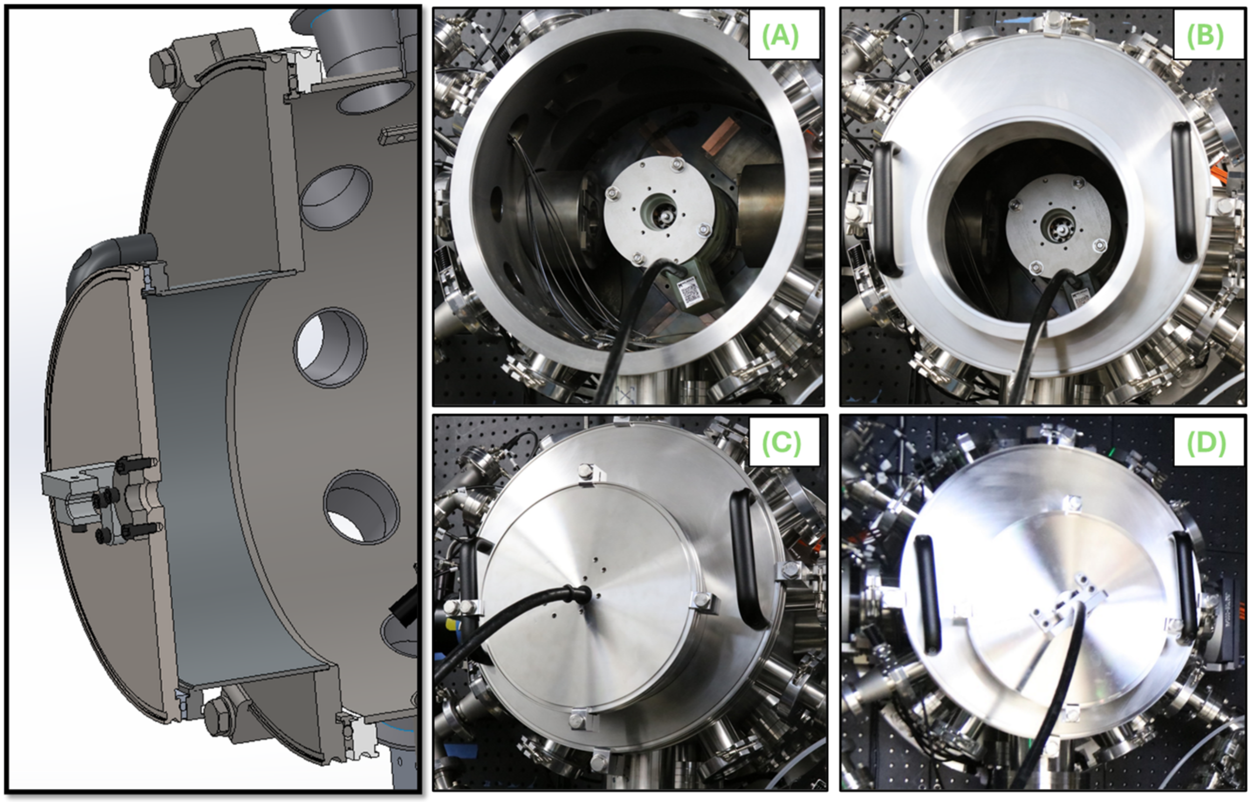

Figure 28:The ABM vacuum feedthrough in CAD (left) without coaxial cable rendered. In (A), the ABM coil has been installed and compressed into place. In (B) the QF250-QF400 adapter is in place. The QF250 feedthrough and o-ring are positioned in (C), and the full vacuum seal is in (D).

4.3. Capacitor Bank and Power Delivery

The required pulsed power circuit to drive the ABM coil pair to 10 T was introduced in a previous section. Capacitors in storage were to be the building blocks of the pulse driver; namely, 2ea. 830 μF, 11 kV rated Maxwell units. Cap charging is provided by a positive polarity, TDK-Lambda 202A-20kV capacitor charging supply rated at 2 kJ/s that runs off 220 V_{AC}. The main user-triggered switch is a Richardson Electronics NL-1057 ignitron unit designed for capacitor discharge and rated for 25 kV and 300 kA. A crowbar diode and resistor are included to passively mitigate voltage reversal on the capacitor bank. The chosen 125 $m\Omega$ resistor keeps the reversal voltage to below 1 kV for an 8 kV shot as seen in Fig. 24 earlier, meeting the 15% recommended maximum voltage reversal. A Strategic Technologies ignitron trigger module was taken from storage and incorporated into the bank chassis to trigger the NL-1057 main switch. This module and the control interface are enclosed in a shielded chassis to reduce EMI effects from the ignitron switch when it is triggered. A normally closed dump relay provides an energy-rated load for dumping the full charge of the banks. This relay is on the upper shelf of the bank enclosure and is visible through the Lexan cover plate. The capacitor bank interlock circuit also will cause the dump relay to close to ensure energy is discharged if the enclosure is opened. This design meets the primary functional requirements for operational safety:

- The bank shall utilize a normally closed dump relay with energy-rated resistor. This state of this relay shall be visible without having to open the enclosure.
- Bank shall incorporate a passive crowbar circuit to reduce voltage reversal to less than 15% of capacitor rating.
- Enclosure should shield internal electronics and trigger circuitry from EMI from ignitron.

The physical layout and enclosure met several requirements. First, the capacitor bank had to be on lockable casters for easy movement between the commissioning facility and Mykonos. It was deemed unnecessary to require movement via overhead crane. Though it does not require non-NRTL inspection for Sandia's electrical inspection procedures, the system was required to have every exposed conductor grounded and designed in such a way to contain any electrical or capacitor failures. An access door above the capacitor terminals is provided to allow access with soft- and hard-grounding sticks for zero energy verification. This step is critical when access to the internal bank circuitry is required for maintenance or troubleshooting. Power cord connections at the rear of the chassis for 120 V and 220 V power connections allow for LOTO to be applied when safing the system. The capacitor bank frame is provided with a grounding lug for secure connection to facility ground when in service.

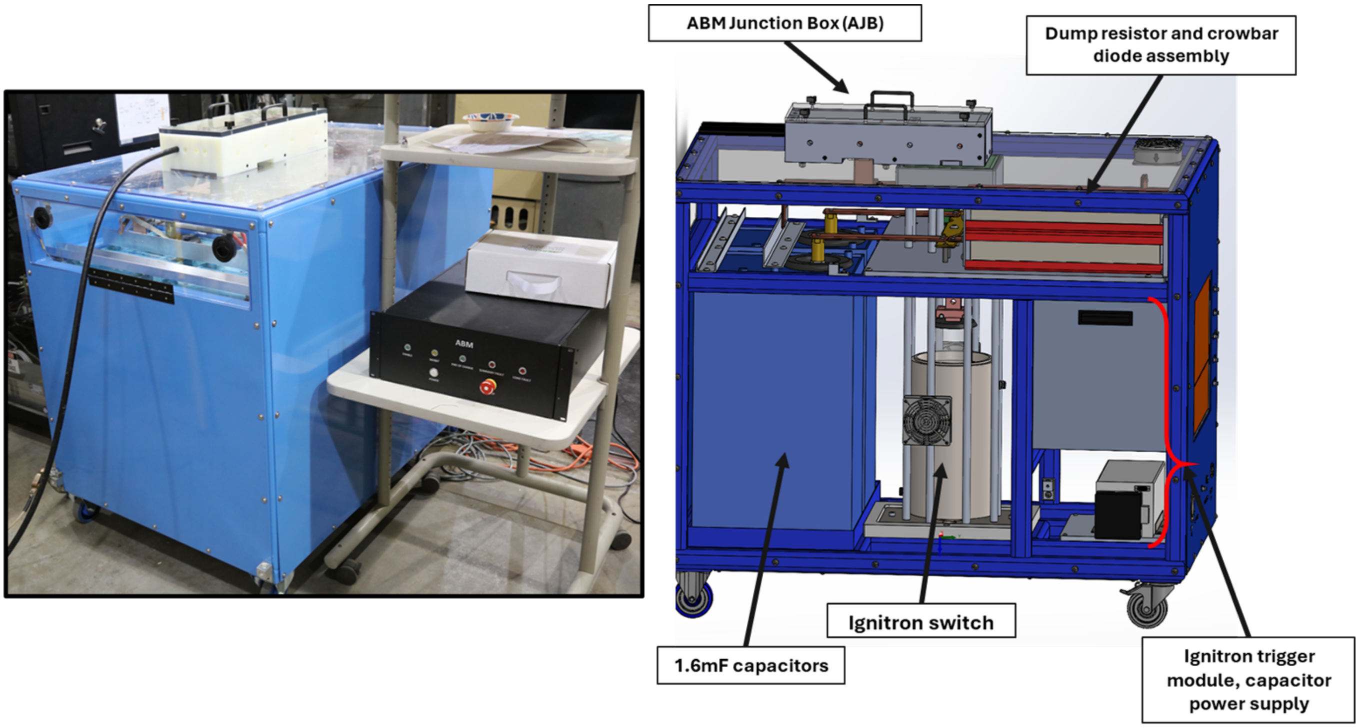

Figure 29: The ABM capacitor bank and control chassis during commissioning activities (left). The access panel for shorting out capacitors is visible on the front face of the chassis. In (right), the main components of the capacitor bank internal volume are shown.

The capacitor bank is positioned about 50 ft from the Mykonos load chamber in the Laser Control Room. A series of coaxial cables and adapter enclosures are required to connect the coil assembly and its single cable lead. A junction box was modified from the ABZ system to adapt directly from the HV bus conductors to output cables. The ABM Junction Box (AJB) is seen on top of the bank in Fig. 29, and for Mykonos outputs two Dielectric Sciences #2323 (DS2323) coaxial cables to run to the Load Junction Box (LJB). Two DS2323 cables were used to reduce the equivalent series resistance of a single cable run. DS2323 has the lowest equivalent series resistance among common HV coaxial cables of about 0.8 $m\Omega/ft$. That said, any reduction in transmission resistance reduces circuit damping and increases achievable peak field, so two are used in parallel for the permanent cable route between AJB and LJB. Cable series inductance is negligible compared to the coil pair.

The LJB provides a modular connection point for the ABM coil load. It is in the lower left corner of the Mykonos laser room and provides a permanent connection point for ABM coils as they are installed between shots and between campaigns. Each ABM coil was delivered from Milhous Company with a 30 ft cable length, since the load end was encapsulated into the coil assembly. Removing the vacuum flange components requires cutting and re-terminating the upstream end, so it was decided to order extra cable in case multiple cuts had to be made during a coil's lifetime.

The excitation circuit used to design the magnets in the previous section used the simplified circuit shown in Fig. 30. Instead of a closing switch, an initial voltage condition on the capacitors is used to excite the simulation. The capacitor pair is modeled as 1.6 mF because measurements of the faceplate 830 μF capacitors revealed that they were closer to 800 μF. Impedance measurements of the output cables and the coil pair were used to create series-RL equivalences. The equivalent inductance of the two coils is resolved in the simulation space, with all mutual coupling and eddy current effects introducing a dynamic impedance load on the coil system. The coil R is lumped into the cable resistance for the ABM load.

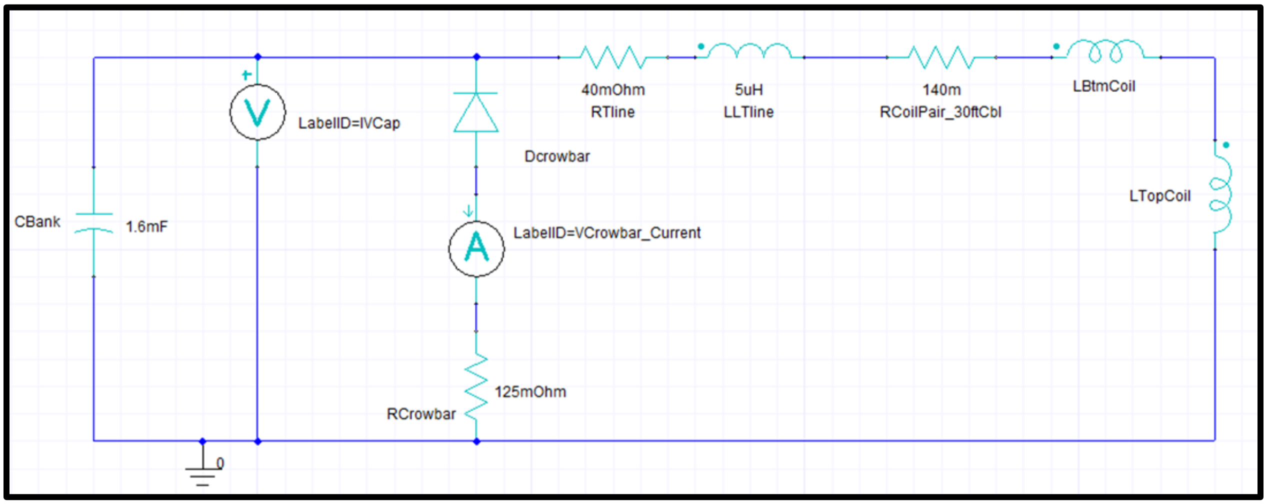

Figure 30: The ANSYS Maxwell equivalent circuit for the capacitor bank, transmission lines, and the inductors for the coil pair.

The detailed capacitor system is shown in Figure 31. This is the as-built schematic for all logic, control, and interlock relays, interfaces with the control chassis and power supply, and the full HV and pulsed circuit. It is part of the ABM system documentation package available upon request from the authors of this document.

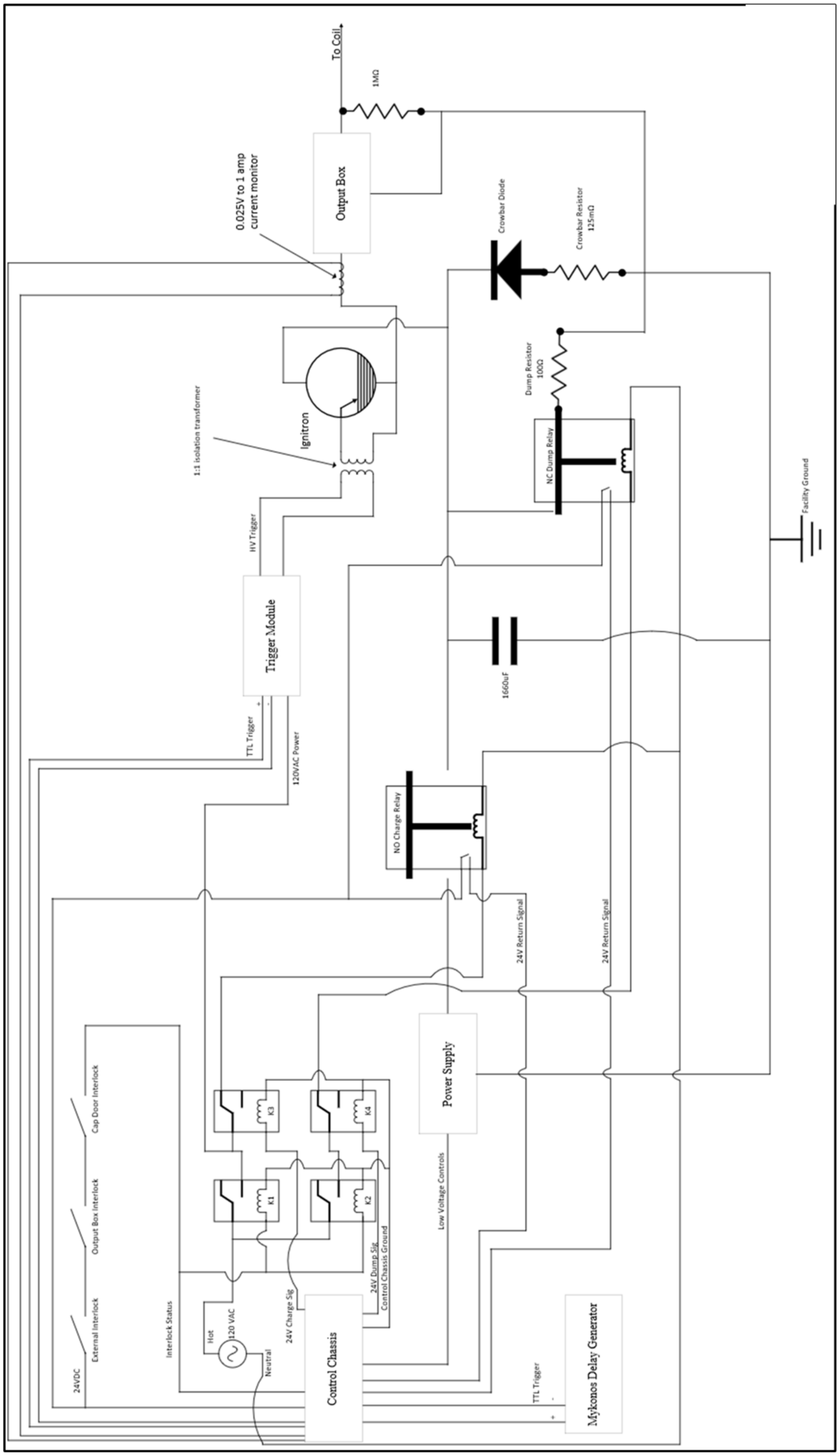

Figure 31: Detailed schematic showing control relays, interlock circuits, and discharge paths.

4.4. System Controller Design

The Control Chassis in Fig. 31 contains the control element that operates the ABM capacitor bank and records signals of interest. An NI 9189 CDAQ control chassis provides remote analog and digital I/O for controlling relay operation, charge voltage setpoints and charge commands, and dump relay control. This CDAQ chassis provides several “slow time” scope channels to digitize the current, voltage, and magnetic fields on the Mykonos millisecond pulse time base. The disparity in time scales between Mykonos and ABM prevented recording relevant signals with the Mykonos facility’s data acquisition system.

A host Windows control computer communicates with the ABM Control Chassis via a fiber optic ethernet adapter. This was done to minimize EMI pickup during ABM and Mykonos charging and firing activities. A NI LabVIEW control program manages shot operations flow, including recordkeeping setup, bank charging and initializing for a Mykonos downline event. The software can also generate a software trigger to operate in troubleshooting mode or in the light lab facility.

The following is a list of functionality requirements that the deployed system controller has met:

- The User-bank interface shall be maintained via embedded NI CompactDAQ controller (“Controller”).
- System shall be controlled via a LabVIEW VI interface using a client model that can be installed on any computer with LabVIEW or LabVIEW RunTime (“Client Computers”).
- Controller shall acquire and buffer all ABM-specific electrical diagnostic signals prior to download to Client Computer.
- System shall have the option to save acquired data from voltage and current diagnostics.
- All file(s) are clearly identified by a unique naming structure including shot number with date and time in the file name (e.g., not just “shot001.dat”)
- Shot specific data includes metadata that identifies:
  - Time of trigger delay (with respect to Mykonos downline)
  - Requested charge voltage (setpoint)
  - Voltage at downline (reading)
  - Date of shot
  - Time of shot (24-hour)
  - Experimenter-specific text string (e.g. “Awe ETI shot 7 of 10 don’t fail this time”)
- For each recorded shot, the acquisition system shall have the channel depth to record at least the following: Main current, main Rogowski, crowbar current, pulse voltage trigger line, main Rogowski, crowbar current, trigger form Mykonos, any ABM-time base load b-dots.
- Conversion from electrical to optical for control communication shall be made within a shielded control volume.
- Controller shall provide interlock capability that disables power supply, disconnects output to capacitor bank, and dumps capacitor charge when any of the following are met:
  - Operator presses soft “EMO” button on Client Computer.
  - Operator/safety watch presses hardware EMO button (outside Mykonos control room.
  - Access panels on capacitor bank enclosure are opened while system is activated.

- Controller shall be user selectable to enable either software trigger (Client Computer) or remote triggering from a Mykonos timing event. External trigger signal shall be a rising edge voltage (Active high), e.g. TTL

The metadata collected during a Mykonos shot looks as follows, in Fig. 32. Figure 33 shows the user interface for initializing a shot, executing an ABM charge and fire, and system readiness monitoring.

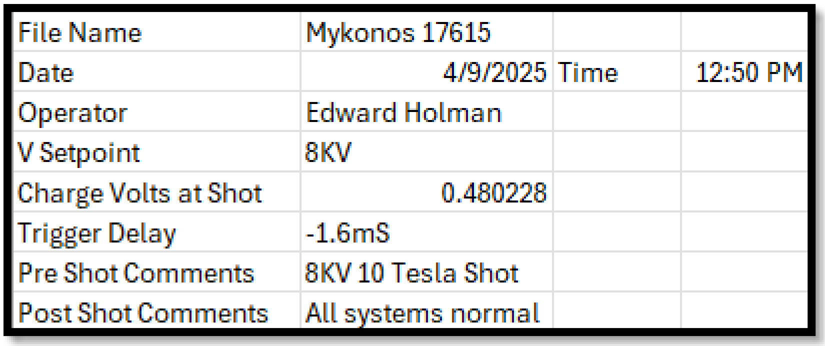

File Name	Mykonos 17615		
Date	4/9/2025	Time	12:50 PM
Operator	Edward Holman		
V Setpoint	8KV		
Charge Volts at Shot	0.480228		
Trigger Delay	-1.6mS		
Pre Shot Comments	8KV 10 Tesla Shot		
Post Shot Comments	All systems normal		

Figure 32: Autogenerated header information for the ABM controller for easy metadata formation during import into a data analysis tool; the balance of the file is channel name, attenuation values used, and columnar tab delimited shot-time data.

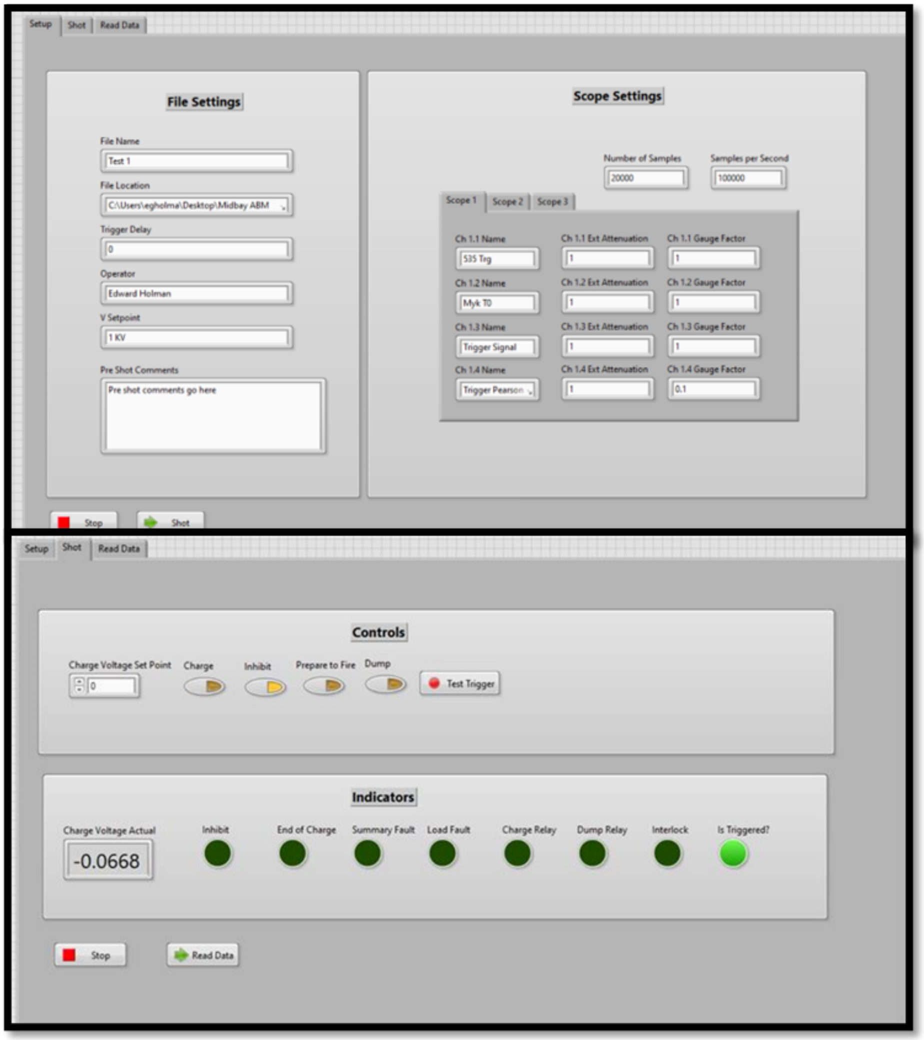

File Name: Test 1
File Location: C:\Users\egholma\Desktop\Midbay ABM
Trigger Delay: 0
Operator: Edward Holman
V Setpoint: 1 KV
Pre Shot Comments: Pre shot comments go here

Number of Samples: 20000
Samples per Second: 100000

Ch 1.1 Name	Ch 1.1 Ext Attenuation	Ch 1.1 Gauge Factor
535 Trg	1	1

Ch 1.2 Name	Ch 1.2 Ext Attenuation	Ch 1.2 Gauge Factor
Myk T0	1	1

Ch 1.3 Name	Ch 1.3 Ext Attenuation	Ch 1.3 Gauge Factor
Trigger Signal	1	1

Ch 1.4 Name	Ch 1.4 Ext Attenuation	Ch 1.4 Gauge Factor
Trigger Pearson	1	0.1

Charge Voltage Set Point: 0
Charge Voltage Actual: -0.0668

Figure 33: The LabVIEW VI for controlling the ABM system from the Mykonos control station.

4.5. Mykonos Commissioning, Performance during ABM+ETI Campaign

In February 2025, the full ABM pulsed power system was assembled in a light lab environment to demonstrate system behavior before deploying to Mykonos. Before being assembled into the capacitor bank, the capacitors were charged to 10 kV and held for 2 minutes three times. The capacitor bank system and first coil pair were fired at the 10 T operating point twice in the light lab configuration. The ABM coil load was assembled onto a Mykonos anode inside of a coil testbed, compressed with the top plate and tie down rods. This provides roughly the correct magnetic circuit, though the Mykonos cathode, barbell, and return can were not present. After these tests passed, the system was moved to the Mykonos facility in Building 983.

Figure 34 shows the layout of the system within Mykonos. The ABM bank was positioned between the support gussets of the overhead walkway running the southern edge of the accelerator. The outward facing apertures of this walkway were covered with Lexan sheets to provide primary containment of debris, should an ABM bank failure occur. The area north of the bank is evacuated during Mykonos charging and firing operations, so no debris shields were deployed there. The 2ea. cables from the AJB run under along the southern edge of the facility before entering through an aperture in the laser control room wall. The LJB is placed in the far-left corner of the laser room to minimize tripping hazards during coil activities. A cart is required to roll the staged coil and vacuum feedthrough hardware into and out of the room on shot days.

The ABM operator interfaces with the ABM controller from the user station in the Mykonos control room. There, they can coordinate the downline sequence with the Mykonos operator for tandem ABM and Mykonos charging and firing. Following a downline Mykonos shot, the ABM operator enters the exclusion area behind the bank and uses shorting sticks to verify zero energy and locking out the subsystem before finishing work. Figure 35 shows the critical hardware pieces as they are deployed to the Mykonos facility.

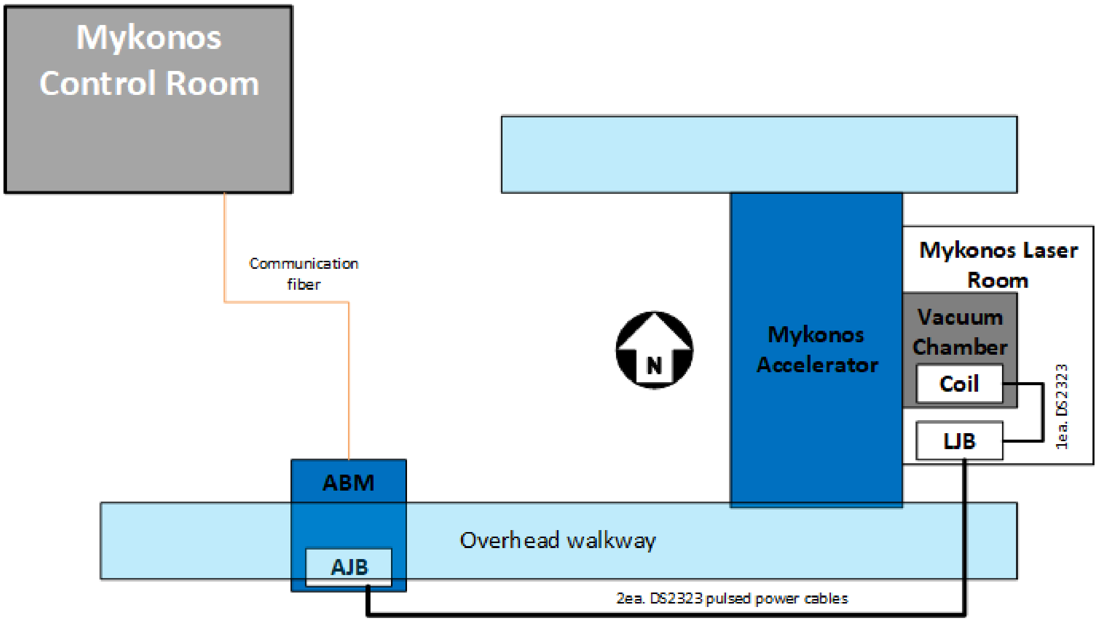

Figure 34: The ABM system layout in the Mykonos lab space.

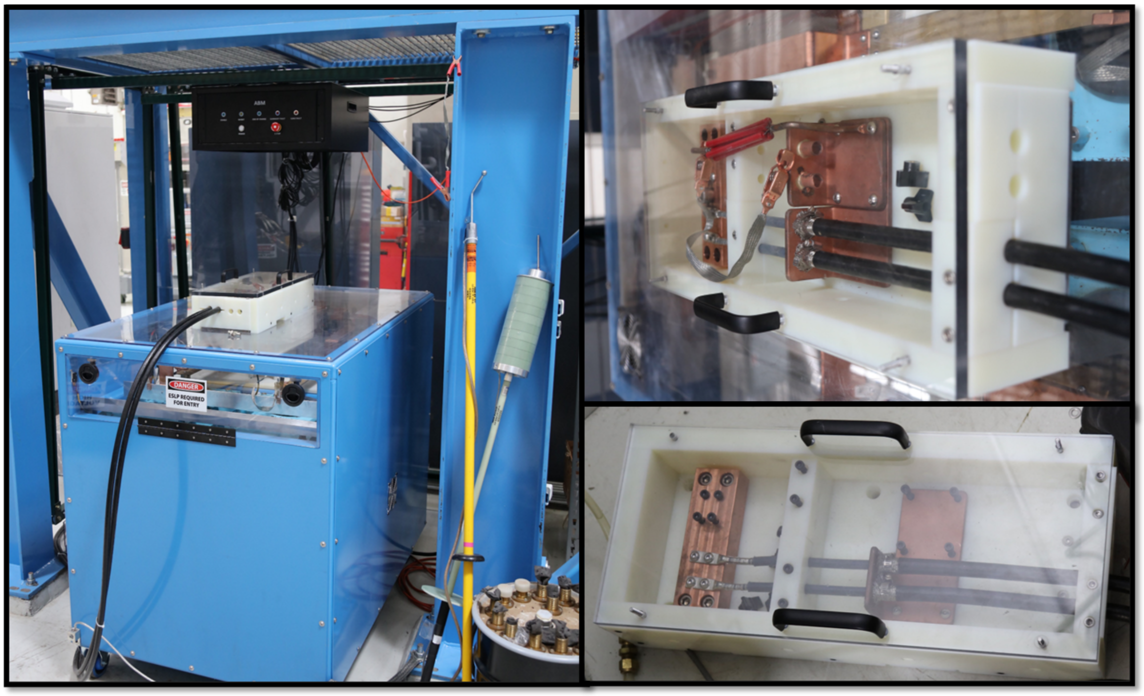

Figure 35: The ABM system deployed to Mykonos, with debris shielding and hard- and soft-grounding sticks (left). The ABM Junction Box for the two output cables (upper right) mounted atop the ABM bank. The Load Junction Box (lower right) in the Laser control room is shown with two input cables from the AJB, but without a connected coil load cable assembly.

Twelve shots in total were performed at the 8 kV charge voltage for nominal 10 T shot performance during the ABM+ETI campaign. The current and therefore the applied magnetic flux density were reproducible to within 1% for these shots. Figure 36 shows an overlay of the 12 shots by Mykonos shot number. The figure also an overlay of all current pulses normalized to the timing fiducial provided by Mykonos; the entire Mykonos shot event happens during the rising edge of the blue pulse at 1.6 ms.

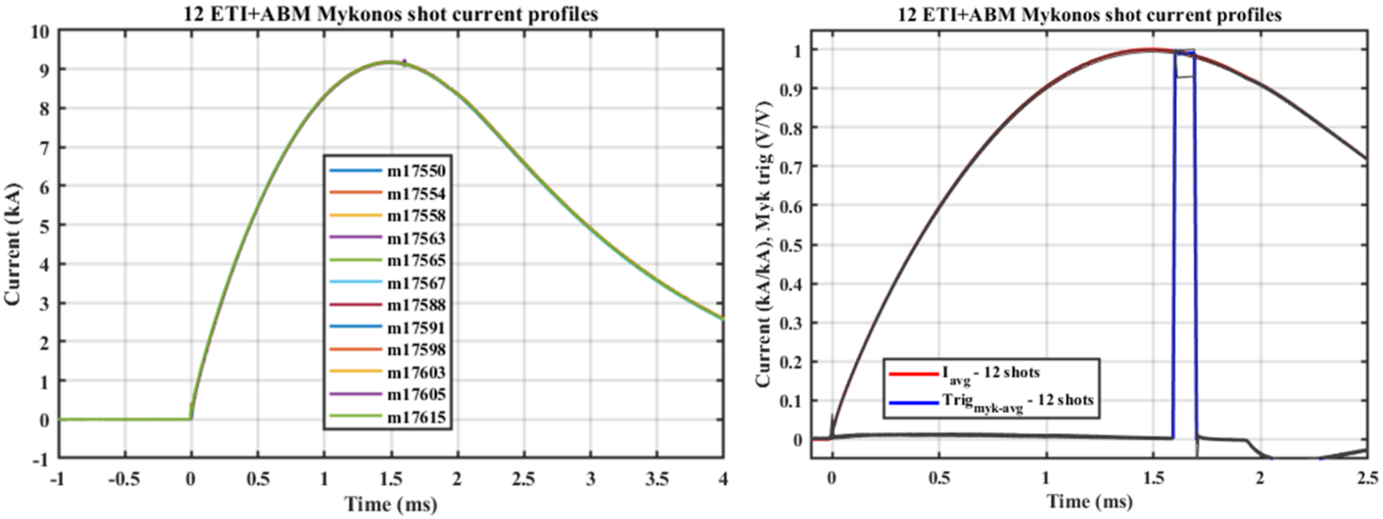

Figure 36: Repeatability of ABM current (kA, left), Mykonos triggering during ABM pulse (right).

The field at the ETI barbell surface can be estimated with reasonable precision by using a scaling factor derived from the Maxwell simulations. For the simulation space described earlier, a 9.22 kA current pulse peaking at 1.5 ms generates a peak field at the ETI surface of 10.06 T at 1.6 ms. This yields a scaling factor of 1.091 T/kA. The average value for the twelve shots in the above figure is 9.18 kA. With scaling applied, all ETI+ABM experiments achieved 10.0 T when Mykonos fired.

The first ABM coil pair (ABM-001) was used for every ABM test pulse during commissioning and experimental campaign work. In total, ABM-001 delivered 18 current pulses delivering 10 T. An interesting development during this campaign was the evolution of the coil pair inductance during the test series. It was not possible to independently measure each coil's impedance because they are permanently connected in series by the encapsulated transition. However, measurements of the coil pair impedance can track the evolution of the pair's inductance, giving an indication of expected lifetime.

Over the course of the 18 shots, the coil pair's equivalent inductance increased from 740.4 μH (pre-shot measurement) to 768.7 μH (after shot 18). The pre-shot measurement agrees well with the calculated apparent inductance from Maxwell simulations of 739.2 μH. The bottom coil is calculated at 184.3 μH, the upper coil at 459.5 μH, and the mutual inductance term at 47.7 μH. As these electromagnets are repeatedly pulsed, the radial loads on the coil inner diameters will plastically deform the turns, pushing them radially outward until a higher packing fraction can achieve a boundary condition with enough modulus and strength to prevent further movement. It is common to see the inductance of coils without internal reinforcement change 1 – 4% over several shots before the coil stabilizes. This process is known as "coil seating."

The next figure shows the inductance measurements normalized to pre-shot values as they were made intermittently during the 18-shot campaign. It is evident that the coil experienced rapid changes to about 3% higher inductance before stabilizing around 3.8% above the initial value. The stability after seating informs a strong statement that the coil pair is not likely to fail from coarse internal motion of conductors. It is likely that this coil can be used for dozens more shots.

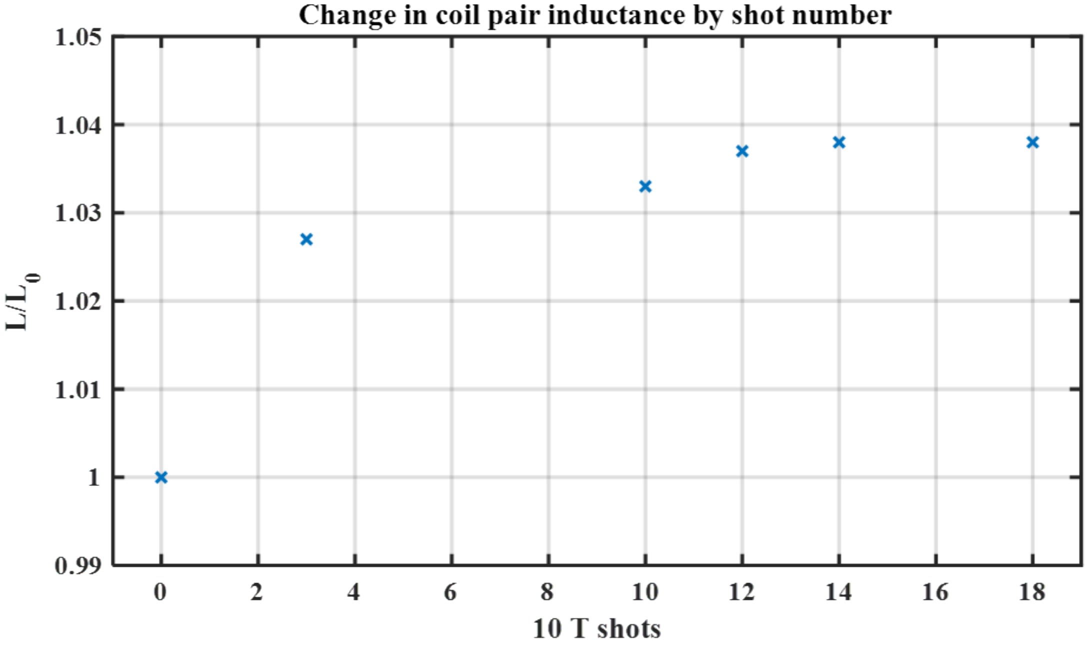

Figure 37: ABM-001 coil inductance measurements normalized to pre-shot values. After 12 shots, the inductance has stabilized as the coil winding seated. This coil pair likely has dozens more shots before another failure mechanism presents (strain, thermal, electrical breakdown).

This varying inductance does have a noticeable impact in the current pulse and resultant field. Inductance scales by diameter, and to zeroth order this inductance change can be approximated by increasing the coil ID by roughly 3.8%. This means the flux density will decrease by the same amount. The current pulse will also lengthen and achieve a lower peak value. The Maxwell calculation was changed to increase the ID by 4%, keeping equal all other coil dimensions. Maxwell's new coil pair with this change is 765.2 μH, in good agreement with the post-18th shot measurement. While this would suggest a reduction of flux density by the change in coil diameter, it is important to note that the ETI+ABM coil shots were shots 5 – 17 in the figure above, a shot range where the coils were already seated to within 1% of the final value. It is reasonable to conclude that there is not significant change in applied field across the campaign.

One item for future work is to complete an effort to directly measure the magnetic field at the location where the ETI barbell would be. This measurement cannot be done in-situ with the barbell installed, but the barbell can be replaced with an on-axis b-dot sensor array that verifies axial magnetic field in the location where the barbell will be. With several probes on an axial array, the variability in the field can be compared to simulation. The scaling factor described earlier for reporting experimental B field can then be verified or further refined. Several attempts at this measurement were made during this project, but issues with calibration and diagnostic returns prevented this final step from being completed by project end.

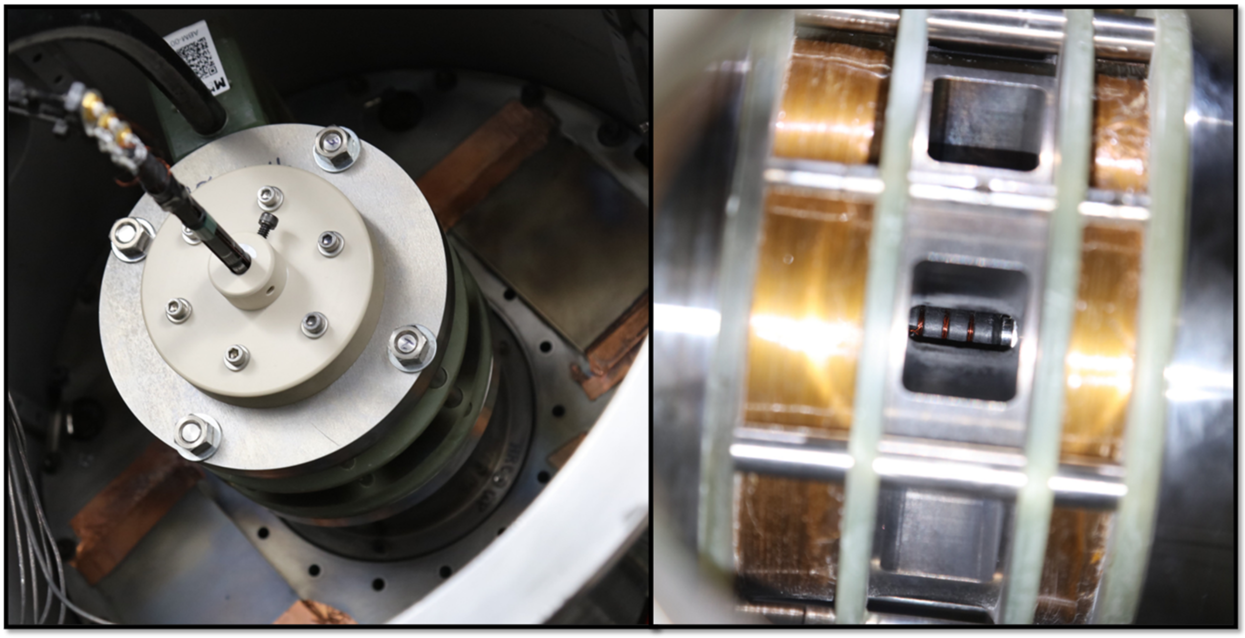

Figure 38: An axial b-dot assembly positions three b-dot sensors on a 6mm rod with 5mm axial spacing between them. The assembly is mounted onto the ABM compression plate (left) and pushed until it engages into the ETI barbell seat on the cathode. The three sensors are on-axis between the coils and visible through a radial diagnostic line of sight (right).

5. ETI + STATIC AXIAL FIELD—EXPERIMENTAL RESULTS

5.1. Target Design and Fabrication

As mentioned in Section 1, simulations of bare ED targets subject to static axial field indicate that the resulatant rotation of the ETI-driven heating topography is much more sublte for static B_z than it is for dynamic B_z (at least for those conditions expected to be achieved in Mykonos experiments). Given the small predcitcted impact on the standard quasi-hemishperical ED, simulations of hemispherical (deeper/higher curvature) ED were also run. These simulations indicate stronger, and likely experimentally observable rotation of the ETI heating topography. As a result, targets with hemispherical ED were designed for static field experiments, as detialed below.

General Atomics fabricated "barbell" targets with hemispherical ED. Starting from the profile specified in SNL drawing J93366_A, the barbell was changed in the following ways (see Fig. 39, below):

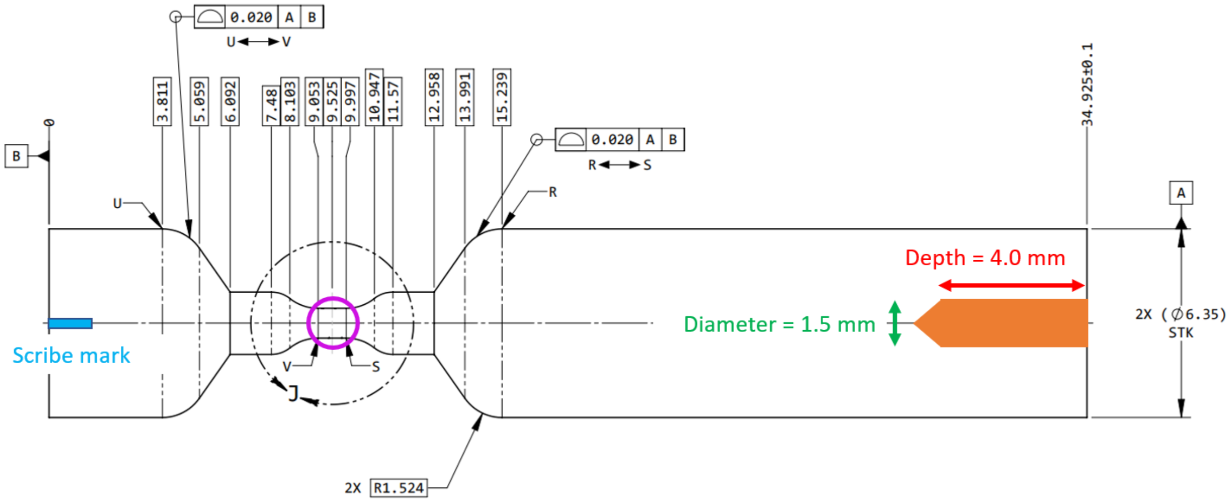

Figure 39. Barbell profile, similar to that in drawing J93366_A, with specified changes.

(1). A counterbore (Fig. 39, orange) will be added to the "long" end of the barbell. Diameter/depth dimensions are notional. A rod (e.g., drill bit) will be inserted into this counterbore to help position the barbell into experimental hardware. Therefore, this is not a precision cut, and the axis of the bore need not be "perfectly" aligned with the axis of the barbell (so the part can be removed from the lathe between cutting the counterbore and the barbell profile, if helpful).

(2). A "scribe" mark shall be placed on the short end of the barbell (Fig. 39, blue). The scribe shall be placed on the "0 degree" side of the target. The scribe must be visible to the naked eye (generally observed as a straight/axial scratch under good lighting).

The ED patterns specified below were added to the Al 5N barbell surface (Fig. 40). In all instances, the horizontal separations are measured about the arc length of the curved cylindrical surface.

ED profiles were cut using a micro-mill to generate the "new" 25-micron-rim-diam., 12.5-micron-deep hemispherical ED. Select targets were coated about the central 1.00-mm-diameter section with 35 microns of optically clear dielectric (Loctite UV cure glue). The Loctite was post machined to a final diameter of 1.070 mm.

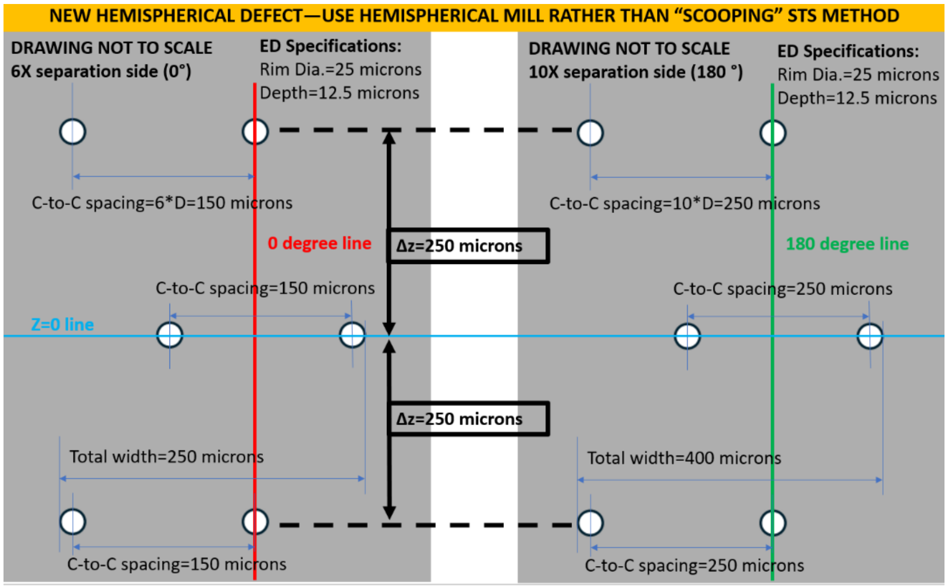

Figure 40. ED pattern #2 specification.

The fabrication process below was followed to generate milled/hemispherical ED targets.

<u>Machining of Uncoated ED Load</u>:

1. Prepare a load "blank" from 1/4" diameter aluminum rod stock by sawing to 1-1/2" long, then facing to 1-3/8" +/-.010" lg. (34.925 +/-0.25) in a manual lathe.
2. Mount blank in a diamond lathe holding by one end in a 1/4" collet mounted in a puck which is held by the lathe's vacuum chuck. Allow ~20mm of blank to extend out of the collet.
3. Position indicator at approximate center of protruding blank, and tap puck radially on vacuum chuck, while rotating by hand, to center blank +/-0.010 approximately. Rough rod OD will limit obtainable accuracy, but it is not important.
4. Using a single crystal diamond tool with 0.025 mm-0.050 mm tip radius, zero top rake, and 15 degree included angle, turn the J93366 A "barbell" shape leaving the 1 mm central dia. 0.0006 mm oversize. This is the "roughing tool."
5. Add required radial ED's using an end mill in a precision milling head which is oriented normal to the lathe spindle axis.
6. Using a new tool of the type described above (in a separate tool holder), turn the central dia. 0.0002 mm oversize. This is the "finishing tool."
7. Re-run ED program, using the same end mill, to remove any burrs that may have been folded into the ED's.

8. Using the finishing tool, turn the central diameter to final, nominal diameter. Final surface Ra of 10 nm – 40 nm is required.
9. Thoroughly clean the load's entire outer surface by flushing with acetone then dry completely by running lathe spindle.
10. Remove load from collet and place in serialized container.

Note: Pressurized mist of odorless mineral spirits (Sigma Aldrich or equivalent) is used for all but the 2 final cuts on the central diameter. A light mineral oil, dripped onto the surface is used for the final cuts.

Characterization of bare/uncoated ED Load:

First Article Inspection (the very first load of each design type shall be inspected as follows before proceeding to machine the remaining loads):

- Central diameter to +/-0.0001 mm precision using laser micrometer.
- Full CT actual-nominal (CAD model) comparison to confirm overall load shape and ED locations.
- Interferometric surface profiler to confirm depth and surface diameter of ED shape.
- Interferometric surface profiler to confirm Ra of central diameter.

In-Process Inspection (by machinist before machining next load):

- Central (1 mm) diameter measured using a laser micrometer.
- Depth and diameter-at-surface of the first and last ED measured on an interferometric surface profiler.

Final Inspection (by inspector before releasing load(s) to customer):

- Central diameter using laser micrometer.
- Interferometric surface profiler to confirm depth and diameter-at-surface of first and last ED of each type.
- Interferometric surface profiler to confirm Ra of central diameter adjacent to ED's.

Application and Machining of Dielectric Coating (if specified):

Note: To ensure concentricity of the dielectric to the underlying Al, do not remove the load to be coated from the lathe after machining, and proceed directly to coating as described below.

1. Thoroughly clean the entire outer surface of uncoated, machined load by flushing with acetone then dry completely by running lathe spindle.
2. Using an optical fiber as an applicator, apply one drop of Loctite 4311 (ethyl cyanoacrylate with photoinitiator) to central area while rotating in lathe at approximately 100 rpm. Prior to deposition, examine drop under high magnification to ensure no air bubbles are present.

3. Cure using handheld UV light source for total of 90 sec. May be broken into 2X @ 45 sec if desired.
4. Using the same finishing tool used to machine the aluminum's central diameter, turn the dielectric central diameter to achieve final dielectric thickness (typically 35um radially).

Note: Pressurized mist of odorless mineral spirits is used for all but the final cut on the central diameter. Mineral oil, dripped onto the surface is used for the final cut.

<u>Characterization of Dielectric Coated Loads</u>:

- Perform First Article, In-process, and Final inspections as described for uncoated loads but with the following differences:
  - Laser micrometer measurements will measure dielectric OD.
  - Interferometer thin film app. is used to measure Ra of dielectric OD and underlying Al.
  - Thin film app. is used to measure dielectric thickness.

Before using, validate this method as follows:

- Diamond turn a test rod to an approximate diameter of 1 mm (programmed radius of 0.5 mm). Actual thickness is unimportant since we are only interested in step height.
- Coat half the rod (axially) with Loctite and cure.
- Using the same diamond tool as in Step 1, without ever removing the load from the lathe, immediately turn the dielectric diameter down using a programmed radius value which is exactly 35 µm larger than the radius programmed for the rod turning. The resulting radial step height expected is 35 µm exactly as a result of the sub-µm accuracy of the machine's linear movements.
- Check the step height on an interferometric surface profiler by comparing fringes on top of the dielectric vs. fringes directly on top of the rod (i.e., not looking through the dielectric). This should give the expected 35 µm film thickness.
- Finally, use the thin film app. to look through the dielectric (since this is the method by which the actual loads will be measured). An IR parameter setting of "1.5" should result in the correct film thickness result (35 µm). Adjust IR parameter as required to obtain this value.

Note: It has been suggested that milled ED's may have more burrs than those made by the scooping method used in the past, and burrs may be confounding the experimental results. One possible explanation for the burrs would be the unavoidable fact that carbide ball end mills are not nearly as sharp as the single crystal diamond tools used for the scooping method, Unfortunately, due to tool clearance considerations, it does not seem possible to use the scooping method to form ED's beyond the 106-degree spherical sector used in the scooped ED so far. So, it seems, therefore, at present, milling is the only method available to us for forming a 180-degree, hemispherical ED.

5.2. Experimental Execution and Results

The first ABM/ED experiments were executed in April of 2025. Entering the experiments, it was expected, based on simulations, that ETI rotation due to static B_z might be subtle. Furthermore, based on previous experience in fielding new targets and/or sub-systems, the experimenters acknowledged the risk that the hemispherical/milled ED may fail to meet experimental requirements, and/or the ABM capability may not perform as expected.

Table 1 includes shot-by-shot information on the first set of ABM experiments, where the key variables were (1) whether static B_z was applied using the ABM capability, (2) which type of target was fielded, (3) the ICCD imager settings.

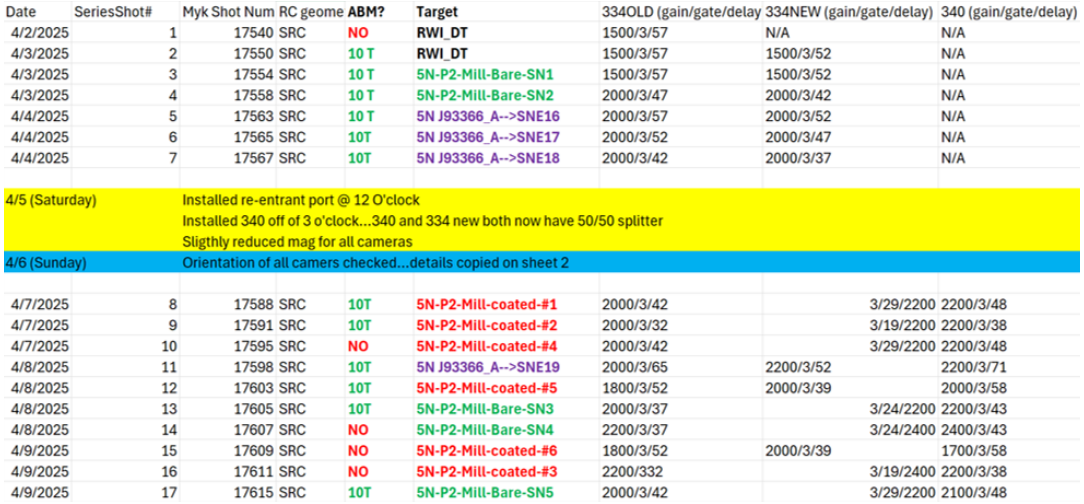

Date	SeriesShot#	Myk Shot Num	RC geome	**ABM?**	**Target**	334OLD (gain/gate/delay	334NEW (gain/gate/delay)	340 (gain/gate/delay)
4/2/2025	1	17540	SRC	**NO**	**RWI_DT**	1500/3/57	N/A	N/A
4/3/2025	2	17550	SRC	**10 T**	**RWI_DT**	1500/3/57	1500/3/52	N/A
4/3/2025	3	17554	SRC	**10 T**	**5N-P2-Mill-Bare-SN1**	1500/3/57	1500/3/52	N/A
4/3/2025	4	17558	SRC	**10 T**	**5N-P2-Mill-Bare-SN2**	2000/3/47	2000/3/42	N/A
4/4/2025	5	17563	SRC	**10 T**	**5N J93366_A-->SNE16**	2000/3/57	2000/3/52	N/A
4/4/2025	6	17565	SRC	**10T**	**5N J93366_A-->SNE17**	2000/3/52	2000/3/47	N/A
4/4/2025	7	17567	SRC	**10T**	**5N J93366_A-->SNE18**	2000/3/42	2000/3/37	N/A
4/5 (Saturday)		Installed re-entrant port @ 12 O'clock Installed 340 off of 3 o'clock...340 and 334 new both now have 50/50 splitter Sligthly reduced mag for all cameras						
4/6 (Sunday)		Orientation of all camers checked...details copied on sheet 2						
4/7/2025	8	17588	SRC	**10T**	**5N-P2-Mill-coated-#1**	2000/3/42	3/29/2200	2200/3/48
4/7/2025	9	17591	SRC	**10T**	**5N-P2-Mill-coated-#2**	2000/3/32	3/19/2200	2200/3/38
4/7/2025	10	17595	SRC	**NO**	**5N-P2-Mill-coated-#4**	2000/3/42	3/29/2200	2200/3/48
4/8/2025	11	17598	SRC	**10T**	**5N J93366_A-->SNE19**	2000/3/65	2200/3/52	2200/3/71
4/8/2025	12	17603	SRC	**10T**	**5N-P2-Mill-coated-#5**	1800/3/52	2000/3/39	2000/3/58
4/8/2025	13	17605	SRC	**10T**	**5N-P2-Mill-Bare-SN3**	2000/3/37	3/24/2200	2200/3/43
4/8/2025	14	17607	SRC	**NO**	**5N-P2-Mill-Bare-SN4**	2200/3/37	3/24/2400	2400/3/43
4/9/2025	15	17609	SRC	**NO**	**5N-P2-Mill-coated-#6**	1800/3/52	2000/3/39	1700/3/58
4/9/2025	16	17611	SRC	**NO**	**5N-P2-Mill-coated-#3**	2200/332	3/19/2400	2200/3/38
4/9/2025	17	17615	SRC	**10T**	**5N-P2-Mill-Bare-SN5**	2000/3/42	3/29/2200	2100/3/48

Target	**Bz**	**# shots**	**Logic on #**
Milled Bare	0	1	Burrs strongly impact heating of bare ED, large existing ED dataset at 0 T
Milled Bare	10 T	4	Focus of campaign
Milled Coated	0	3	Compare hemisphere to existing quasi-hem dataset at 0 T
Milled Coated	10 T	3	Focus of campaign
Scooped Bare	0	0	No targets available
Scooped Bare	10 T	0	No targets available
Scooped Coated	0	0	Large existing ED dataset at 0 T
Scooped Coated	10 T	4	See if any impact can be observed with more reproducible ED

Table 1. Experimental parameters and setup

The first experiments used a "RWI" target (low cost, not diamond turned, no ED), and did not use ABM (B_z=0). It was intended simply to ensure the Mykonos Facility, and imaging diagnostics were functioning as expected. The second experiment again used a RWI target, but here, prior to the shot, we commissioned the ABM capability by firing ABM multiple times at progressively higher charge voltage (without firing Mykonos). We were able to observe small movements in the target due the ABM magnetic field pulse, confirming the utility/necessity of the barbell retaining cup (see Fig. 27 and discussion). Finally, shot 2 was executed (by firing Mykonos), data was obtained, and the ABM capability was successfully commissioned on Mykonos.

Next, we transitioned to studies of the new milled/hemispherical target type, uncoated, with ABM pulsed to generate a 10 T axial field. The results were quite disappointing (see Fig. 41), in that while all measurements indicated that ABM performed as expected, the heating pattern observed from ED was highly non-uniform and was not reproducible from one ED to the next. Given previous experience, this immediately suggested that the ED rims may have imperfections (e.g., burrs) which could be driving local heating sufficient to overwhelm any changes associated with the addition of static B_z. The remainder of the series was intended to:

1. Evaluate bare/milled/hemispherical ED both with and without B_z=10 T applied by ABM
2. Evaluate coated/milled/hemispherical ED both with and without B_z=10 T applied by ABM
    a. Here, we hoped the addition of the coating might slow the heating associated with rim imperfections (which has been observed in previous studies) perhaps allowing heating pattern rotations to be observed.
3. Evaluate scooped/quasi-hemispherical targets (both bare and dielectric coated) both with and without B_z=10 T applied by ABM
    a. Here, we had higher confidence that rim imperfections would not dominate (given our earlier HRC studies, and the proven machining method), and wanted to determine whether rotations due to static B_z could be observed, even though simulations suggested such rotations, while present, would be extremely subtle.

Self-emission imaging data from milled/hemispherical ED targets are included in Figs. 41-43. First, Fig. 41 shows data from bare targets, where the emissions around the ED rim appear quite random, with the locations of brightest emission being largely irreproducible from one ED to the next, even within the same target. This appears to be generally true, regardless of whether ABM provided 10 T axial field, or not. Next, Fig. 42 shows data from dielectric coated targets. Here, given the tamping affect of the coating, the heating pattern has changed significantly, and appears to be more reproducible from on ED to the next. But, when comparing data from B_z=0 and B_z=10 T experiments, there is no obvious rotation observed. Upon more detailed inspection (Fig. 43), zooming in on individual ED heating patterns from a single experimental target shows significant variations in the micron scale heating, presumably, again, indicating that variations in the ED profiles may be driving irreproducible emissions.

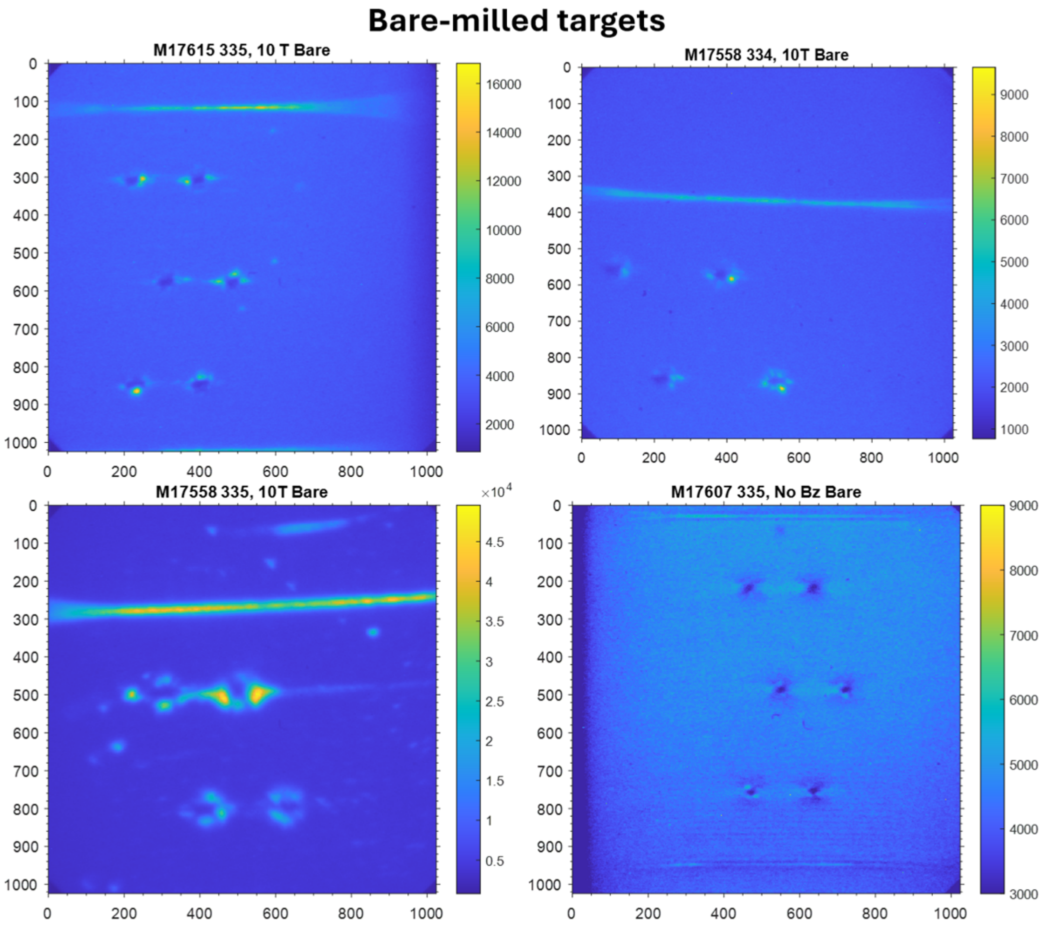

Figure 41. Self-emission images from bare milled/hemispherical ED showing largely random rim heating, presumably due to machining imperfections.

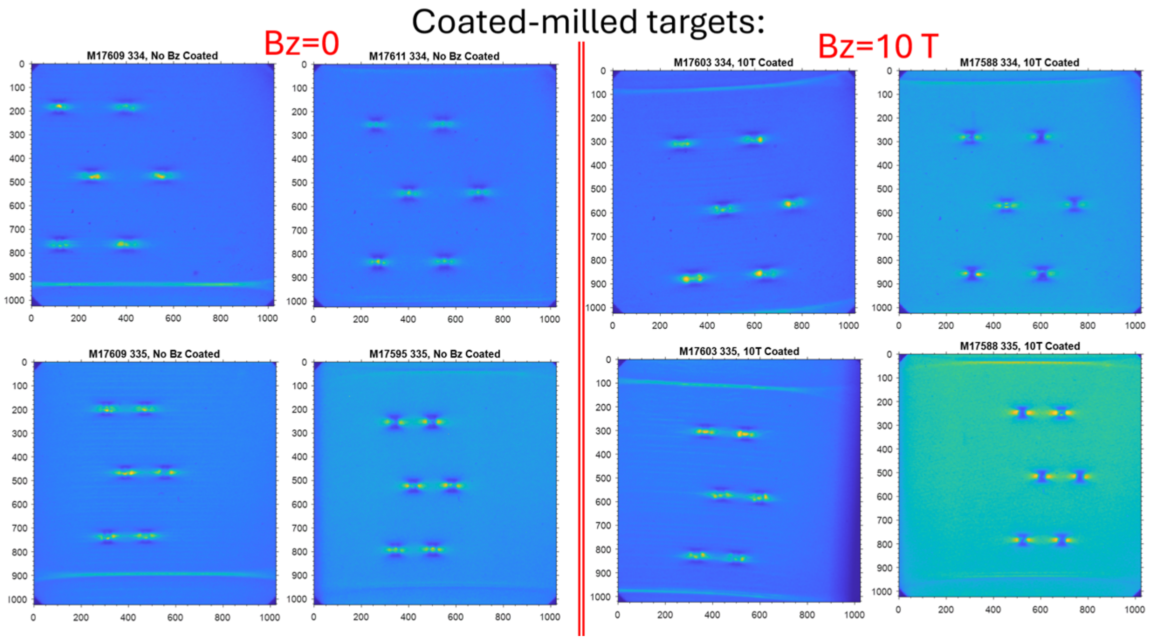

Figure 42. Self-emission images from dielectric coated milled/hemispherical ED. On the left is data from experiments where ABM was not fired (B_z=0) whereas on the right, B_z=10 T static field was applied. No clear change is observed for these different axial field configurations.

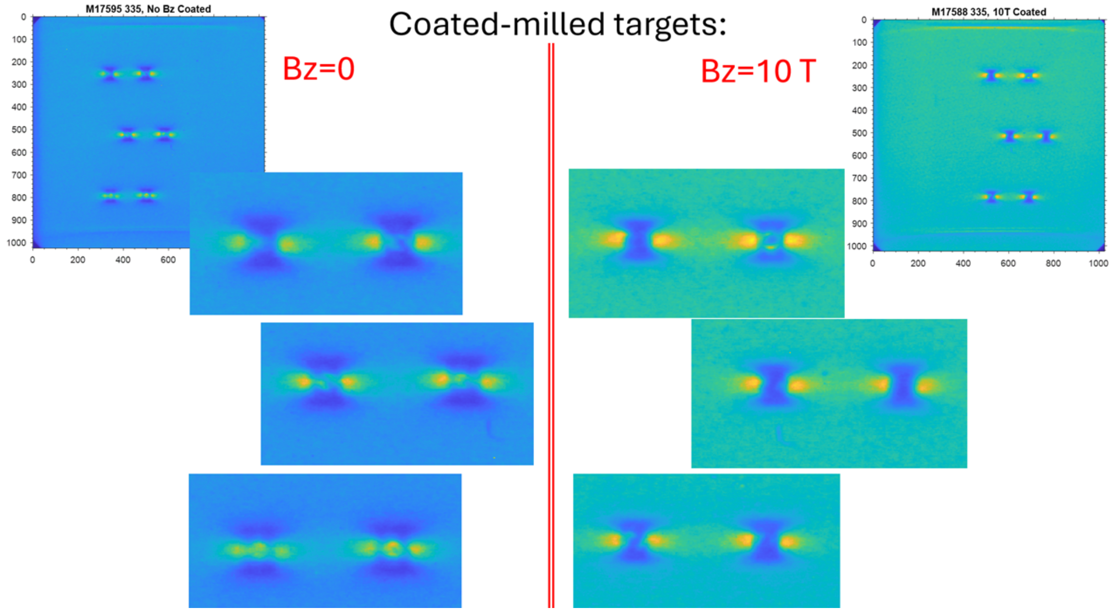

Figure 43. Self-emission images from dielectric coated milled/hemispherical ED. On the left is data from experiments where ABM was not fired (B_z=0) whereas on the right, B_z=10 T static field was applied. The data in the images are then cropped to better display the heating about ED. This shows that within a single image, the heating patterns contain a variety of asymmetric features, presumably due to imperfections in the machined ED profiles.

Interferometric scans of ED were gathered before Mykonos experiments, and are used to both characterize the surface roughness of the physics target, but also the size, shape, and rim quality of the machined ED. Below, in Fig. 44, is a sample of data from 8 ED, gathered from multiple targets. The ED rims vary both in shape (some are not round) and in the location/size of rim imperfections (folded over material and burrs). It is likely that these variable features contributed to the variable self-emission structures observed in experiments.

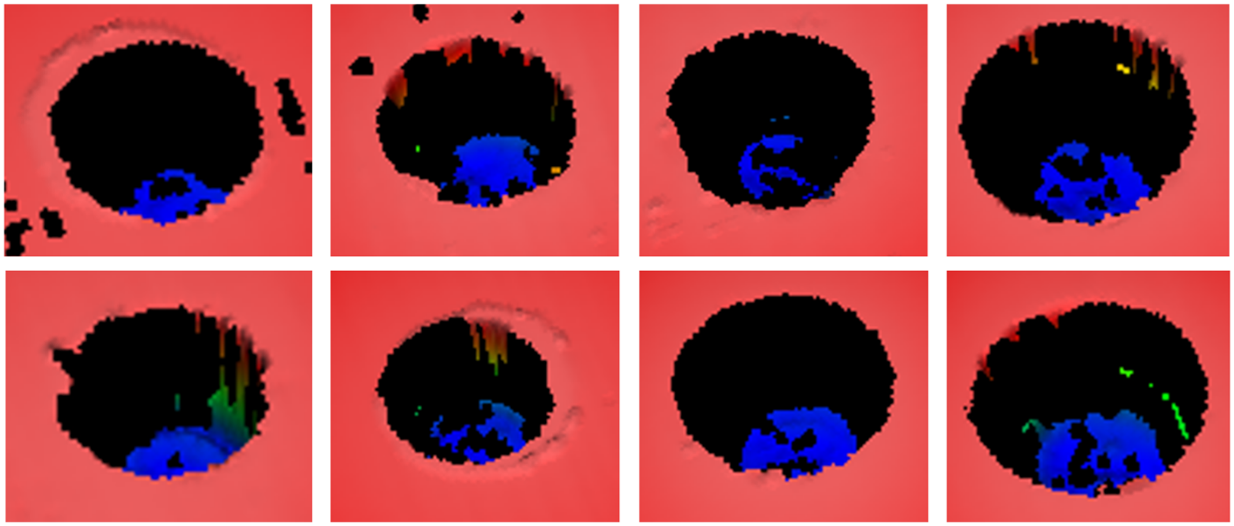

Figure 44. Interferometry data of a sample of milled/hemispherical ED, showing ED rims vary both in shape (some are not round) and in the location/size of rim imperfections (folded over material and burrs)

Finally, given the concerns of rim imperfection on the milled/hemispherical ED, we chose to execute a series of experiments using the scooped-quasi-hemispherical ED targets used in the dynamic field (HRC) experiments discussed previously. In Fig. 45, we show on the right, data reported previously on the merging of ED pairs along the surface field polarization angle, ϕ_B, for the HRC experiments (please see the full discussion in the recent publication). The panel to the left in Fig. 45 shows data from experiments where ABM provided a 10 T static axial field. Here, ED pair merging appears to be strongest for those ED which are horizontally oriented (ϕ_{ED}=0). This may not be surprising, given that by the time these images were gathered, in the absence of mechanisms like flux compression, the azimuthal surface field exceed the B_z=10 T axial field by a factor of 10 or more. Future work will compare this dataset to the previously obtained B_z=0 dataset to see if any change in heating topography can be attributed to the application of the static axial field.

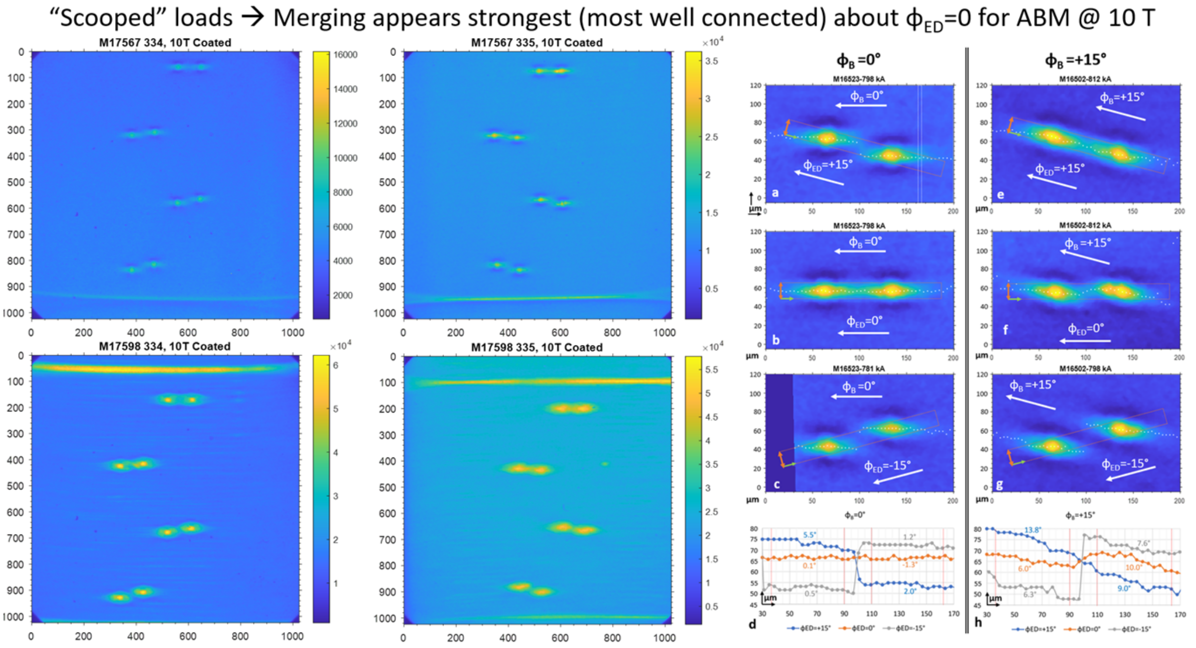

“Scooped” loads → Merging appears strongest (most well connected) about $\phi_{ED}=0$ for ABM @ 10 T

Figure 45. Self-emission data from dielectric coated targets with scooped/quasi-hemispherical ED. In the left panel, we see data from experiments where ABM applied 10 T static field. The right panel is a data from experiments which used similar targets, but applied a 15° surface field polarization using a helical return can.

REFERENCES

---

[i] T.J. Awe, E.P. Yu, G.A. Shipley, K.C. Yates, K. Tomlinson, and M. Hatch. Rotation of electrothermal-instability-driven overheating structure due to helically oriented surface magnetic field on a high-current-density aluminum rod. Phys. Plasmas 32, 082109 (2025).
DOI: https://doi.org/10.1063/5.0279628

[ii] I. R. Lindemuth, Two-dimensional fiber ablation in the solid-deuterium Z pinch, Phys. Rev. Lett. 65, 179 (1990).
DOI: https://doi.org/10.1103/PhysRevLett.65.179

[iii] J.E. Hammel, D.W. Scudder, J.S. Shlachter, Recent results on dense Z pinches, Nuclear Instruments and Methods in Physics Research, Volume 207, Issues 1–2, 1983, Pages 161-168, ISSN 0167-5087,
DOI: https://doi.org/10.1016/0167-5087(83)90233-8

[iv] U. Shumlak; Z-pinch fusion. *J. Appl. Phys.* 127, 200901 (2020).
DOI: https://doi.org/10.1063/5.0004228

[v] J.E. Bailey, G. A. Chandler, S. A. Slutz, G. R. Bennett, G. Cooper, J. S. Lash, S. Lazier, R. Lemke, T. J. Nash, D. S. Nielsen, T. C. Moore, C. L. Ruiz, D. G. Schroen, R. Smelser, J. Torres, and R. A. Vesey, X-Ray Imaging Measurements of Capsule Implosions Driven by a Z-Pinch Dynamic Hohlraum, Phys. Rev. Lett. 89, 095004 (2002).
DOI: https://doi.org/10.1103/PhysRevLett.89.095004

[vi] A. L. Velikovich, R. W. Clark, J. Davis, Y. K. Chong, C. Deeney, C. A. Coverdale, C. L. Ruiz, G. W. Cooper, A. J. Nelson, J. Franklin, L. I. Rudakov, Z-pinch plasma neutron sources. *Phys. Plasmas*, 14, 022701 (2007).
DOI: https://doi.org/10.1063/1.2435322

[vii] C. A. Coverdale, C. Deeney, A. L. Velikovich, R. W. Clark, Y. K. Chong, J. Davis, J. Chittenden, C. L. Ruiz, G. W. Cooper, A. J. Nelson, J. Franklin, P. D. LePell, J. P. Apruzese, J. Levine, J. Banister, N. Qi; Neutron production and implosion characteristics of a deuterium gas-puff Z pinch. *Phys. Plasmas* 14, 022706 (2007).
DOI: https://doi.org/10.1063/1.2446177

[viii] J. E. Bailey; G. A. Chandler; R. C. Mancini; S. A. Slutz; G. A. Rochau; M. Bump; T. J. Buris-Mog; G. Cooper; G. Dunham; I. Golovkin; J. D. Kilkenny; P. W. Lake; R. J. Leeper; R. Lemke; J. J. MacFarlane; T. A. Mehlhorn; T. C. Moore; T. J. Nash; A. Nikroo; D. S. Nielsen; K. L. Peterson; C. L. Ruiz; D. G. Schroen; D. Steinman; W. Varnum, Dynamic hohlraum radiation hydrodynamics, Phys. Plasmas, **13**, No. 5, 056301 (2006).
DOI: https://doi.org/10.1063/1.2177640

[ix] G A Rochau, J E Bailey, G A Chandler, G Cooper, G S Dunham, P W Lake, R J Leeper, R W Lemke, T A Mehlhorn, A Nikroo, K J Peterson, C L Ruiz, D G Schroen, S A Slutz, D Steinman, W A Stygar and W Varnum, High performance capsule implosions driven by the Z-pinch dynamic hohlraum, Plasma Phys. Control. Fusion, **49**, B591 (2007).
DOI: 10.1088/0741-3335/49/12B/S55

---

[x] G. A. Rochau, J. E. Bailey, R. E. Falcon, G. P. Loisel, T. Nagayama, R. C. Mancini, I. Hall, D. E. Winget, M. H. Montgomery, and D. A. Liedahl, “ZAPP: The Z astrophysical plasma properties collaboration,” Phys. Plasmas 21, 056308 (2014).
DOI: https://doi.org/10.1063/1.4875330

[xi] I.R. Lindemuth and R.C. Kirkpatrick, Parameter space for magnetized fuel targets in inertial confinement fusion, Nucl. Fusion 23, 263 (1983).
DOI: 10.1088/0029-5515/23/3/001

[xii] Y. B. Khariton, Usp. Fiziol. Nauk 120, 706 (1976) [Sov. Phys. Usp. 19, 1032 (1976)].

[xiii] Y C F Thio, Status of the U. S. program in magneto-inertial fusion, J. Phys.: Conf. Ser. 112 042084, (2008).
DOI: 10.1088/1742-6596/112/4/042084

[xiv] S. A. Slutz, M. C. Herrmann, R. A. Vesey, A. B. Sefkow, D. B. Sinars, D. C. Rovang, K. J. Peterson, and M. E. Cuneo, Pulsed-power-driven cylindrical liner implosions of laser preheated fuel magnetized with an axial field, Phys. Plasmas 17, 056303 (2010).
DOI: https://doi.org/10.1063/1.3333505

[xv] S. A. Slutz and R. A. Vesey, High-Gain Magnetized Inertial Fusion, Phys. Rev. Lett. 108, 025003 (2012).
DOI: https://doi.org/10.1103/PhysRevLett.108.025003

[xvi] M. E. Cuneo, M. C. Herrmann, D. B. Sinars, S. A. Slutz, W. A. Stygar, R. A. Vesey, A. B. Sefkow, G. A. Rochau, G. A. Chandler, J. E. Bailey, J. L. Porter, R. D. McBride, D. C. Rovang, M. G. Mazarakis, E. P. Yu, D. C. Lamppa, K. J. Peterson, C. Nakhleh, S. B. Hansen, A. J. Lopez, M. E. Savage, C. A. Jennings, M. R. Martin, R. W. Lemke, B. W. Atherton, I. C. Smith, P. K. Rambo, M. Jones, M. R. Lopez, P. J. Christenson, M. A. Sweeney, B. Jones, L. A. McPherson, E. Harding, M. R. Gomez, P. F. Knapp, T. J. Awe, R. J. Leeper, C. L. Ruiz, G. W. Cooper, K. D. Hahn, J. McKenney, A. C. Owen, G. R. McKee, G. T. Leifeste, D. J. Ampleford, E. M. Waisman, A. Harvey-Thompson, R. J. Kaye, M. H. Hess, S. E. Rosenthal, and M. K. Matzen, Magnetically Driven Implosions for Inertial Confinement Fusion at Sandia National Laboratories, IEEE Trans. Plasma Sci. 40, 3222 (2012).
DOI: 10.1109/TPS.2012.2223488

[xvii] A.B.Sefkow, S.A. Slutz, J.M. Koning, M.M. Marinak, K.J. Peterson, D.B. Sinars, and R.A. Vesey, Design of magnetized liner inertial fusion experiments using the Z facility, Phys. Plasmas **21**, 072711 (2014).
DOI: https://doi.org/10.1063/1.4890298

[xviii] M.R. Gomez, S.A. Slutz, A.B. Sefkow, D.B. Sinars, K.D. Hahn, S.B. Hansen, E.C. Harding, P.F. Knapp, P.F. Schmit, C.A. Jennings, T.J. Awe, M. Geissel, D.C. Rovang, G.A. Chandler, G.W. Cooper, M.E. Cuneo, A.J. Harvey-Thompson, M.C. Herrmann, M.H. Hess, O. Johns, D.C. Lamppa, M.R. Martin, R.D. McBride, K.J. Peterson, J.L. Porter, G.K. Robertson, G.A. Rochau, C.L. Ruiz, M.E. Savage, I.C. Smith, W.A. Stygar, R.A. Vesey, Phys. Rev. Lett. 113, 155003 (2014).
DOI: https://doi.org/10.1103/PhysRevLett.113.155003

[xix] D. C. Rovang, D. C. Lamppa, M. E. Cuneo, A. C. Owen, J. McKenney, D. W. Johnson, S. Radovich, R. J. Kaye, R. D. McBride, C. S. Alexander, T. J. Awe, S. A. Slutz, A. B. Sefkow, T. A. Haill, P. A. Jones, J. W. Argo, D. G. Dalton, G. K. Robertson, E. M. Waisman, D. B. Sinars, J. Meissner, M. Milhous, D. N. Nguyen, and C. H. Mielke, Pulsed-coil magnet systems for applying uniform 10–30 T fields to centimeter-scale targets on Sandia's Z facility, Rev. Sci. Instrum. **85**, 124701 (2014).
DOI: https://doi.org/10.1063/1.4902566

[xx] M.R. Gomez, S.A. Slutz, A.B. Sefkow, K.D. Hahn, S.B. Hansen, P.F. Knapp, P.F. Schmit, C.L. Ruiz, D.B. Sinars, E.C. Harding, C.A. Jennings, T.J. Awe, M. Geissel, D.C. Rovang, I.C. Smith, G.A. Chandler, G.W. Cooper, M.E. Cuneo, A.J. Harvey-Thompson, M.C. Herrmann, M.H. Hess, D.C. Lamppa, M.R. Martin, R.D. McBride, K.J. Peterson, J.L. Porter, G.A. Rochau, M.E. Savage, D.G. Schroen, W.A. Stygar, R.A. Vesey, Demonstration of thermonuclear conditions in magnetized liner inertial fusion experiments, Phys. Plasmas 22, 056306 (2015).
DOI: https://doi.org/10.1063/1.4919394

[xxi]. M.R. Gomez, S.A. Slutz, C.A. Jennings, D.J. Ampleford, M.R. Weis, C.E. Myers, D.A. Yager-Elorriaga, K.D. Hahn, S.B. Hansen, E.C. Harding, A.J. Harvey-Thompson, D.C. Lamppa, M. Mangan, P.F. Knapp, T.J. Awe, G.A. Chandler, G.W. Cooper, J.R. Fein, M. Geissel, M.E. Glinsky, W.E. Lewis, C.L. Ruiz, D.E. Ruiz, M.E. Savage, P.F. Schmit, I.C. Smith, J.D. Styron, J.L. Porter, B. Jones, T.R. Mattsson, K.J. Peterson, G.A. Rochau, D.B. Sinars, Performance Scaling in Magnetized Liner Inertial Fusion Experiments, Phys. Rev. Lett. 125, 155002 (2020).
DOI: https://doi.org/10.1103/PhysRevLett.125.155002

[xxii] P.F. Schmit, P.F. Knapp, S.B. Hansen, M.R. Gomez, K.D. Hahn, D.B. Sinars, K.J. Peterson, S.A. Slutz, A.B. Sefkow, T.J. Awe, E. Harding, C.A. Jennings, G.A. Chandler, G.W. Cooper, M.E. Cuneo, M. Geissel, A.J. Harvey-Thompson, M.C. Herrmann, M.H. Hess, O. Johns, D.C. Lamppa, M.R. Martin, R.D. McBride, J.L. Porter, G.K. Robertson, G.A. Rochau, D.C. Rovang, C.L. Ruiz, M.E. Savage, I.C. Smith, W.A. Stygar, R.A. Vesey, Understanding Fuel Magnetization and Mix Using Secondary Nuclear Reactions in Magneto-Inertial Fusion, Phys. Rev. Lett. 113, 155004 (2014).
DOI: https://doi.org/10.1103/PhysRevLett.113.155004

[xxiii] P.F. Knapp, P.F. Schmit, S.B. Hansen, M.R. Gomez, K.D. Hahn, D.B. Sinars, K.J. Peterson, S.A. Slutz, A.B. Sefkow, T.J. Awe, E. Harding, C.A. Jennings, M.P. Desjarlais, G.A. Chandler, G.W. Cooper, M.E. Cuneo, M. Geissel, A.J. Harvey-Thompson, J.L. Porter, G.A. Rochau, D.C. Rovang, C.L. Ruiz, M.E. Savage, I.C. Smith, W.A. Stygar, M.C. Herrmann, Effects of magnetization on fusion product trapping and secondary neutron spectra, Phys. Plasmas 22, 056312 (2015).
DOI: https://doi.org/10.1063/1.4920948

[xxiv] T.J. Awe, R. D. McBride, C. A. Jennings, D. C. Lamppa, M. R. Martin, D. C. Rovang, S. A. Slutz, M. E. Cuneo, A. C. Owen, D. B. Sinars, K. Tomlinson, M. R. Gomez, S. B. Hansen, M. C. Herrmann, J. L. McKenney, C. Nakhleh, G. K. Robertson, G. A. Rochau, M. E. Savage, D. G. Schroen, and W. A. Stygar, Observations of Modified Three-Dimensional Instability Structure for Imploding *z*-Pinch Liners that are Premagnetized with an Axial Field, Phys. Rev. Lett. **111**, 235005 (2013).
DOI: DOI: https://doi.org/10.1103/PhysRevLett.111.235005

[xxv] T. J. Awe, C. A. Jennings, R. D. McBride, M. E. Cuneo, D. C. Lamppa, M. R. Martin, D. C. Rovang, D. B. Sinars, S. A. Slutz, A. C. Owen, K. Tomlinson, M. R. Gomez, S. B. Hansen, M. C. Herrmann, M. C. Jones, J.

L. McKenney, G. K. Robertson, G. A. Rochau, M. E. Savage, D. G. Schroen, and W. A. Stygar, Modified helix-like instability structure on imploding z-pinch liners that are pre-imposed with a uniform axial magnetic field, Phys. Plasmas **21**, 056303 (2014).
DOI: https://doi.org/10.1063/1.4872331

[xxvi] R. D. McBride, S. A. Slutz, C. A. Jennings, D. B. Sinars, M. E. Cuneo, M. C. Herrmann, R. W. Lemke, M. R. Martin, R. A. Vesey, K. J. Peterson, A. B. Sefkow, C. Nakhleh, B. E. Blue, K. Killebrew, D. Schroen, T. J. Rogers, A. Laspe, M. R. Lopez, I. C. Smith, B. W. Atherton, M. Savage, W. A. Stygar, and J. L. Porter, Penetrating Radiography of Imploding and Stagnating Beryllium Liners on the Z Accelerator, Phys. Rev. Lett. 109, 135004 (2012).
DOI: 10.1103/PhysRevLett.109.135004

[xxvii] R. D. McBride, M. R. Martin, R. W. Lemke, J. B. Greenly, C. A. Jennings, D. C. Rovang, D. B. Sinars, M. E. Cuneo, M. C. Herrmann, S. A. Slutz, C. W. Nakhleh, D. D. Ryutov, J.-P. Davis, D. G. Flicker, B. E. Blue, K. Tomlinson, D. Schroen, R. M. Stamm, G. E. Smith, J. K. Moore, T. J. Rogers, G. K. Robertson, R. J. Kamm, I. C. Smith, M. Savage, W. A. Stygar, G. A. Rochau, M. Jones, M. R. Lopez, J. L. Porter, and M. K. Matzen, Beryllium liner implosion experiments on the Z accelerator in preparation for magnetized liner inertial fusion, Phys. Plasmas **20**, 056309 (2013).
DOI: https://doi.org/10.1063/1.4803079

[xxviii] P. F. Schmit, A. L. Velikovich, R. D. McBride, and G. K. Robertson, Controlling Rayleigh-Taylor Instabilities in Magnetically Driven Solid Metal Shells by Means of a Dynamic Screw Pinch, Phys. Rev. Lett. 117, 205001 (2016).
DOI: https://doi.org/10.1103/PhysRevLett.117.205001

[xxix] G. A. Shipley, C. A. Jennings, and P. F. Schmit, Design of dynamic screw pinch experiments for magnetized liner inertial fusion, Phys. Plasmas 26, 102702 (2019).
DOI: https://doi.org/10.1063/1.5120529

[xxx] G. A. Shipley, D. E. Ruiz, C. A. Jennings, D. A. Yager-Elorriaga, and P. F. Schmit, Numerical study of implosion instability mitigation in magnetically driven solid liner dynamic screw pinches, Phys. Plasmas 31, 022704 (2024).
DOI: https://doi.org/10.1063/5.0189042

[xxxi] V. I. Oreshkin, Thermal instability during an electrical wire explosion, Phys. Plasmas 15, 092103 (2008).
DOI: https://doi.org/10.1063/1.2966121

[xxxii] A. G. Rousskikh, V. I. Oreshkin, S. A. Chaikovsky, N. A. Labetskaya, A. V. Shishlov, I. I. Beilis, and R. B. Baksht, Study of the strata formation during the explosion of a wire in vacuum, Phys. Plasmas 15, 102706 (2008).
DOI: https://doi.org/10.1063/1.3000390

[xxxiii] K. J. Peterson, D. B. Sinars, E. P. Yu, M. C. Herrmann, M. E. Cuneo, S. A. Slutz, I. C. Smith, B. W. Atherton, M. D. Knudson, and C. Nakhleh, Electrothermal instability growth in magnetically driven pulsed power liners, Phys. Plasmas 19, 092701 (2012).
DOI: https://doi.org/10.1063/1.4751868

[xxxiv] A. B. Sefkow, “On the helical instability and efficient stagnation pressure production in thermonuclear magnetized inertial fusion,” invited talk at 58th Annual Meeting of American Physical Society Division of Plasma Physics [Bull. Am. Phys. Soc. 61(18), UI3.00006 (2016)].
[xxxv] D. D. Ryutov, T. J. Awe, S. B. Hansen, R. D. McBride, K. J. Peterson, D. B. Sinars, and S. A. Slutz, Effect of axial magnetic flux compression on the helical mode of the magnetic Rayleigh-Taylor instability (theory), AIP Conf. Proc. 1639, 63–66 (2014).
DOI: https://doi.org/10.1063/1.4904778

[xxxvi] C. E. Seyler, M. R. Martin, and N. D. Hamlin, Helical instability in MagLIF due to axial flux compression by low-density plasma, Phys. Plasmas 25, 062711 (2018).
DOI: https://doi.org/10.1063/1.5028365
[xxxvii] C. E. Seyler, Axial magnetic flux amplification in Hall-magnetohydrodynamic simulations of externally magnetized z-pinches, Phys. Plasmas 27, 092102 (2020).
DOI: https://doi.org/10.1063/5.0011833

[xxxviii] J.M. Woolstrum, C.E. Seyler, and R.D. McBride, Hall instability driven seeding of helical magneto-Rayleigh–Taylor instabilities in axially premagnetized thin-foil liner Z-pinch implosions, Phys. Plasmas, 29, 122701 (2022).
DOI: https://doi.org/10.1063/5.0103651

[xxxix] J.M. Woolstrum, D.E. Ruiz, N.D. Hamlin, K. Beckwith, and M.R. Martin, Hall interchange instability as a seed for helical magneto Rayleigh–Taylor instabilities in magnetized liner inertial fusion Z-Pinches scaled from Z-Machine parameters to a next generation pulsed power facility, Phys. Plasmas, 30, 072712 (2023).
DOI: https://doi.org/10.1063/5.0156806

[xl] M. R. Weis, P. Zhang, Y. Y. Lau, P. F. Schmit, K. J. Peterson, M. Hess, R. M. Gilgenbach, Coupling of sausage, kink, and magneto-Rayleigh-Taylor instabilities in a cylindrical liner. *Phys. Plasmas*, 22 032706 (2015).
DOI: https://doi.org/10.1063/1.4915520

[xli] L. Atoyan, D. A. Hammer, B. R. Kusse, T. Byvank, A. D. Cahill, J. B. Greenly, S. A. Pikuz, T. A. Shelkovenko, Helical plasma striations in liners in the presence of an external axial magnetic field. *Phys. Plasmas*, 23, 022708 (2016).
DOI: https://doi.org/10.1063/1.4942787

[xlii] D. A. Yager-Elorriaga, P. Zhang, A. M. Steiner, N. M. Jordan, P. C. Campbell, Y. Y. Lau, R. M. Gilgenbach, Discrete helical modes in imploding and exploding cylindrical, magnetized liners. *Phys. Plasmas*, 23, 124502 (2016).
DOI: https://doi.org/10.1063/1.4969082

[xliii] D. A. Yager-Elorriaga, P. Zhang, A. M. Steiner, N. M. Jordan, Y. Y. Lau, R. M. Gilgenbach, Seeded and unseeded helical modes in magnetized, non-imploding cylindrical liner-plasmas. *Phys. Plasmas,* 23 101205 (2016).
DOI: https://doi.org/10.1063/1.4965240

[xliv] D. A. Yager-Elorriaga, Y. Y. Lau, P. Zhang, P. C. Campbell, A. M. Steiner, N. M. Jordan, R. D. McBride, R. M. Gilgenbach, Evolution of sausage and helical modes in magnetized thin-foil cylindrical liners driven by a Z-pinch. *Phys. Plasmas*, 25, 056307 (2018).
DOI: https://doi.org/10.1063/1.5017849

[xlv] P. C. Campbell, T. M. Jones, J. M. Woolstrum, N. M. Jordan, P. F. Schmit, J. B. Greenly, W. M. Potter, E. S. Lavine, B. R. Kusse, D. A. Hammer, and R. D. McBride, Stabilization of liner implosions via a dynamic screw pinch, Phys. Rev. Lett. 125, 035001 (2020).
DOI: https://doi.org/10.1103/PhysRevLett.125.035001

[xlvi] Paul C. Campbell, T. M. Jones, J. M. Woolstrum, N. M. Jordan, P. F. Schmit, A. L. Velikovich, J. B. Greenly, W. M. Potter, E. S. Lavine, B. R. Kusse, D. A. Hammer, R. D. McBride, Liner implosion experiments driven by a dynamic screw pinch. *Phys. Plasmas*, 28, 082707 (2021).
DOI: https://doi.org/10.1063/5.0044906

[xlvii] T.J. Awe, B.S. Bauer, S. Fuelling, and R.E. Siemon. *Threshold for Thermal Ionization of an Aluminum Surface by Pulsed Megagauss Magnetic Field*. Phys. Rev. Lett. **104**, 035001 (2010).
DOI: https://doi.org/10.1103/PhysRevLett.104.035001

[xlviii] T.J. Awe, B.S. Bauer, S. Fuelling, I.R. Lindemuth, R.E. Siemon. *Experimental investigation of thermal plasma formation from thick aluminum surfaces by pulsed multi-megagauss magnetic field.* Phys. Plasmas **17**, 102507 (2010).
DOI: https://doi.org/10.1063/1.3491335

[xlix] T.J. Awe, B.S. Bauer, S. Fuelling, and R.E. Siemon. *Mitigation of nonthermal plasma production to measure the pulsed magnetic field threshold for the thermal formation of plasma from thick aluminum surfaces*. Phys. Plasmas **18**, 056304 (2011).
DOI: https://doi.org/10.1063/1.3567485

[l] T. J. Awe, E. P. Yu, K. C. Yates, W. G. Yelton, B. S. Bauer, T. M. Hutchinson, S. Fuelling, and B. B. Mckenzie. *On the Evolution from Micrometer-Scale Inhomogeneity to Global Overheated Structure During the Intense Joule Heating of a z-Pinch Rod*. IEEE Trans. Plasma Sci., **45**, 584 (2017).
DOI: 10.1109/TPS.2017.2655450

[li] T. M. Hutchinson, T. J. Awe, B. S. Bauer, K. C. Yates, E. P. Yu, W. G. Yelton, and S. Fuelling. *Experimental observation of the stratified electrothermal instability on aluminum with thickness greater than a skin depth*. Phys. Rev. E **97**, 053208 (2018).
DOI: https://doi.org/10.1103/PhysRevE.97.053208

[lii] T. M. Hutchinson, T. J. Awe, B. S. Bauer, B. T. Hutsel, D. A. Yager-Elorriaga, K. C. Yates, A. W. Klemmer, M. W. Hatch, S. E. Kreher, E. P. Yu, and M. Gilmore, On the relative importance of the different initial conditions that seed the electrothermal instability, J. Appl. Phys., 130, 153302 (2021).
DOI: https://doi.org/10.1063/5.0063160

[liii] T. M. Hutchinson, T. J. Awe, B. S. Bauer, D. H. Dolan, J. R. Pillars, B. T. Hutsel, E. P. Yu, A. W. Klemmer, and S. E. Kreher. *Photonic Doppler velocimetry of Ohmically exploded aluminum surfaces*. Phys. Plasmas **27**, 052705 (2020).

DOI: https://doi.org/10.1063/1.5140477

[liv] K. C. Yates, B. S. Bauer, S. Fuelling, T. J. Awe, T. M. Hutchinson, V. V. Ivanov, J. Mei, R. S. Bauer, Significant change in threshold for plasma formation and evolution with small variation in copper alloys driven by a mega-ampere current pulse, *Phys. Plasmas*, 26, 042708 (2019).
DOI: https://doi.org/10.1063/1.5066559

[lv] K. C. Yates, T. J. Awe, B. S. Bauer, T. M. Hutchinson, E. P. Yu, S. Fuelling, D. C. Lamppa, M. R. Weis, Initial surface conditions affecting the formation of plasma on metal conductors driven by a mega-ampere current pulse, *Phys. Plasmas*, 27, 082707 (2020).
DOI: https://doi.org/10.1063/5.0003649

[lvi] M.W. Hatch, "Non-uniform Joule heating and plasma formation driven by machined 2D and 3D surface perturbations on dielectric coated and bare aluminum rods," invited talk at 66th Annual Meeting of American Physical Society Division of Plasma Physics [Bull. Am. Phys. Soc., NI03.00003 (2024)].

[lvii] T. J. Awe, E. P. Yu, M. W. Hatch, T. M. Hutchinson, K. Tomlinson, W. D. Tatum, K. C. Yates, B. T. Hutsel, B. S. Bauer, Seeding the explosion of a high-current-density conductor in a controlled manner through the addition of micron-scale surface defects, *Phys. Plasmas*, 28, 072104 (2021).
DOI: https://doi.org/10.1063/5.0053898

[lviii] E. P. Yu, T. J. Awe, K. R. Cochrane, K. C. Yates, T. M. Hutchinson, K. J. Peterson, B. S. Bauer, Use of hydrodynamic theory to estimate electrical current redistribution in metals, *Phys. Plasmas*, 27, 052703 (2020).
DOI: https://doi.org/10.1063/1.5143271

[lix] E. P. Yu, T. J. Awe, K. R. Cochrane, K.J. Peterson, K. C. Yates, T. M. Hutchinson, M.W. Hatch, B. S. Bauer, K. Tomlinson, and D.B. Sinars, Seeding the electrothermal instability through a three-dimensional, nonlinear perturbation Phys. Rev. Lett., 130, 255101 (2023).
DOI: https://doi.org/10.1103/PhysRevLett.130.255101

[lx] E. P. Yu, T. J. Awe, K. R. Cochrane, K.J. Peterson, K. C. Yates, T. M. Hutchinson, M.W. Hatch, B. S. Bauer, K. Tomlinson, and D.B. Sinars, Three-dimensional feedback processes in current-driven metal Phys. Rev. E, 107, 065209 (2023).
DOI: https://doi.org/10.1103/PhysRevE.107.065209

[lxi] J. J. MacFarlane, I. E. Golovkin, P. Wang, P. R. Woodruff, and N. A. Pereyra, SPECT3D – A multi-dimensional collisional-radiative code for generating diagnostic signatures based on hydrodynamics and PIC simulation output, High Energy Density Phys. 3, 181 (2007).
DOI: https://doi.org/10.1016/j.hedp.2007.02.016

[lxii] D. J. Ampleford, D. A. Yager-Elorriaga, C. A. Jennings, E. C. Harding, M. R. Gomez, A. J. Harvey-Thompson, T. J. Awe, G. A. Chandler, G. S. Dunham, M. Geissel, K. D. Hahn, S. B. Hansen, P. F. Knapp, D. C. Lamppa, W. E. Lewis, L. Lucero, M. Mangan, R. Paguio, L. Perea, G. A. Robertson, C. L. Ruiz, D. E. Ruiz, P. F. Schmit, S. A. Slutz, G. E. Smith, I. C. Smith, C. S. Speas, T. J. Webb, M. R. Weis, K. Whittemore, E. P. Yu, R. D. McBride, K. J. Peterson, B. M. Jones, G. A. Rochau, D. B. Sinars, Controlling morphology and

---

improving reproducibility of magnetized liner inertial fusion experiments, *Phys. Plasmas*, 31, 022703 (2024).
DOI: https://doi.org/10.1063/5.0169981

[lxiii] Welch, B. L. (1938). THE SIGNIFICANCE OF THE DIFFERENCE BETWEEN TWO MEANS WHEN THE POPULATION VARIANCES ARE UNEQUAL, *Biometrika*, 29(3-4), 350-362 (1938).
DOI: https://doi.org/10.1093/biomet/29.3-4.350

[lxiv] https://www.ansys.com

DISTRIBUTION

Email—Internal

Name	Org.	Sandia Email Address
Greg Frye	1330	gcfrye@sandia.gov
Jens Schwarz	1659	jschwar@sandia.gov
Eric Harding	1681	ehardi@sandia.gov
David Ampleford	1683	damplef@sandia.gov
Technical Library	1911	sanddocs@sandia.gov

This page left blank

Sandia
National
Laboratories

Sandia National Laboratories is a multimission laboratory managed and operated by National Technology & Engineering Solutions of Sandia LLC, a wholly owned subsidiary of Honeywell International Inc. for the U.S. Department of Energy’s National Nuclear Security Administration under contract DE-NA0003525.